nanoSQUIDs for the detection of small spin systems in strong magnetic fields

Dissertation

der Mathematisch-Naturwissenschaftlichen Fakultät
der Eberhard Karls Universität Tübingen
zur Erlangung des Grades eines
Doktors der Naturwissenschaften
(Dr. rer. nat.)

vorgelegt von
Tobias Schwarz
aus Reutlingen

Tübingen
2014

nanoSQUIDs for the detection of small spin systems in strong magnetic fields

Dissertation

der Mathematisch-Naturwissenschaftlichen Fakultät
der Eberhard Karls Universität Tübingen
zur Erlangung des Grades eines
Doktors der Naturwissenschaften
(Dr. rer. nat.)

vorgelegt von
Tobias Schwarz
aus Reutlingen

Tübingen
2014

Tag der mündlichen Prüfung:	09. Januar 2015
Dekan:	Prof. Dr. W. Rosenstiel
1. Berichterstatter:	Prof. Dr. D. Kölle
2. Berichterstatter:	Prof. Dr. R. Kleiner

Abstract

This thesis deals with the development of ultra-sensitive nanoscaled superconducting quantum interference devices (nanoSQUIDs) for the detection of small spin systems. SQUIDs based on $YBa_2Cu_3O_7$ (YBCO) grain boundary Josephson junctions (GBJs) and Nb SQUIDs with HfTi junctions were investigated. As SQUIDs are the most sensitive detectors for magnetic flux, they are suitable candidates for the characterization of small magnetic spin systems like magnetic nanoparticles, which are in the focus of a large variety of research areas. However, the SQUIDs have to be adapted to fulfill this purpose. With the ultimate goal to detect single spin flips, the spin sensitivity has to be improved significantly compared to conventional SQUIDs. Furthermore, the detection of magnetization reversal of magnetic nanoparticles demands for operation of the SQUIDs in strong magnetic fields from several milliteslas up to the tesla range, which is impossible for conventional SQUIDs. To fulfill these requirements the SQUIDs have to be miniaturized. By reducing the loop size a lower geometric inductance can be achieved, resulting in an improvement of the flux noise level. At the same time miniaturization of the SQUID loop and the junctions together with an appropriate SQUID layout help to make the SQUID less sensitive to homogeneous external magnetic fields. Smaller line widths increase the coupling of the stray field of a magnetic particle placed close to the SQUID. The miniaturization of smallest line widths of several tens of nanometers demands for special fabrication technologies that have to be developed and optimized.

In the first stage of this thesis a process for the fabrication of YBCO GBJ nanoSQUIDs using focused ion beam (FIB) milling has been developed. For the first generation of nanoSQUIDs, YBCO films with thickness $d = 50\,\mathrm{nm}$ were grown epitaxially on $SrTiO_3$ (STO) bicrystals with a misorientation angle of 24° using pulsed laser deposition. Subsequently, a 60 nm thick gold layer was evaporated to provide non-hysteretic current-voltage characteristics (IVCs). After prepatterning 7 μm wide bridges across the grain boundary, using optical lithography and argon ion beam milling the SQUIDs were nanostructured using FIB milling. By choosing

appropriate milling parameters smallest line widths of 50 nm could be fabricated without loss of superconductivity. A constriction patterned next to the SQUID loop allowed flux biasing of the device by applying an additional modulation current. This enabled operation of the SQUID in a flux locked loop (FLL) mode at the optimum working point. To achieve optimum coupling of the stray field generated by a magnetic particle into the SQUID loop, the particle has to be placed on top of the constriction. For one of the first generation of nanoSQUIDs a white flux noise level $S_\Phi^{1/2} = 1.3\,\mu\Phi_0/\mathrm{Hz}^{1/2}$ could be determined at an operation temperature $T = 4.2\,\mathrm{K}$ (Φ_0 is the magnetic flux quantum). With a calculated coupling factor $\phi_\mu = 21\,\Phi_0/\mu_B$ this corresponds to a spin sensitivity of $S_\mu^{1/2} = S_\Phi/\phi_\mu = 62\,\mu_B/\mathrm{Hz}^{1/2}$ (μ_B is the Bohr magneton). Even in magnetic fields up to $B = 3\,\mathrm{T}$ the SQUID could be operated with only a slight suppression of the critical current. At $B = 1\,\mathrm{T}$ only a slight degradation of the spin sensitivity was observable.

In the second stage of this thesis a numerical study was performed in order to optimize the spin sensitivity of the YBCO nanoSQUIDs. The influence of all relevant geometric parameters on the spin sensitivity was investigated. It has been shown that with optimized SQUID parameters, spin sensitivities of only a few $\mu_B/\mathrm{Hz}^{1/2}$ should be feasible.

This theoretical prediction was subsequently confirmed by experimental results. For YBCO nanoSQUIDs with optimum film thickness $d = 120\,\mathrm{nm}$, flux noise levels down to $S_\Phi^{1/2} = 50\,\mathrm{n}\Phi_0/\mathrm{Hz}^{1/2}$ in magnetically shielded environment were observed. The corresponding spin sensitivity is $S_\mu^{1/2} = 3.7\,\mu_B/\mathrm{Hz}^{1/2}$. However, this value could only be determined at the cutoff frequency of the readout electronics $f_{3dB} = 7\,\mathrm{MHz}$. For lower frequencies the spectrum was dominated by frequency-dependent excess noise scaling approximately as $S_\Phi \propto 1/f$. Even the application of a bias reversal readout scheme could only partially reduce the $1/f$ noise.

To check the suitability of the YBCO nanoSQUIDs for the investigation of small spin systems, the magnetization reversal of an iron nanowire encapsulated in a multiwall carbon nanotube (MW-CNT) was detected. Therefore, the nanowire was placed close to the SQUID. By sweeping a magnetic field between $B = \pm 150\,\mathrm{mT}$ the magnetization of the single domain nanowire could be switched and the changing stray field could be detected directly with the SQUID with unprecedented signal-to-noise ratio.

In the second part of this thesis, the spin sensitivity of Nb nanoSQUIDs was investigated in magnetic fields up to $B = 0.5\,\mathrm{T}$ at $T = 4.2\,\mathrm{K}$. The SQUIDs were fabricated at the Physikalisch Technische Bundesanstalt (PTB) in Braunschweig. As for the

YBCO SQUIDs, a modulation line, that allows for operation of the SQUIDs at the optimum working point without the need of an external coil, was implemented. At $B = 0$ a spin sensitivity $S_\mu^{1/2} = 23\,\mu_B/\mathrm{Hz}^{1/2}$ was determined. Up to fields of $B = 50\,\mathrm{mT}$ only a negligible increase of the spin sensitivity was observable and even at $B = 0.5\,\mathrm{T}$ a spin sensitivity of $S_\mu^{1/2} = 79\,\mu_B/\mathrm{Hz}^{1/2}$ could be achieved.

Kurzfassung

Thema dieser Dissertation ist die Entwicklung extrem empfindlicher, nanoskaliger supraleitender Quanteninterferometer (nanoSQUIDs) für die Detektion kleinster magnetischer Spinsysteme. Es wurden SQUIDs basierend auf $YBa_2Cu_3O_7$ (YBCO) Korngrenzenkontakten (GBJs) und Nb SQUIDs mit HfTi Kontakten untersucht. SQUIDs, als die derzeit empfindlichsten Detektoren für magnetischen Fluss, sind vielversprechend für die Charakterisierung kleinster magnetischer Spinsysteme, wie zum Beispiel magnetische Nanopartikel, an deren potentiellen Anwendungsmöglichkeiten in verschiedensten Bereichen geforscht wird. Allerdings müssen die SQUIDs für diesen Zweck entsprechend angepasst werden. Mit dem Ziel, das Umklappen einzelner Spins detektieren zu können, muss die Spinsensitivität der SQUIDs gegenüber der konventioneller SQUIDs deutlich verbessert werden. Zudem erfordert die Messung von Magnetisierungskurven magnetischer Nanopartikel den Betrieb der SQUIDs in starken Magnetfeldern vom Millitesla- bis in den Teslabereich, was mit konventionellen SQUIDs nicht möglich ist. Umgesetzt werden können diese Anforderung durch eine Miniaturisierung der SQUIDs. Die Reduktion des SQUID-Rings führt dabei zu einer kleineren geometrischen Induktivität und damit zu einer Verbesserung des Flussrauschens und verringert zugleich, zusammen mit der Miniaturisierung der Kontakte und einer Anpassung des Layouts, die Empfindlichkeit des SQUIDs auf homogene äußere Magnetfelder. Schmalere Stegbreiten erhöhen die Kopplung des Streufeldes eines nahe des SQUIDs platzierten magnetischen Partikels. Die Miniaturisierung von Strukturen mit kleinsten Breiten von nur wenigen zehn Nanometern erfordert spezielle Fertigungsprozesse, die entwickelt und optimiert werden müssen.

Im ersten Teil dieser Arbeit wurde ein Verfahren entwickelt, um YBCO nanoSQUIDs mit Korngrenzenkontakten mittels fokussiertem Ionenstrahlätzen (FIB-Ätzen) zu fertigen. Hierfür wurden für die erste Generation von nanoSQUIDs epitaktische YBCO Filme der Dicke $d = 50\,\mathrm{nm}$ auf $SrTiO_3$ (STO) Bikristallen mit einem Korngrenzenwinkel von 24° mittels gepulster Laserdeposition aufgewachsen. An-

schließend wurde, um nicht-hysteretische Kennlininen zu erhalten, ein 60 nm dicker Goldfilm aufgedampft. Nach der Vorstrukturierung von 7 μm breiten Brücken über die Korngrenze mittels optischer Lithographie und Argon Ionenstrahlätzen, erfolgte die Nanostrukturierung der SQUIDs mittels FIB-Ätzen. Eine geeignete Wahl der FIB Parameter ermöglichte die Herstellung von kleinsten Stegbreiten bis zu 50 nm, ohne den Verlust der Supraleitung. Über eine Einschnürung, die neben das SQUID strukturiert wurde, konnte durch einen Modulationsstrom der in das SQUID einkoppelnde Fluss gesteuert werden. Dadurch konnte das SQUID mit Hilfe einer Flussregelschleife am optimalen Arbeitspunkt betrieben werden. Um die optimale Kopplung eines magnetischen Partikels an das SQUID zu erhalten, muss dieses auf der Einschnürung platziert werden. Ein weißes Flussrauschen $S_\Phi^{1/2} = 1.3\,\mu\Phi_0/\mathrm{Hz}^{1/2}$, mit dem magnetischen Flussquant Φ_0, konnte bei einer Temperatur $T = 4.2\,\mathrm{K}$ für eines der ersten SQUIDs ermittelt werden. Dies entspricht, mit einem berechneten Kopplungsfaktor $\phi_\mu = 21\,\Phi_0/\mu_B$ (μ_B ist das Bohrsche Magneton), einer Spinsensitivität von $S_\mu^{1/2} = S_\Phi/\phi_\mu = 62\,\mu_B/\mathrm{Hz}^{1/2}$. Selbst in Feldern von bis zu $B = 3\,\mathrm{T}$ konnte das SQUID mit nur leichter Unterdrückung des maximalen kritischen Stroms betrieben werden. Bei $B = 1\,\mathrm{T}$ zeigte sich nur eine leichte Reduktion der Spinsensitivität $S_\mu^{1/2} = 110\,\mu_B/\mathrm{Hz}^{1/2}$.

Um die Spinsensitivität der SQUIDs zu optimieren, wurde im nächsten Schritt eine numerische Analyse durchgeführt, die den Einfluss aller relevanten geometrischen Parameter auf das Flussrauschen und den Kopplungsfaktor der SQUIDs ermittelte. Nach dieser Untersuchung sollten, bei geeigneter Wahl der SQUID-Parameter, optimierte Spinsensitivitäten von nur wenigen $\mu_B/\mathrm{Hz}^{1/2}$ realisierbar sein.

Die anschließende experimentelle Umsetzung der Simulationsergebnisse bestätigte diese Abschätzung. So konnte für YBCO nanoSQUIDs aus Filmen mit der optimierten Dicke $d = 120\,\mathrm{nm}$ eine obere Grenze für das weiße Flussrauschen von $S_\Phi^{1/2} = 50\,\mathrm{n}\Phi_0/\mathrm{Hz}^{1/2}$ in geschirmter Umgebung ermittelt werden. Dies entspricht einer Spinsensitivität $S_\mu^{1/2} = 3.7\,\mu_B/\mathrm{Hz}^{1/2}$. Einschränkend bleibt jedoch anzumerken, dass dieser Wert bei der Abschneidefrequenz der Elektronik $f_{3dB} = 7\,\mathrm{MHz}$ bestimmt wurde. Unterhalb dieser Frequenz wurde das Spektrum von frequenzabhängigem Rauschen dominiert. Auch durch die Anwendung von geeigneten Auslesemethoden *(bias reversal)* konnte das $1/f$-Rauschen nur teilweise unterdrückt werden.

Um die Eignung der SQUIDs für die Untersuchung kleiner Spinsysteme zu zeigen, wurde die Magnetisierungskurve eines Eisennanodrahtes, der von einer Kohlenstoffnanoröhre umschlossen war, detektiert. Dazu wurde der Draht nahe des SQUIDs platziert. Durch Anlegen eines externen Magnetfelds zwischen $B = \pm 150\,\mathrm{mT}$ konn-

te die Magnetisierungsrichtung des eindomänigen Nanodrahtes umgeklappt und das sich ändernde Streufeld mit dem SQUID detektiert werden. Dies gelang mit einem bis dahin unerreichten Signal-zu-Rausch-Verhältnis.

Im zweiten Teil der Arbeit wurde die Spinsensitivität von Nb nanoSQUIDs in Magnetfeldern bis zu $B = 0.5\,\mathrm{T}$ bei $T = 4.2\,\mathrm{K}$ untersucht. Die SQUIDs wurden von der Physikalisch Technischen Bundesanstalt (PTB) in Braunschweig gefertigt. Sie verfügen, wie die YBCO SQUIDs, über eine Modulationsleitung, mit Hilfe derer die SQUIDs ohne externe Spule am optimalen Arbeitspunkt betrieben werden können. Bei $B = 0$ konnte eine Spinsensitivität von $S_\mu^{1/2} = 23\,\mu_B/\mathrm{Hz}^{1/2}$ ermittelt werden. Bis zu $B = 50\,\mathrm{mT}$ stieg diese nur unwesentlich an und selbst bei Feldern von $B = 0.5\,\mathrm{T}$ konnte noch eine Spinsensitivität von $S_\mu^{1/2} = 79\,\mu_B/\mathrm{Hz}^{1/2}$ erreicht werden.

List of publications

This is a cumulative thesis which is based on the publications listed below. The publications are attached at the very end of the thesis

Appended Publications

.

Publication 1 **T. Schwarz**, J. Nagel, R. Wölbing, M. Kemmler, R. Kleiner, and D. Koelle

Low-Noise Nano Superconducting Quantum Interference Device Operating in Tesla Magnetic Fields

ACS Nano **7**, 844 (2013)

Publication 2 R. Wölbing, **T. Schwarz**, B. Müller, J. Nagel, M. Kemmler, R. Kleiner, and D. Koelle

Optimizing the spin sensitivity of grain boundary junction nanoSQUIDs - towards detection of small spin systems with single-spin resolution

Supercond. Sci. Technol. **27**, 125007 (12pp) (2014)

Publication 3 **T. Schwarz**, R. Wölbing, C. F. Reiche, B. Müller, M. J. Martínez-Pérez, T. Mühl, B. Büchner, R. Kleiner, and D. Koelle

Low-Noise $YBa_2Cu_3O_7$ Nano Superconducting Quantum Interference Devices for Magnetization Reversal Measurements on Magnetic Nanoparticles

submitted to Phys. Rev. Appl. (2014)

Publication 4 R. Wölbing, J. Nagel, **T. Schwarz**, O. Kieler, T. Weimann, J. Kohlmann, A. B. Zorin, M. Kemmler, R. Kleiner, and D. Koelle

Nb nano superconducting quantum interference devices with high spin sensitivity for operation in magnetic fields up to 0.5 T

Appl. Phys. Lett. **102**, 192601 (2013)

Publications not included in this thesis

Publication 5 J. Li, J. Yuan, M. Ji, G. Zhang, J. Y. Ge, H. L. Feng, Y. H. Yuan, T. Hatano, W. Hu, K. Jin, **T. Schwarz**, R. Kleiner, D. Koelle, K. Yamaura, H. B. Whang, P. H. Wu, E. Takayama-Muromachi, J. Vanacken, V. V. Moshchalkov

Impurities effects on the normal-state transport properties of $Ba_{0.5}K_{0.5}Fe_2As_2$ *superconductors*

Phys. Rev. B **90**, 024512 (2014)

Publication 6 J. Li, M. Ji, **T. Schwarz**, X. Ke, G. Van Tendeloo, J. Yuan, Y. Huang, G. Zhang, H. L. Feng, Y. H. Yuan, T. Hatano, R. Kleiner, D. Koelle, L. F. Chibotaru, K. Yamaura, H. B. Wang, P. H. Wu, E. Takayama-Muromachi, J. Vanacken, V. V. Moshchalkov

Local destruction of superconductivity by nonmagnetic impurities in mesoscopic iron-based superconductors

submitted to Nat. Commun. (2014)

Contents

Chapter 1

Introduction

Magnetic nanoparticles (MNPs) like nanomagnets, magnetic molecules or magnetic nanowires are in the focus of many current research areas. Their magnetic characteristics are completely different from those of their bulk counterparts, which makes them interesting not only for fundamental research on magnetism but also for a wide range of applications in biomedicine, data storage, spintronic devices, etc. [1–7]. Below a certain particle size it will be energetically favorable for ferromagnetic or ferrimagnetic materials to be in a single domain state. In the single domain state MNPs can show high magnetic anisotropy which results in very high coercive fields. These particles are in a stable magnetic configuration which makes them suitable for applications in data storage devices with huge packaging density [8].

The energy barrier that needs to be overcome to switch the magnetization of a single domain particle (SDP) is $\Delta E = KV$, where K is the anisotropy constant and V is the volume of the particle. If the volume of a SDP is small enough, the magnetization will flip induced by thermal fluctuations with the Néel relaxation time $\tau_N = \tau_0 \exp(KV/k_BT)$ (were τ_0 is a characteristic time, k_B is the Boltzmann constant and T is the temperature) and change into the superparamagnetic state. For biomedical applications, particles that show a superparamagnetic behaviour at room temperature are of great interest [9]. MNPs can be used for drug delivery [10], as contrast agents [11] or for hyperthermia treatments in cancer therapy [12].

As the magnetic moment of a MNP is very small, the investigation of their magnetic characteristics is difficult. With conventional magnetic field sensors only the detection of an ensemble of MNPs is possible. This complicates the analysis of the accuired data, since interactions between the particles have to be considered. Further, no information on anisotropy of the particles can be obtained if they are

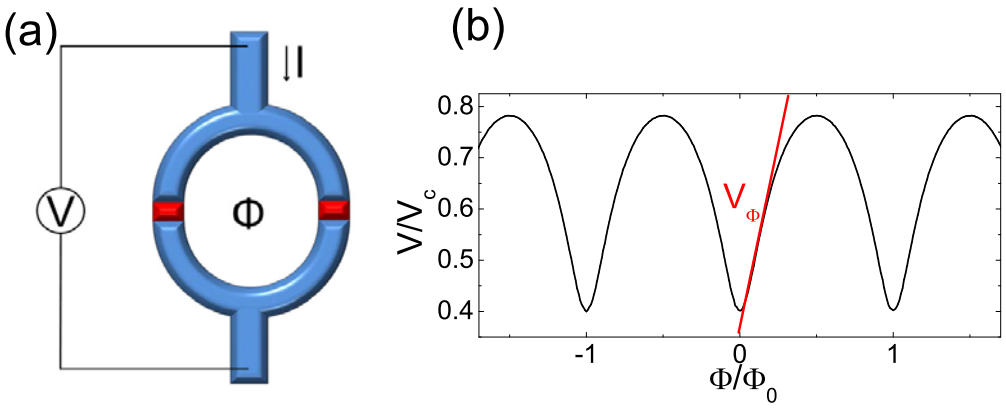

Figure 1.1: (a) Scheme of a dc SQUID, red areas indicate the Josephson junctions. (b) $V(\Phi)$-characteristics plotted for bias current $I = 2.3I_0$ where I_0 is the critical current of a single junction. Red line indicates the transfer function at the optimum working point. V_c is the characteristic voltage of the Josephson junctions.

oriented randomly. For this reason the development of new sensors capable to detect the field generated by a single MNP is of great importance. To detect the magnetization reversal of a MNP that carries only a few Bohr magnetons, the detector needs to be highly sensitive and the particle has to be placed in very close vicinity of the detector. This implies that it should be feasible to operate the detector in very strong magnetic fields that are necessary to switch the magnetization of a MNP. Wernsdorfer *et al.* [13] proposed to use micron-sized Superconducting Quantum Interference Devices (SQUIDs) for magnetization reversal measurements of MNPs.

SQUIDs [14] are the most sensitive detectors for magnetic flux. They consist of a superconducting ring intersected by two Josephson junctions [15] (Fig. 1.1(a)) (in the case of a dc SQUID). Magnetic flux Φ coupling into the dc SQUID loop results in a periodic modulation of the voltage drop V across the device (Fig. 1.1(b)). Measurements with highest sensitivity can be performed with the SQUID biased at the point with the steepest slope of the $V(\Phi)$-characteristics. The resolution of the SQUID is limited by the white flux noise level $S_\Phi^{1/2} = S_V^{1/2}/|V_\Phi|$ where S_V is the spectral density of voltage noise, $\Phi_0 \approx 2.07 \cdot 10^{-15}\,\mathrm{T/m^2}$ is the flux quantum and $V_\Phi = (dV/d\Phi)_{max}$ is the transfer function. Conventional devices typically have a white flux noise level of a few $\mu\Phi_0/\mathrm{Hz}^{1/2}$ and are usually operated in the earth's magnetic field ($\approx 50\,\mu\mathrm{T}$) or in magnetically shielded environment.

To detect the magnetization reversal of a MNP, the particle must be placed close to the SQUID, so that the stray field of the particle couples into the loop (Fig. 1.2). To

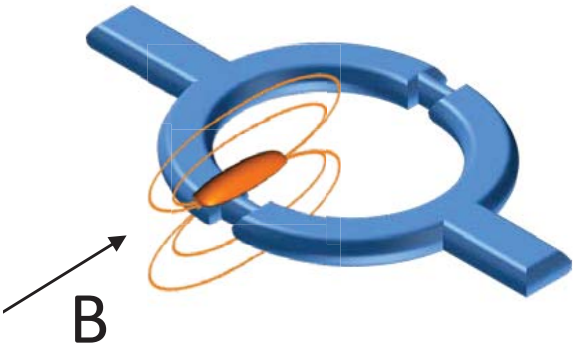

Figure 1.2: MNP placed on top of a constriction in the SQUID loop, where the coupling is strongest. A magnetic field B applied parallel to the loop switches the magnetization of the MNP.

switch the magnetization of the MNP placed on top of the SQUID a magnetic field B has to be applied. This needs to be done in a way that the applied field does not couple into the SQUID loop (i.e. the field should be oriented parallel to the loop) or into the Josephson junctions (i.e. field oriented perpendicular to the junction barrier). Miniaturization of the SQUID loop and the junctions helps to lower the influence of slight misalignments of the SQUID with respect to the applied field. Also the line widths w and film thickness d of the SQUID should be of the order of the London penetration depth λ_L or below, to avoid the penetration of Abrikosov vortices.

The amount of flux Φ that couples into the SQUID for a particle carrying a magnetic moment μ is given by the coupling factor $\phi_\mu = \Phi/\mu$. It strongly depends on the position of the particle, the orientation of $\vec{\mu}$ and the SQUID layout. The optimum coupling factor can be achieved for a particle placed on top of the SQUID at the position where the loop has its smallest line width w.

Together with the flux noise level the coupling factor determines the spin sensitivity $S_\mu^{1/2} = S_\Phi^{1/2}/\phi_\mu$ of the SQUID, i.e. the smallest number of Bohr magnetons that can be detected. Both parameters, flux noise level and coupling factor, have to be optimized to achieve high spin sensitivities. Considering the theoretical expression [16] for the spectral density of flux noise $S_\Phi = f(\beta_L)LT\Phi_0/I_0R$, with screening parameter $\beta_L = 2I_0L/\Phi_0$, loop inductance L, temperature T, critical current I_0 and normal resistance R of the Josephson junctions and $f(\beta_L) \approx 4(1+\beta_L)$ for $\beta_c > 0.4$ [14], the spin sensitivity can be optimized by choosing SQUID parameters that reduce the inductance and increase the characteristic voltage $V_c = I_0R$. Reduction of the geometric inductance can be achieved by shrinking the loop size. High V_c demands for high quality junctions that provide high critical current densities, so that even for miniaturized junctions, that are advantageous for applications in strong

magnetic fields, sufficiently large critical currents can be achieved.

In summary, miniaturization of the SQUID helps to achieve high spin sensitivity and to make the SQUIDs suitable for high field applications. However, miniaturization also brings a counterbalancing effect, that is the rise of the kinetic inductance $L_{kin} = \mu_0 \lambda_L^2 l/wd$ and hence the flux noise S_Φ with shrinking film thickness d and line width w.

To meet these challenges a great variety of nanoSQUIDs [17–37] made of different materials have been developed within the last years. The most common approach are SQUIDs with constriction type Josephson junctions (cJJs) [19, 20, 22, 24, 31, 34, 35]. For magnetization measurements a MNP can be placed close to the constriction where the coupling factor is highest. However in this case, an optimization of the coupling factor cannot be performed without affecting the junction parameters, which makes optimization of the nanoSQUIDs difficult. Film thicknesses well below λ_L allow for the operation in strong magnetic fields up to the tesla range exceeding the upper critical field B_{c2} of the superconducting material. However, the use of very thin films increases the kinetic inductance of the SQUIDs and makes them less sensitive. Further, cJJs usually have hysteretic current-voltage characteristics (IVCs), which complicates operation in a flux locked loop (FLL) mode. Finally, the temperature range, where the SQUIDs can be operated with optimum performance, is very narrow and close to the transition temperature T_c, which is unfavorable for many applications.

One of the currently most successful nanoSQUID designs is the SQUID-on-tip (SOT) [34, 36, 37]. This device is fabricated by shadow evaporation of Pb, Al or Nb on a quartz tip with smallest apex diameters down to $\approx 50\,\mathrm{nm}$. With a spin sensitivity of $0.38\,\mu_B/\mathrm{Hz}^{1/2}$ [36], SOTs are theoretically capable to perform measurements with single spin resolution. The SOT is a powerful tool for scanning SQUID microscopy and can be used for the imaging of magnetic domains, current distributions or Abrikosov vortices. In contrast to conventional SQUIDs for scanning SQUID microscopy it is also possible to use a SOT to detect in-plane and out-of-plane components of the magnetic field without the need of a reorientation of the sample [37]. However, up to now there is no possibility to keep the optimum flux bias point of the SOT at a variable magnetic field. Hence, measurements of magnetization reversal on magnetic nanoparticles are difficult to perform with a SOT.

The nanoSQUID project, which is presented in this work started with the aim of developing nanoSQUIDs that circumvent the disadvantages of the nanoSQUID designs mentioned above. Operation of the nanoSQUIDs in a FLL mode with high

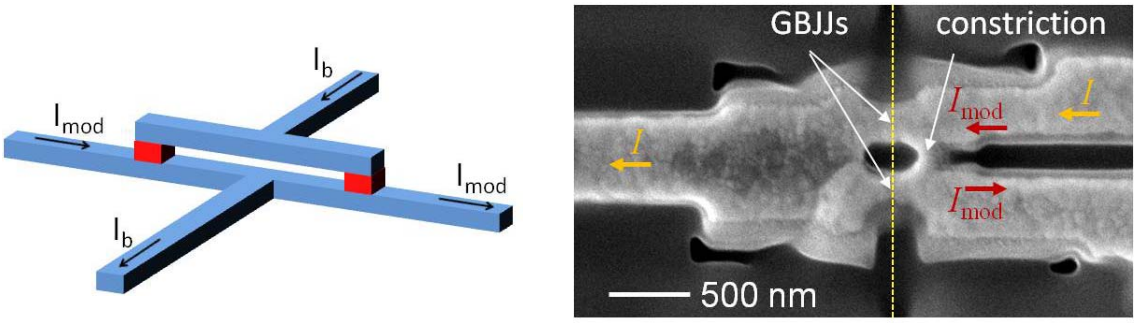

Figure 1.3: Left: Scheme of Nb nanoSQUID. Red areas indicate the HfTi Josephson junctions. The SQUID loop is oriented perpendicular to the substrate. Paths for the bias current I_b and the modulation current I_{mod} are indicated by arrows. Right: SEM image of a YBCO nanoSQUID. The grain boundary is indicated by the dashed yellow line. Current paths are indicated by arrows. Figure modified from appended publication 3. © Institute of Physics and IOP Publishing.

spin sensitivity over a wide temperature range should be possible. The design of the nanoSQUIDs should allow for an optimization of the coupling factor without affecting the junction properties. And finally, the nanoSQUIDs should be suitable for stable operation in high magnetic fields.

Two types of nanoSQUIDs were developed (see Fig. 1.3). The first type [38–41] is based on Nb/HfTi/Nb superconductor/normal metal/superconductor (SNS) junctions and is fabricated at the Physikalisch Technische Bundesanstalt (PTB) in Braunschweig. Electron beam lithography is used to nanopattern the SQUIDs and smallest loop sizes of $\approx 600 \times 200\,\mathrm{nm}^2$ could be realized. Compared to Nb/AlO_x/Nb junctions that are commonly used in conventional SQUIDs, the use of HfTi junctions brings two advantages. First, HfTi junctions provide high critical current densities $j_c \approx 10^5\,\mathrm{A/cm}^2$ at 4.2 K. Therefore, high critical currents can be achieved even for miniaturized junctions. Second, the junctions are intrinsically shunted. This provides non-hysteretic IVCs without an external shunt resistance that would make miniaturization more difficult. To allow for FLL operation, a modulation line is implemented in the SQUID design. Via a modulation current applied across the bottom electrode, the nanoSQUIDs can be flux biased at the optimum working point. Stable operation of these devices has been demonstrated in magnetic fields up to 100 mT with spin sensitivities $S_\mu^{1/2} \approx 40\mu_B/\mathrm{Hz}^{1/2}$. The focus in this thesis is on the second type of SQUID [42–44], which is based on $YBa_2Cu_3O_7$ (YBCO) grain boundary junctions. Nanopatterning was done by focused ion beam (FIB) milling. As for the HfTi junctions, high critical current densities can be achieved. A gold layer evaporated on the YBCO film serves as a shunt resistance to provide non-

hysteretic IVCs. By applying a modulation current across an additional constriction next to the SQUID loop, the SQUID can be flux biased at the optimum working point. YBCO offers the advantage to use the SQUIDs in a wide temperature range, due to the larger transition temperature of $T_c = 92\,\mathrm{K}$ compared to $T_c = 9.25\,\mathrm{K}$ for Nb. More importantly, the huge upper critical field $B_{c2} > 30\,\mathrm{T}$ allows for magnetization reversal measurements on MNPs with strong coercive fields in the tesla range. In **Publication 1** noise measurements and calculated spin sensitivities at $B = 0$ and $B = 1\,\mathrm{T}$ of a YBCO nanoSQUID are presented. A numerical optimization study of the spin sensitivity for this SQUID layout can be found in **Publication 2**. The experimental verification of the predictions of **Publication 2** are described in **Publication 3**. Also included in this publication is a magnetization reversal measurement of an iron filled carbon nanotube [45]. **Publication 4** summarizes the results of noise measurements in magnetic fields up to $0.5\,\mathrm{T}$ for a Nb nanoSQUID.

Chapter 2

Summary of Publications

2.1 Summary of Publication 1:

Low-Noise Nano Superconducting Quantum Interference Device Operating in Tesla Magnetic Fields

Usually, SQUIDs are operated in the earth‘s magnetic field or in magnetically shielded environment. To allow for the detection of magnetization reversal of magnetic nanoparticles, SQUIDs have to be operated in strong magnetic fields. This demands for miniaturization of the loop, the junctions and the line width of the SQUID. Also, the (upper) critical magnetic field of the superconducting material is important. Due to the huge upper critical field B_{c2}, in the range of tens of teslas, SQUIDs based on YBCO theoretically can easily be operated in fields in the tesla range. To nanopattern YBCO, milling parameters have to be chosen carefully as superconductivity can be lost due to oxygen outdiffusion. The aim of this work was to fabricate YBCO nanoSQUIDs with grain boundary junctions (GBJs) and demonstrate their suitability for applications in high magnetic fields with high spin sensitivity.

The fabrication of the nanoSQUIDs was done in a similar way as described in [42]. A $d = 50\,\mathrm{nm}$ thick YBCO film was grown epitaxially on a STO bicrystal substrate with a misorientation angle of 24°. To provide non-hysteretic IVCs a 60 nm thick gold layer which serves as a shunt resistance was evaporated *in-situ* on top of the YBCO film. After prepatterning of 7 μm wide bridges across the grain boundary by photolithography and Ar ion milling, two $w_J = 130\,\mathrm{nm}$ wide Josephson junctions and an additional constriction next to the SQUID loop with a width $w_c = 90\,\mathrm{nm}$ were

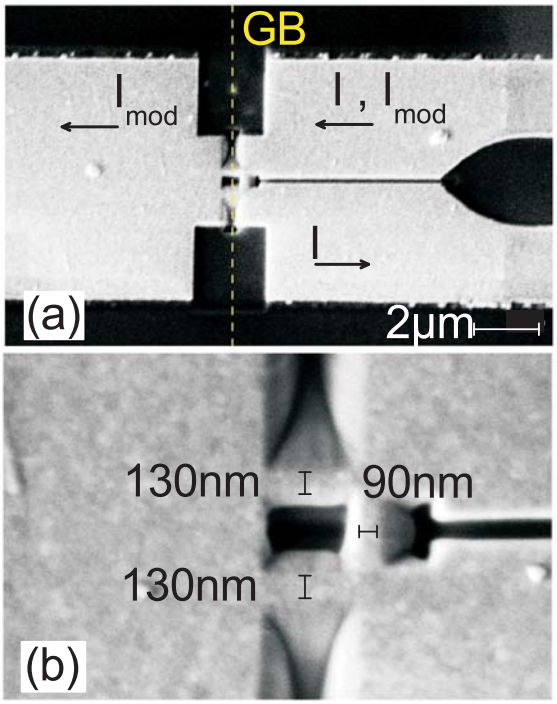

Figure 2.1: SEM images of the YBCO nanoSQUID. (a) Current paths for the modulation current and the bias current are indicated by arrows. The dashed yellow line indicates the position of the grain boundary. (b) Widths of the junctions and the constriction are indicated. Figure from appended Publication 1. © American Chemical Society.

patterned by focused ion beam (FIB) milling (Fig. 2.1). Via the constriction the SQUID can be flux biased by applying a modulation current I_{mod}. For magnetization measurements a MNP would be placed on top of the constriction as it has the smallest line width and therefore is the position with the strongest coupling.

Electronic transport measurements at $T = 4.2\,\mathrm{K}$ were first performed in a magnetically shielded environment. We determined a critical current $I_0 = 18.5\,\mu\mathrm{A}$ and a resistance $R = 7\,\Omega$ of each junction. The maximum transfer function was $V_\Phi = 450\,\mu\mathrm{V}/\Phi_0$. Via numerical simulations of the $I_c(I_{mod})$-characteristics we found the screening parameter $\beta_L = 0.65$ and calculated the inductance $L = 36\,\mathrm{pH}$. To test the high field suitability of the device, the nanoSQUID was installed in a high field setup with a superconduction split-coil magnet which allows to apply fields up to 7 T. Magnetic fields up to $B = 3\,\mathrm{T}$ were applied, with the field aligned parallel to the SQUID loop and perpendicular to the grain boundary (Fig. 2.2). To perform the alignment the SQUID was mounted on an high-precision alignment system consisting of two goniometers with perpendicular tilt axes and a rotator. Even at $B = 3\,\mathrm{T}$ modulation of the SQUID could be observed with only slight degradation of the critical current.

For noise measurements the SQUID was connected parallel to the input circuit of a SQUID amplifier. The voltage drop across the nanoSQUID was readout with the amplifier SQUID in a so called two-stage configuration [46]. Flux noise spectra were

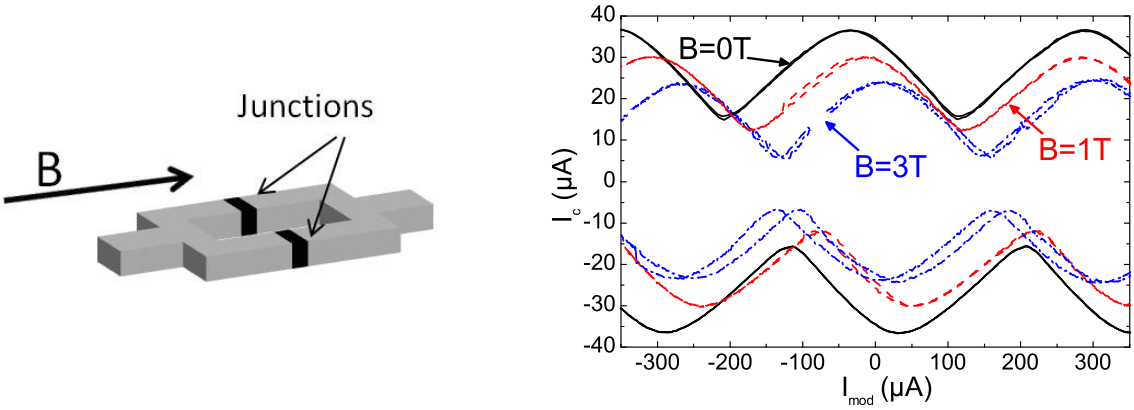

Figure 2.2: Left: Schematic layout of the YCBO nanoSQUID. Black areas indicate the GBJs. The magnetic field B is aligned parallel to the SQUID loop and perpendicular to the grain boundary. Right: Critical current $I_c(I_{mod})$ for $B = 0, 1$ and $3\,\mathrm{T}$ at $T = 4.2\,\mathrm{K}$. Figure modified from Publication 1. © American Physical Society.

measured at $B = 0$ and $B = 1\,\mathrm{T}$ (see Fig. 2.3). Only a slight increase in the white flux noise level from $S_\Phi^{1/2} = 1.3\,\mu\Phi_0/\mathrm{Hz}^{1/2}$ at $B = 0$ to $S_\Phi^{1/2} = 2.3\mu\Phi_0/\mathrm{Hz}^{1/2}$ at $B = 1\,\mathrm{T}$ could be observed.

Calculation of the coupling factor ϕ_μ was done according to [38] using the software package 3D-MLSI [47]. For a point-like particle placed on top of the constriction 10 nm above the YBCO layer we could determine $\phi_\mu = 21\,\mathrm{n}\Phi_0/\mu_B$. This yields a spin sensitivity $S_\mu^{1/2} = 62\,\mu_B/\mathrm{Hz}^{1/2}$ at $B = 0$ and $S_\mu^{1/2} = 121\,\mu_B/\mathrm{Hz}^{1/2}$ at $B = 1\,\mathrm{T}$.

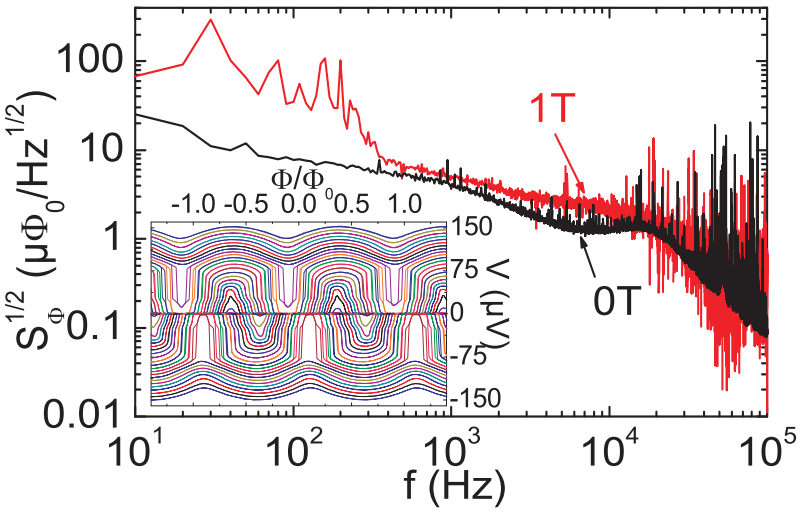

Figure 2.3: Measured flux noise spectra at $B = 0$ (black) and $B = 1\,\mathrm{T}$ (red) at $T = 4.2\,\mathrm{K}$; the observed flux noise levels in the white noise regime were $S_\Phi^{1/2} = 1.3\,\mu_B/\mathrm{Hz}^{1/2}$ and $S_\Phi^{1/2} = 2.3\,\mu_B/\mathrm{Hz}^{1/2}$, respectively [43]. The inset shows $V(\Phi)$ curves at $B = 0$ for bias currents $I = -49.5 \ldots 49.5\,\mu\mathrm{A}$. Figure from appended Publication 1. © American Chemical Society.

In summary, we fabricated YBCO nanoSQUIDs and showed that operation of the SQUIDs in strong magnetic fields up to $B = 3\,\mathrm{T}$ is possible. Even at $B = 1\,\mathrm{T}$ a high spin sensitivity $S_\mu^{1/2} = 121\,\mu_B/\mathrm{Hz}^{1/2}$ could be observed. This was the first publication presenting flux noise spectra of a SQUID measured at magnetic fields $B = 1\,\mathrm{T}$. These results confirm that the SQUID fulfills the requirements necessary to use it as a detector of small spin systems.

Contributions

J. Nagel developed the measurement setup and the sample design and assisted with the measurements and the interpretation of the results. R. Wölbing did the simulations of the coupling factor. M. Kemmler assisted with the experiments. My contribution to this publication was the fabrication of the nanoSQUID. Further, I performed the measurements and analyzed the experimental data.

2.2 Summary of Publication 2:

Optimizing the spin sensitivity of grain boundary junction nanoSQUIDs - towards detection of small spin systems with single-spin resolution

One major drawback of SQUIDs based on constriction type Josephson junctions is that the best coupling factor can be achieved close to the junctions. This means that an optimization of the coupling via changing the geometry of the cJJs, will always have an influence on the junction properties. This complicates the optimization of the spin sensitivity of cJJ based nanoSQUIDs significantly. In contrast, the YBCO nanoSQUID layout presented in this thesis offers the possibility to optimize the coupling factor independently from the junction parameters as the position of best coupling is on top of the constriction which is separated from the GBJs. The device presented in Publication 1 showed a spin sensitivity of $S_\mu^{1/2} = 62\,\mu_B/\mathrm{Hz}^{1/2}$. To achieve a further improvement of S_μ we performed a numerical optimization study for this SQUID layout using the software package 3D-MLSI [47]. This simulation program uses London theory to calculate the current distribution in a stack of two-dimensional sheets that define the geometry of the SQUID (Fig. 2.4).

We could calculate the coupling factor ϕ_μ and the SQUID inductance L as a function of all relevant geometrical parameters of the SQUID layout and the electrical parameters of the GBJs. The calculation of the coupling factor was done using three different methods. All methods yielded the same scaling of the coupling factor $\phi_\mu(d, w_c)$ with film thickness d and constriction width w_c, within the considered parameter range.

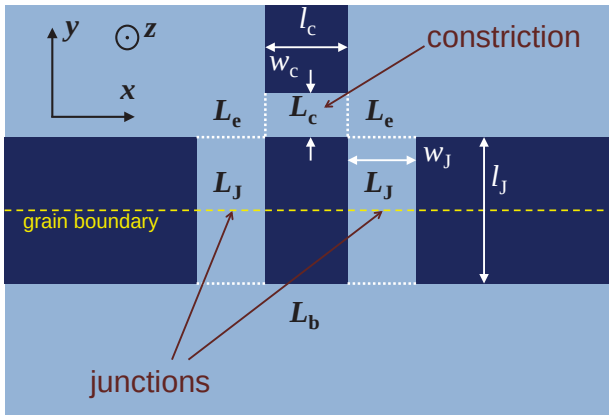

Figure 2.4: Scheme of the SQUID layout with all relevant geometric parameters (constriction width w_c and length l_c, junction width w_J and junction length l_J) and inductances of the constriction L_c, the junctions L_J, the edges L_e and the bottom part L_b. Figure from appended Publication 2. © Institute of Physics and IOP Publishing.

To calculate the flux noise level we used $S_\Phi = f(\beta_L)\Phi_0 k_B T L/I_0 R$ [16] with $f(\beta_L) \approx$

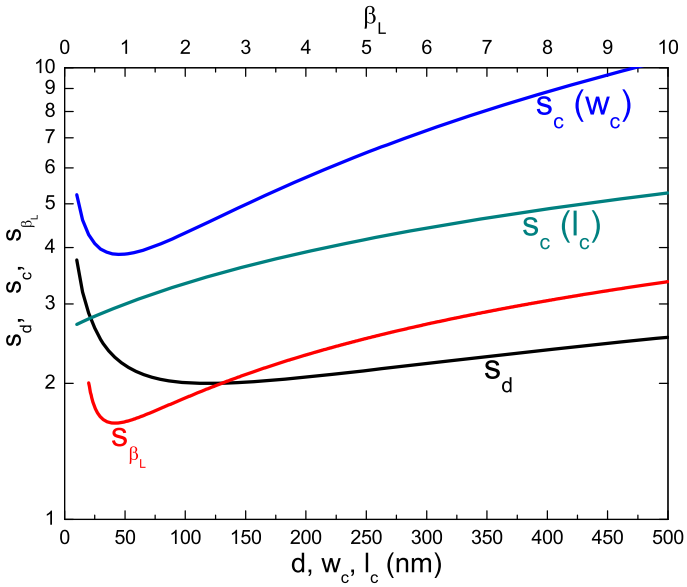

Figure 2.5: Terms contributing to S_μ. $s_c(w_c)$ plotted for $l_c = 200\,\mathrm{nm}$ and $s_c(l_c)$ plotted for $w_c = 50\,\mathrm{nm}$. Figure from appended Publication 2. © Institute of Physics and IOP Publishing.

$4(1+\beta_L)$. Here $\beta_L = 2LI_0/\Phi_0$ is the screening parameter, with the critical current I_0 of the GBJs. By calculating the inductance $L(d, w_c, l_c, w_J, l_J)$ with constriction length l_c, junction width w_J and junction lentgh l_c, we find $S_\Phi(d, w_c, \beta_L)$. With S_Φ and ϕ_μ we obtained a parametrization of the spin sensitivity $S_\mu^{1/2} = S_\Phi^{1/2}/\phi_\mu$. The dependence on the SQUID parameters splits into three parts

$$S_\mu^{1/2} = S_{\mu,0}^{1/2} \cdot s_d(d) \cdot s_{\beta_L}(\beta_L) \cdot s_c(w_c, l_c). \tag{2.1}$$

The contributions to $S_\mu^{1/2}$ are plotted in Fig. 2.5. $s_{\beta_L}(\beta_L)$ shows a clear minimum. The influence of the film thickness d on s_μ is small as long as $d \geq 100\,\mathrm{nm}$, as the decrease in the kinetic inductance and the decrease of the coupling factor almost compensate for each other. $s_c(l_c)$ is plotted for fixed $w_c = 50\,\mathrm{nm}$ and increases with increasing l_c. $s_c(w_c)$ is plotted for fixed $l_c = 200\,\mathrm{nm}$. It shows a clear minimum at $w_{c,min}$. The position and the value of the minimum depend on l_c.

In Fig. 2.6 $S_{\mu,opt}(w_c, l_c)$ is plotted for $d = 120\,\mathrm{nm}$ and $\beta_L = 0.4$. The dashed and dotted lines show $w_{c,min}(l_c)$. With shrinking l_c, $w_{c,min}$ becomes hard to realize. But we can see that even for not ideal w_c, we can achieve spin sensitivities of a few $\mu_B/\mathrm{Hz}^{1/2}$ for a SQUID with optimum film thickness $d = 120\,\mathrm{nm}$ and screening parameter $\beta_L = 0.4$.

This improvement could be achieved by a significant reduction of the SQUID inductance due to a larger film thickness and smaller loop size - especially by minimizing the length of the constriction. Besides calculated values for the spin sensitivity, we also present data for experimental devices with different geometrical parameters. Compared to the theoretically expected values, the experimental ones are slightly

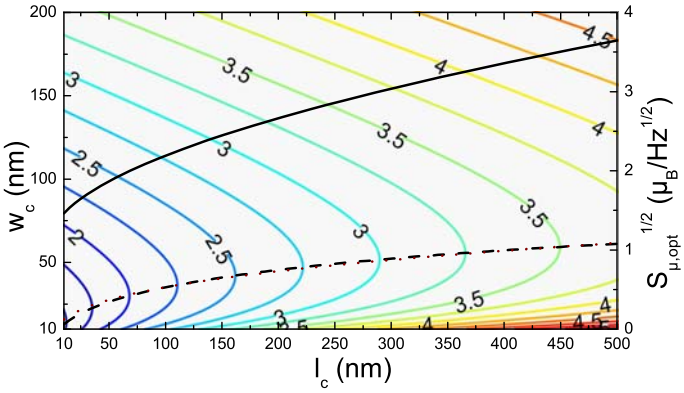

Figure 2.6: The contour plot shows $S_{\mu,opt}(w_c, l_c)$ for $d = 120\,\mathrm{nm}$ and $\beta_L = 0.4$. The dotted and dashed lines show $w_{c,min}(l_c)$. The solid black line shows $S_{\mu,opt}(l_c)$ for $w_c = w_{c,min}$. Figure from appended Publication 2. © Institute of Physics and IOP Publishing.

higher. Still, the achieved best spin sensitivities were of the order of $10\,\mu_B/\mathrm{Hz}^{1/2}$.

In summary, we performed an analysis of the spin sensitivity for YBCO nanoSQUIDs based on GBJs. We predicted that for optimized geometrical parameters spin sensitivities of a few $\mu_B/\mathrm{Hz}^{1/2}$ should be feasible. This can be achieved by realizing YBCO nanoSQUIDs with very low inductance. Compared to the SQUID presented in Publication 1, a significant reduction of the inductance can be achieved by choosing a larger film thickness $d \geq 100\,\mathrm{nm}$ (compared to $d = 50\,\mathrm{nm}$).

Contributions

R. Wölbing developed the methods used for the determination of the coupling factor. Further, he did the main part of the simulations and the data analysis. B. Müller assisted with the simulations and the data analysis. I contributed the experimental data, fabricated the devices and wrote a C based program to automate the numerical simulations.

2.3 Summary of Publication 3:

Low-Noise $YBa_2Cu_3O_7$ Nano Superconducting Quantum Interference Devices for Magnetization Reversal Measurements on Magnetic Nanoparticles

Considering the results of the numerical study presented in Publication 2 we fabricated YBCO nanoSQUIDs with optimized geometrical parameters. We present transport and noise measurements (Fig. 2.8) of one device measured in a magnetically shielded environment at $T = 4.2\,\mathrm{K}$. Due to an increased film thickness $d = 120\,\mathrm{nm}$ and a smaller loop size $350 \times 190\,\mathrm{nm}^2$ (Fig. 2.7) the inductance of the fabricated device $L \approx 4\,\mathrm{pH}$ was almost one order of magnitude lower than the inductance determined for the non-optimized SQUID presented in Publication 1. Further, as the critical current density of the junctions was very high ($j_c \approx 22\,\mathrm{mA}/\mu\mathrm{m}^2$), we could achieve a huge characteristic voltage $V_c = 2\,\mathrm{mV}$. This results in a very low

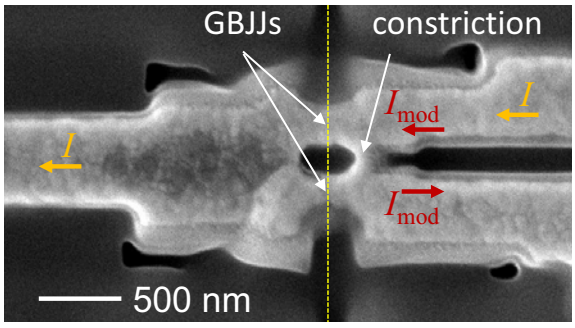

Figure 2.7: SEM image of the YBCO nanoSQUID. Dashed yellow line indicates the position of the grain boundary. Arrows indicate the paths for the modulation current I_{mod} (red) and the bias current I_b (orange).Figure from appended publication 3. © American Physical Society.

flux noise level $S_\Phi^{1/2} = 50\,\mathrm{n}\Phi_0/\mathrm{Hz}^{1/2}$ (Fig. 2.8(a)) in the white noise regime, which corresponds to a calculated spin sensitivity of a few $\mu_B/\mathrm{Hz}^{1/2}$. However, the detected noise spectrum is dominated by low-frequency excess noise up to the cutoff frequency of the readout electronics at 7 MHz.

Typically, two sources of $1/f$ noise in SQUIDs are considered: Abrikosov vortices, that jump between pinning sites and fluctuations of the critical currents of the Josephson junctions. As the measurements were performed in a magnetically shielded environment, the presence of vortices is unlikely. To eliminate noise generated by in-phase and out-of-phase critical current fluctuations we applied a bias reversal readout scheme [46]. However, the low-frequency noise could only be reduced partially below the bias reversal frequency $f_{br} = 260\,\mathrm{MHz}$ (Fig. 2.8(b)).

Hence, we assume that there are some other fluctuators of unknown origin. A pos-

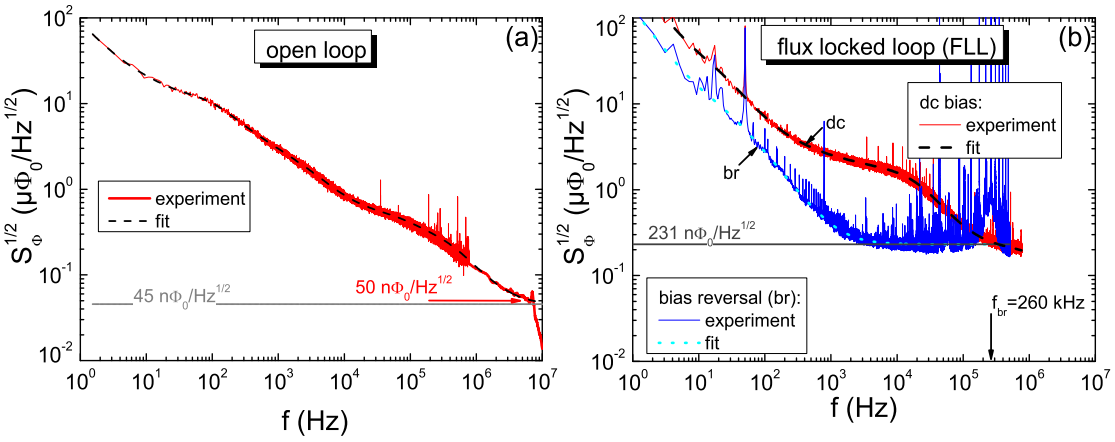

Figure 2.8: Noise spectra of the optimized YBCO nanoSQUID at $T = 4.2\,\mathrm{K}$ in magnetically shielded environment. (a) Flux noise measured in open loop mode. (b) Flux noise measured in flux locked loop mode with dc bias (red) and bias reversal (blue). Dashed and dotted lines indicate fits to the spectra. Horizontal lines indicate the white flux noise level. Figure modified from appended Publication 3. © American Physical Society.

sible explanation are defects [48], especially oxygen vacancies, in the STO substrate that can create ferromagnetic moments. These defects can be caused by the ion milling process.

Such fluctuators have already been observed during other experiments with SQUIDs based on Nb, Pb, PbIn and Al at temperatures below 1 K [49] and different models [50–52] have been developed to explain them. These models consider magnetic moments of electrons in defects or surface spins. To allow for measurements with spin sensitivities of a few $\mu_B/\mathrm{Hz}^{1/2}$ at low frequencies these fluctuators need to be further investigated.

In the second part of the Publication we demonstrate the suitability of the YBCO nanoSQUID as a detector of small spin systems by detecting the magnetization reversal of an iron nanowire encapsulated in a multiwall carbon nanotube (MWCNT). Magnetic nanowires of this type are promising for the use in magnetic force microscopy [53, 54]. The Fe nanowire had a diameter of 39 nm and a length of 13.8 nm. The thickness of the CNT was about 130 nm.

The CNT was positioned close to a non-optimized nanoSQUID with the easy axis of the Fe wire oriented perpendicular to the grain boundary and parallel to the SQUID loop (inclination angle $\approx 4°$) (Fig. 2.9). By applying a magnetic field parallel to the wire axis the magnetization of the particle could be switched and the change in the stray field was detected directly with the nanoSQUID operated in a flux locked

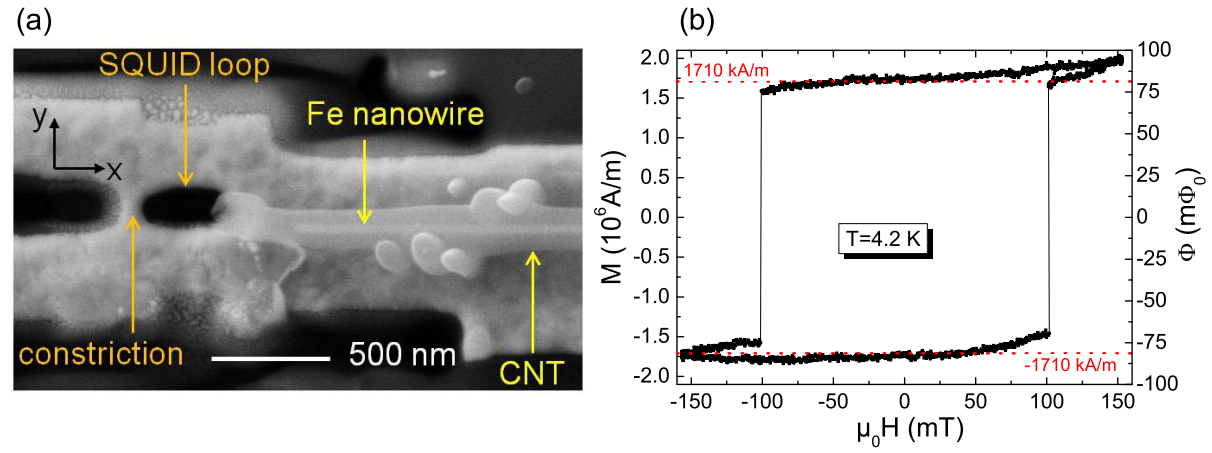

Figure 2.9: (a) SEM image of the nanoSQUID with the iron filled CNT attached close to the loop. (b) Hysteresis curve of the nanowire detected with the SQUID at $T = 4.2\,\mathrm{K}$. Switching of magnetization can be observed at $B = \pm 101\,\mathrm{mT}$ Dotted red lines indicates the literature value for the saturation magnetization. Figure modified from appended Publication 3. © American Physical Society.

loop mode. Compared to measurements that were done before on a similar nanowire with a micro-Hall bar [55], we could achieve a significantly higher signal to noise ratio. The observed nucleation field $H_n \approx 100\,\mathrm{mT}$ is in very good agreement with the theoretically predicted value for a switching of the magnetization via curling mode. Further, we estimated the flux coupling into the SQUID loop for the fully magnetized iron nanowire by integrating the coupling factor over the volume of the nanowire. Again we find very good agreement between the calculated and the detected signal.

The supplemental material to Publication 3 contains data of an additional SQUID. We present noise spectra measured at different temperatures in dc bias mode and in bias reversal mode. As for the SQUID presented in the main article the noise spectra are dominated by frequency-dependent excess noise up to the cutoff frequency of the readout electronis. Applying a bias reversal readout scheme could only suppress the f-dependent noise for frequencies above $\approx 1\,\mathrm{kHz}$. For all obtained spectra there is no systematic temperature dependence of the excess noise observable.

Further, we show the characteristics of the SQUID we used for the measurement of nanowire. This device had a film thickness of $d = 75\,\mathrm{nm}$, which results in a higher inductance $L \approx 28\,\mathrm{pH}$ and hence a higher flux noise level $S_\Phi^{1/2} \leq 1.5\,\mu\Phi_0/\mathrm{Hz}^{1/2}$ compared to the devices with optimum film thickness $d = 120\,\mathrm{nm}$. In the last part of the supplemental material we show a detailed analysis of the noise spectra presented in the main article. We used an algorithm [56] to decompose the spectra

into a sum of several Lorentzians, a $1/f^2$ part and a white noise contribution. We observed that some of the Lorentzians necessary to fit the spectra, i.e. those that are caused by critical current fluctuations, can be eliminated by bias reversal. The remaining fluctuators must have a magnetic origin.

In conclusion, we fabricated YBCO nanoSQUIDs based on GBJs with optimized spin sensitivity. The main improvement, compared to the nanoSQUID presented in Publication 1, could be achieved by using a larger film thickness $d = 120\,\mathrm{nm}$ that lead to a decrease of the inductance $L \approx 4\,\mathrm{pH}$ of the SQUID by approximately one order of magnitude. The experimentally determined upper limit for the flux noise $\approx 50\,\mathrm{n}\Phi_0/\mathrm{Hz}^{1/2}$ constitutes an improvement by more than an order of magnitude over the lowest flux noise values of the best YBCO SQUIDs reported so far in literature. The noise spectra were dominated by low-frequency excess noise, that could only be partially reduced by a bias reversal readout scheme. Hence, this excess noise must be partially caused by magnetic fluctuators. The origin of these fluctuators is not yet clear. But they could possibly be caused by surface defects in the substrate. In the second part, we detected the magnetization reversal of a Fe nanowire. The measured magnetization curve is in good agreement with theoretical predictions. Hence, we could show that one central aim of this thesis, the development of nanoSQUIDs for the detection of small spin systems, could be achieved.

Contributions

This work was done in a collaboration with the group of B. Büchner at the IFW Dresden that provided the nanowire. The positioning of the wire was done by C. F. Reiche at the IFW Dresden. R. Wölbing did the simulations of the coupling factor and determined the optimum SQUID parameters. B. Müller contributed to the measurements at variable temperature. M. J. Martínez-Pérez assisted with the measurements and the interpretation of the results. For this work I fabricated the SQUIDs and performed the measurements at 4.2 K. I did parts of the simulations and assisted with the measurements at variable temperature. In collaboration with R. Wölbing, I optimized the measurement setup and the readout electronics.

2.4 Summary of Publication 4:

Nb nano superconducting quantum interference devices with high spin sensitivity for operation in magnetic fields up to 0.5 T

In Publication 4 we present a nanoSQUID with Nb/HfTi/Nb Josephson junctions. Compared to junctions based on conventional Nb/Al-AlO_x/Nb trilayer technology these intrinsically shunted junctions show very large critical current densities and non-hysteretic IV-characteristics. This allows for a miniaturization of the SQUIDs, keeping the advantages of the trilayer technology, that is much more flexible in design than the 2-dimensional layout of SQUIDs based on cJJs or GBJs. A first

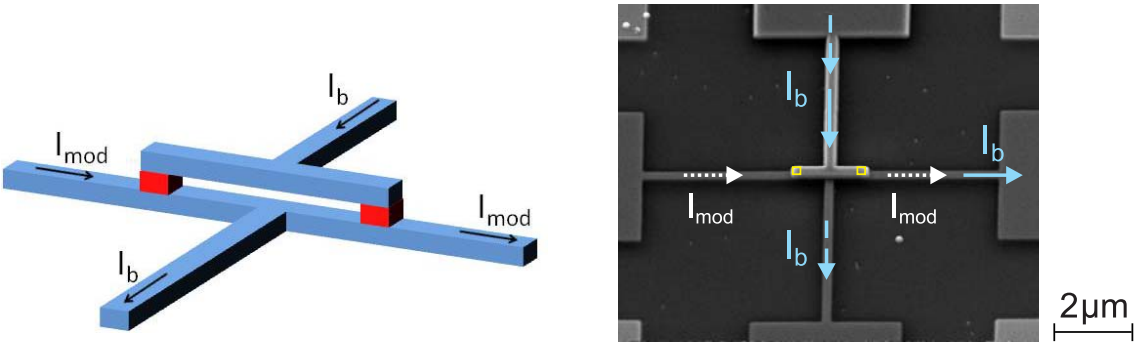

Figure 2.10: Left: Scheme of the Nb nanoSQUID. Arrows indicate current paths. Right: SEM image of the Nb nanoSQUID. Yellow rectangles indicate the position of the Josephson junctions. Arrows indicate the paths for the modulation current (dashed) and for the bias current (dashed: symmetric bias, solid: asymmetric bias). Figure modified from appended Publication 4. © American Physical Society.

generation of this type of SQUIDs is presented in [38].
The second generation that is discussed in this publication has been improved in terms of high field suitability by developing a new SQUID layout (see Fig. 2.10). For these devices the SQUID loop is oriented perpendicular to the substrate. Now, for magnetization reversal measurements a magnetic field can be applied parallel to the SQUID loop without coupling flux into the junctions. Additionally, as for the YBCO SQUIDs discussed in Publication 1, a modulation line was implemented. By applying a modulation current I_{mod} the SQUID can be flux biased at the optimum working point.

The SQUIDs were fabricated at the PTB Braunschweig using electron beam lithography and argon ion milling. Junctions with a size of $200 \times 200\,\mathrm{nm}^2$ were realized.

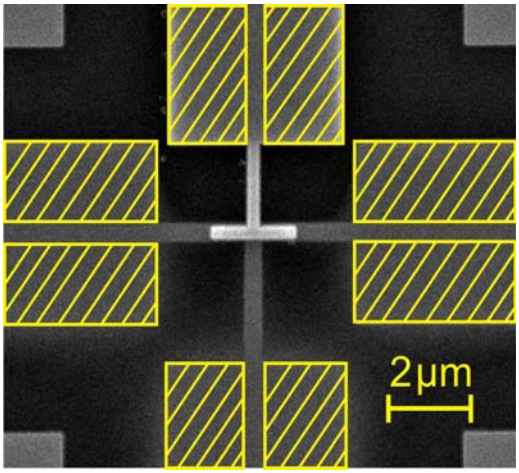

Figure 2.11: Nb nanoSQUID after reducing the widths of the connection lines by FIB milling as indicated by the yellow areas. Figure modified from appended Publication 4. © American Physical Society.

Experimental data of two nanoSQUIDs at $T = 4.2\,\mathrm{K}$ is presented in this publication.

Transport measurements were performed in a magnetically shielded environment. The IVCs were non-hysteretic and we could determine characteristic voltages $V_c = I_0 R \approx 50\,\mu\mathrm{V}$ and extremely low inductances $L \approx 2 \ldots 3\mathrm{pH}$.

Flux noise spectra were measured in a two-stage configuration [46] with a Nb SQUID amplifier at $T = 4.2\,\mathrm{K}$. The obtained spectra are dominated by frequency dependent noise up to the cutoff frequency $f_{3dB} \approx 10\,\mathrm{kHz}$. By fitting the experimental data we could determine a very low flux noise level $S_\Phi^{1/2} = 200\,\mathrm{n}\Phi_0/\mathrm{Hz}^{1/2}$.

With a calculated coupling factor $\phi_\mu = 8.6\,\mathrm{n}\Phi_0/\mu_B$, for a particle with magnetic moment $\vec{\mu}$ oriented perpendicular to the substrate plane with a distance of 10 nm to the SQUID loop, we obtained a spin sensitivity $S_\mu^{1/2} = 23\,\mu_B/\mathrm{Hz}^{1/2}$.

In the second part of the publication we present the high-field performance of the Nb nanoSQUIDs. The SQUIDs were installed in a high-field setup with a superconducting split-coil magnet and aligned using two goniometers with perpendicular tilt axes and a rotator. Aligning the magnetic field perpendicular to the substrate plane prevents coupling of the field into the SQUID loop or into the Josephson junctions. The high field operation was limited by the penetration of Abrikosov vortices, but could be improved by reducing the widths of the connection lines close to the SQUID by focused ion beam milling (Fig. 2.11).

For the next generation of SQUIDs these changes in the SQUID layout were implemented and enabled stable operation up to $B = 50\,\mathrm{mT}$ with only a slight suppression of the critical current (Fig. 2.12(a)). Also the white flux noise level $S_\Phi^{1/2} = 240\,\mathrm{n}\Phi_0/\mathrm{Hz}^{1/2}$ (Fig. 2.12(b)) does not increase significantly at $B = 50\,\mathrm{mT}$.

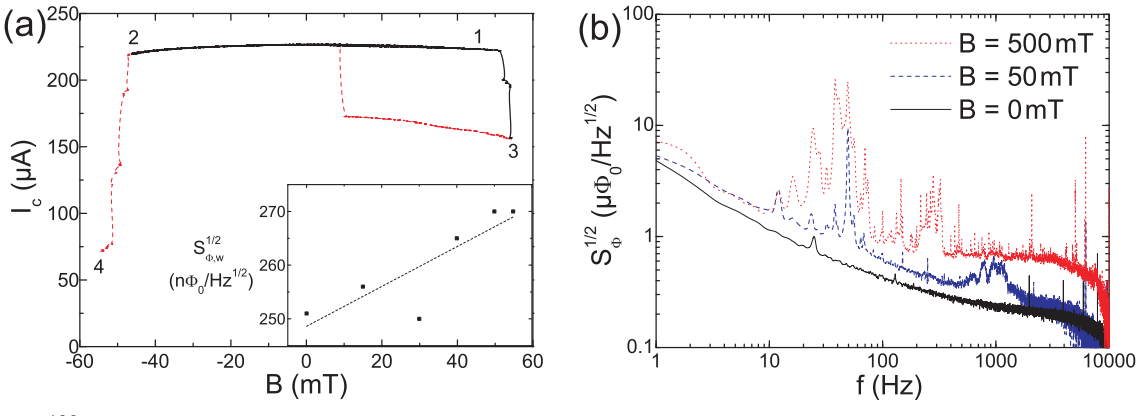

Figure 2.12: Nb nanoSQUID at $T = 4.2\,\mathrm{K}$. (a) $I_c(B)$ for the optimized SQUID layout. Black line: sweep sequence 1-3, red line plus symbols: sweep sequence 3-4. (b) Flux noise spectra for $B = 0\,\mathrm{mT}$, $50\,\mathrm{mT}$ and $500\,\mathrm{mT}$. Figure modified from appended Publication 4. © American Physical Society.

Even in stronger fields up to $B = 0.5\,\mathrm{T}$ the SQUIDs could be operated with high sensitivity $S_\Phi^{1/2} \approx 680\,\mathrm{n}\Phi_0/\mathrm{Hz}^{1/2}$ (Fig. 2.12).

In summary, we developed Nb nanoSQUIDs with HfTi junctions with an implemented flux modulation line. We determined a very low flux noise level and a high spin sensitivity of the nanoSQUIDs. As the SQUID loop and the junction barrier is perpendicular to the substrate, stable operation of the SQUIDs in fields up to 50 mT is possible. Good noise performance of the nanoSQUIDs can be observed even in high magnetic fields $B = 0.5\,\mathrm{T}$.

Contributions

This work was done in a collaboration with the PTB Braunschweig with the group of J. Kohlmann and A. W. Zorin. The samples were fabricated by O. Kieler and T. Weimann. R. Wölbing performed the transport and noise measurements. J. Nagel assisted with the measurements and developed the sample design. M. Kemmler assisted with the interpretation of the results. For this work I did the FIB milling to reduce the widths of the connection lines and assisted with the noise measurements.

List of acronyms and physical constants

List of acronyms

cJJ	constriction type Josephson junction
CNT	carbon nanotube
dc	direct current
FeCNT	iron-filled carbon nanotube
FIB	focused ion beam
GBJ	grain boundary junction
IVC	current-voltage characteristics
MNP	magnetic nanoparticle
MW-CNT	multiwall carbon nanotube
SDP	single domain particle
SEM	scanning electron microscopy
SIS	superconductor/insulator/superconductor
SNS	superconductor/normal metal/superconductor
SOT	SQUID-on-tip
STO	strontium titanate ($SrTiO_3$)
SQUID	superconducting quantum interference device
YBCO	yttrium barium copper oxide ($YBa_2Cu_3O_7$)

List of physical constants

$\Phi_0 = 2.07 \cdot 10^{-15}\,\mathrm{Tm}^2$	magnetic flux quantum
$\mu_B = 9.27 \cdot 10^{-24}\,\mathrm{J/T}$	Bohr magneton
$\mu_0 = 1.26 \cdot 10^{-6}\,\mathrm{Tm/A}$	vacuum permeability
$k_B = 1.38 \cdot 10^{-}23\,\mathrm{J/K}$	Boltzmann constant

Bibliography

[1] Juan Bartolomé, Fernando Luis, and Julio F. Fernández, editors. *Molecular Magnets: Physics and Applications*. NanoScience and Technology. Springer, Heidelberg, 2014.

[2] Lapo Bogani and Wolfgang Wernsdorfer. Molecular spintronics using single-molecule magnets. *Nature Materials*, 7:179–186, 2008.

[3] Michael N. Leuenberger and Daniel Loss. Quantum computing in molecular magnets. *Nature*, 410:789–793, 2001.

[4] S. Odenbach (ed.). Ferrofluids. *J. Phys: Condens. Matter*, 18 (38):special issue, 2006.

[5] Andreas Jordan, Regina Scholz, Peter Wust, Horst Fähling, and Roland Felix. Magnetic fluid hyperthermia (MFH): Cancer treatment with AC magnetic field induced excitation of biocompatible superparamagnetic nanoparticles. *J. Magn. Magn. Mat.*, 201:413–419, 1999.

[6] R. C. Semelka and T. K. G. Helmberger. State of the art: Contrast agents for mr imaging of the liver. *Radiology*, 218:27–38, 2001.

[7] R. Klingeler, S. Hampel, and B. Büchner. Carbon nanotube based biomedical agents for heating, temperature sensoring and drug delivery. *Int. J. Hyperthermia*, 24:496, 2008.

[8] S. N. Piramanayagam and K. Srinivasan. Recording media research for future hard disk drives. *J. Magn. Magn. Mat.*, volume 321, issue 6:485–494, 2009.

[9] Q. A. Pankhurst, N. T. K. Thanh, S. K. Jones, and J. Dobson. Progress in applications of magnetic nanoparticles in biomedicine. *J. Phys. D: Appl. Phys.*, 42:224001 (15pp), 2009.

[10] S. C. McBain, H. H. P. Yiu, and J. Dobson. Magnetic nanoparticles for gene and drug delivery. *Int. J. Nanomed.*, 3:169–80, 2008.

[11] K. Ohno, C. Mori, T. Akashi, S. Yoshida, Y. Tago, Y. Tsujii, and Y. Tabata. Fabrication of contrast agents for magnetic resonance imaging from polymer-brush-afforded iron oxide magnetic nanoparticles prepared by surface-initiated living radical polymerization. *Biomacromolecules*, 14 (10):pp 3453–3462, 2013.

[12] B. Thiesen and A. Jordan. Clinical applications of magnetic nanoparticles for hyperthermia. *Int. J. Hyperthermia*, 24 (6):467–74, 2008.

[13] W. Wernsdorfer. Classical and quantum magnetization reversal studied in nanometersized particles and clusters. *Adv. Chem. Phys.*, 118:99–190, 2001.

[14] B. Chesca, R. Kleiner, and D. Koelle. *SQUID Theory*, volume 1: Fundamentals and Technology of SQUIDs and SQUID systems, chapter 2, pages 29–92. Wiley-VCH, Weinheim, 2004.

[15] B. D. Josephson. The discovery of tunnelling supercurrents. *Rev. Mod. Phys.*, 46:251–254, 1974.

[16] D. Koelle, R. Kleiner, F. Ludwig, E. Dantsker, and John Clarke. High-transition-temperature superconducting quantum interference devices. *Rev. Mod. Phys.*, 71:631–686, 1999.

[17] D. D. Awschalom, J. R. Rozen, M. B. Ketchen, W. J. Gallagher, A. W. Kleinsasser, R. L. Sandstrom, and B. Bumble. Low-noise modular microsusceptometer using nearly quantum limited dc SQUIDs. *Appl. Phys. Lett.*, 53:2108–2110, 1988.

[18] M. Ketchen, D. Awschalom, W. Gallagher, A. Kleinsasser, R. Sandstrom, J. Rozen, and B. Bumble. Design, fabrication, and performance of integrated miniature SQUID susceptometers. *IEEE Trans. Magn.*, 25:1212–1215, 1989.

[19] K. Hasselbach, D. Mailly, and J. R. Kirtley. Micro-superconducting quantum interference device characteristic. *J. Appl. Phys.*, 911:4432–4437, 2002.

[20] S. K. H. Lam and D. L. Tilbrook. Development of a niobium nanosuperconducting quantum interference device for the detection of small spin populations. *Appl. Phys. Lett.*, 82:1078–1080, 2003.

[21] J.-P. Cleuziou, W. Wernsdorfer, V. Bouchiat, T. Ondarçuhu, and M. Monthioux. Carbon nanotube superconducting quantum interference device. *Nature Nanotech.*, 1:53–59, 2006.

[22] Aico G. P. Troeman, Hendrie Derking, Bert Borger, Johannes Pleikies, Dick Veldhuis, and Hans Hilgenkamp. NanoSQUIDs based on niobium constrictions. *Nano Lett.*, 7:2152–2156, 2007.

[23] Nicholas C. Koshnick, Martin E. Huber, Julie A. Bert, Clifford W. Hicks, Jeff Large, Hal Edwards, and Kathryn A. Moler. A terraced scanning supper conducting quantum interference device susceptometer with submicron pickup loops. *Appl. Phys. Lett.*, 93:243101, 2008.

[24] L. Hao, J. C. Macfarlane, J. C. Gallop, D. Cox, J. Beyer, D. Drung, and T. Schurig. Measurement and noise performance of nano-superconducting-quantum-interference devices fabricated by focused ion beam. *Appl. Phys. Lett.*, 92(19):192507, 2008.

[25] C. P. Foley and H. Hilgenkamp. Why NanoSQUIDs are important: an introduction to the focus issue. *Supercond. Sci. Technol.*, 22:064001, 2009.

[26] V. Bouchiat. Detection of magnetic moments using a nano-squid: limits of resolution and sensitivity in near-field squid magnetometry. *Supercond. Sci. Technol.*, 22:064002, 2009.

[27] W. Wernsdorfer. From micro- to nano-SQUIDs: applications to nanomagnetism. *Supercond. Sci. Technol.*, 22:064013, 2009.

[28] Francesco Giazotto, Joonas T. Peltonen, Matthias Meschke, and Jukka P. Pekola. Superconducting quantum interference proximity transistor. *Nature Phys.*, 6:254–259, 2010.

[29] M. J. Martínez-Pérez, E. Bellido, R. de Miguel, J. Sesé, A. Lostao, C. Gómez-Moreno, D. Drung, T. Schurig, D. Ruiz-Molina, and F. Luis. Alternating current magnetic susceptibility of a molecular magnet submonolayer directly patterned onto a micro superconducting quantum interference device. *Appl. Phys. Lett.*, 99:032504, 2011.

[30] E. J. Romans, S. Rozhko, L. Young, A. Blois, L. Hao, D. Cox, and J. C. Gallop. Noise performance of niobium nano-SQUIDs in applied magnetic fields. *IEEE Trans. Appl. Supercond.*, 21:404–407, 2011.

[31] R. Russo, C. Granata, E. Esposito, D. Peddis, C. Cannas, and A. Vettoliere. Nanoparticle magnetization measurements by a high sensitive nano-superconducting quantum interference device. *Appl. Phys. Lett.*, 101:122601, 2012.

[32] Carmine Granata, Antonio Vettoliere, Roberto Russo, Matteo Fretto, Natascia De Leo, and Vincenzo Lacquaniti. Three-dimensional spin nanosensor based on reliable tunnel Josephson nano-junctions for nanomagnetism investigations. *Appl. Phys. Lett.*, 103:102602, 2013.

[33] D. Drung, J.-H. Storm, F. Ruede, A. Kirste, M. Regin, T. Schurig, A. M. Repollés, J. Sesé, and F. Luis. Thin-film microsusceptometer with integrated nanoloop. *IEEE Trans. Appl. Supercond.*, 24:1600206, 2014.

[34] Amit Finkler, Yehonathan Segev, Yuri Myasoedov, Michael L. Rappaport, Lior Ne'eman, Denis Vasyukov, Eli Zeldov, Martin E. Huber, Jens Martin, and Amir Yacoby. Self-aligned nanoscale SQUID on a tip. *Nano Lett.*, 10:1046–1049, 2010.

[35] R. Arpaia, M. Arzeo, S. Nawaz, S. Charpentier, F. Lombardi, and T. Bauch. Ultra low noise $YBa_2Cu_3O_{7-\delta}$ nano superconducting quantum interference devices implementing nanowires. *App. Phys. Lett.*, 104:072603, 2014.

[36] Denis Vasyukov, Yonathan Anahory, Lior Embon, Dorri Halbertal, Jo Cuppens, Lior Ne'eman, Amit Finkler, Yehonathan Segev, Yuri Myasoedov, Michael L. Rappaport, Martin E. Huber, and Eli Zeldov. A scanning superconducting quantum interference device with single electron spin sensitivity. *Nature Nanotechnol.*, 8:639–644, 2013.

[37] Yonathan Anahory, Jonathan Reiner, Lior Embon, Dorri Halbertal, Anton Yakovenko, Yuri Myasoedov, Michael L. Rappaport, Martin E. Huber, and Eli Zeldov. Three-junction SQUID-on-tip with tunable in-plane and out-of-plane magnetic field sensitivity. *Nano Letters*, 2014.

[38] J. Nagel, O. F. Kieler, T. Weimann, R. Wölbing, J. Kohlmann, A. B. Zorin, R. Kleiner, D. Koelle, and M. Kemmler. Superconducting quantum interference devices with submicron Nb/HfTi/Nb junctions for investigation of small magnetic particles. *Appl. Phys. Lett.*, 99:032506, 2011.

[39] R. Wölbing, J. Nagel, T. Schwarz, O. Kieler, T. Weimann, J. Kohlmann, A. B. Zorin, M. Kemmler, R. Kleiner, and D. Koelle. Nb nano superconducting quan-

tum interference devices with high spin sensitivity for operation in magnetic fields up to 0.5 T. *Appl Phys. Lett.*, 102:192601, 2013.

[40] J. Nagel, A. Buchter, F. Xue, O. F. Kieler, T. Weimann, J. Kohlmann, A. B. Zorin, D. Rüffer, E. Russo-Averchi, R. Huber, P. Berberich, A. Fontcuberta i Morral, D. Grundler, R. Kleiner, D. Koelle, M. Poggio, and M. Kemmler. Nanoscale multifunctional sensor formed by a Ni nanotube and a scanning Nb nanoSQUID. *Phys. Rev. B*, 88:064425, 2013.

[41] A. Buchter, J. Nagel, D. Rüffer, F. Xue amd D. P. Weber, O. F. Kieler, T. Weimann, J. Kohlmann, A. B. Zorin, E. Russo-Averchi, R. Huber, P. Berberich, A. Fontcuberta i Morral, M. Kemmler, R. Kleiner, D. Koelle, D. Grundler, and M. Poggio. Reversal mechanism of an individual Ni nanotube simultaneously studied by torque and SQUID magnetometry. *Phys. Rev. Lett.*, 111:067202, 2013.

[42] J. Nagel, K. B. Konovalenko, M. Kemmler, M. Turad, R. Werner, E. Kleisz, S. Menzel, R. Klingeler, B. Büchner, R. Kleiner, and D. Koelle. Resistively shunted $YBa_2Cu_3O_7$ grain boundary junctions and low-noise SQUIDs patterned by a focused ion beam down to 80 nm linewidth. *Supercond. Sci. Technol.*, 24:015015, 2011.

[43] T. Schwarz, J. Nagel, R. Wölbing, M. Kemmler, R. Kleiner, and D. Koelle. Low-noise nano superconducting quantum interference device operating in tesla magnetic fields. *ACS Nano*, 7:844–850, 2013.

[44] R. Wölbing, T. Schwarz, B. Müller, J. Nagel, M. Kemmler, R. Kleiner, and D. Koelle. Optimizing the spin sensitivity of grain boundary junction nanoSQUIDs – towards detection of small spin systems with single-spin resolution. *Supercond. Sci. Technol., in press*, 2014.

[45] A. Leonhardt, S. Hampel, C. Müller, I. Mönch, R. Koseva, M. Ritschel, D. Elefant, K. Biedermann, and B. Büchner. Synthesis, properties, and applications of ferromagnetic-filled carbon nanotubes. *Chem. Vap. Deposition*, 12:380–387, 2006.

[46] D. Drung and M. Mück. *SQUID Electronics*, volume 1: Fundamentals and Technology of SQUIDs and SQUID systems, chapter 4, pages 127–170. Wiley-VCH, Weinheim, 2004.

[47] M. Khapaev, M. Kupriyanov, E. Goldobin, and M. Siegel. Current distribution simulation for superconducting multi-layered structures. *Supercond. Sci. Technol.*, 16:24–27, 2003.

[48] K. Potzger, J.Osten, A. A.Levin, A.Shalimov, G.Talut, H.Reuther, S.Arpaci, D. Bürger, H. Schmidt, T.Nestler, and D. C.Meyer. Defect-induced ferromagnetism in crystalline $SrTiO_3$. *J. Magn. Magn. Mater.*, 323:1551–1562, 2011.

[49] D. Drung, J. Beyer, J.-H. Storm, M. Peters, and T. Schurig. Investigation of low-frequency excess flux noise in dc SQUIDs at mK temperatures. *IEEE Trans. Appl. Supercond.*, 21:340–344, 2011.

[50] Roger H. Koch, David P. DiVincenzo, and John Clarke. Model for $1/f$ flux noise in SQUIDs and qubits. *Phys. Rev. Lett.*, 98:267003, 2007.

[51] Rogerio de Sousa. Dangling-bond spin relaxation and magnetic 1?f noise from the amorphous-semiconductor/oxide interface: Theory. *Phys. Rev. B*, 76:245306, 2007.

[52] S. Sendelbach, D. Hover, A. Kittel, M. Mück, John M. Martinis, and R. McDermott. Magnetism in SQUIDs at millikelvin temperatures. *Phys. Rev. Lett.*, 100:227006, 2008.

[53] A. Winkler, T. Mühl, S. MenS. Menzel. Kozhuharova-Koseva, S. Hampel, A. Leonhardt, and B. Büchner. Magnetic force microscopy sensors using iron-filled carbon nanotubes. *J. Appl. Phys.*, 2006.

[54] T. Mühl, J. Körner, S. Philippi, C. F. Reiche, A. Leonhardt, and B. Büchner. Magnetic force microscopy sensors providing in-plane and perpendicular sensitivity. *App. Phys. Lett.*, 101:112401, 2012.

[55] K. Lipert, S. Bahr, F. Wolny, P. Atkinson, U. Weißker, T. Mühl, O. G. Schmidt, B. Büchner, and R. Klingeler. An individual iron nanowire-filled carbon nanotube probed by micro-Hall magnetometry. *App. Phys. Lett.*, 97:212503, 2010.

[56] E. Sassier, R. Kleiner, and D. Koelle. A spectroscopic method for excess-noise spectrum analysis. unpublished.

Appended publications

Publication 1

Low-Noise Nano Superconducting Quantum Interference Device Operating in Tesla Magnetic Fields

Tobias Schwarz, Joachim Nagel, Roman Wölbing, Matthias Kemmler, Reinhold Kleiner, and Dieter Koelle*

Physikalisches Institut—Experimentalphysik II and Center for Collective Quantum Phenomena in LISA$^+$, Universität Tübingen, Auf der Morgenstelle 14, D-72076 Tübingen, Germany

ABSTRACT Superconductivity in the cuprate $YBa_2Cu_3O_7$ (YBCO) persists up to huge magnetic fields (B) up to several tens of Teslas, and sensitive direct current (dc) superconducting quantum interference devices (SQUIDs) can be realized in epitaxially grown YBCO films by using grain boundary Josephson junctions (GBJs). Here we present the realization of high-quality YBCO nanoSQUIDs, patterned by focused ion beam milling. We demonstrate low-noise performance of such a SQUID up to $B = 1$ T applied parallel to the plane of the SQUID loop at the temperature $T = 4.2$ K. The GBJs are shunted by a thin Au layer to provide nonhysteretic current voltage characteristics, and the SQUID incorporates a 90 nm wide constriction which is used for on-chip modulation of the magnetic flux through the SQUID loop. The white flux noise of the device increases only slightly from 1.3 $\mu\Phi_0/(\mathrm{Hz})^{1/2}$ at $B = 0$ to 2.3 $\mu\Phi_0/(\mathrm{Hz})^{1/2}$ at 1 T. Assuming that a point-like magnetic particle with magnetization in the plane of the SQUID loop is placed directly on top of the constriction and taking into account the geometry of the SQUID, we calculate a spin sensitivity $S_\mu^{1/2} = 62\ \mu_B/(\mathrm{Hz})^{1/2}$ at $B = 0$ and 110 $\mu_B/(\mathrm{Hz})^{1/2}$ at 1 T. The demonstration of low noise of such a SQUID in Tesla fields is a decisive step toward utilizing the full potential of ultrasensitive nanoSQUIDs for direct measurements of magnetic hysteresis curves of magnetic nanoparticles and molecular magnets.

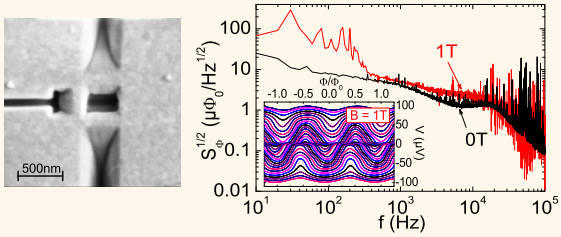

KEYWORDS: YBCO · SQUID · superconductivity · nanofabrication · flux noise · spin sensitivity · magnetic particle detection

Growing interest in the detection and investigation of small spin systems like single-molecular/single-chain magnets,[1,2] cold atom clouds,[3] or even single electrons/atoms[4] demands for sensors that are sensitive to very small changes of the magnetization of small particles with the ultimate goal of single spin detection. The interest for the investigation of such particles affects many fields of research such as material science, chemistry, information technology, medical and biological science, or studies of quantum effects in mesoscopic matter. In order to meet the challenge of detecting a single electron spin, various techniques such as magnetic resonance force microscopy,[5] magneto-optic spin detection,[6,7] and scanning tunneling microscopy assisted electron spin resonance[8,9] have been adapted.

In contrast to these techniques, miniaturized Hall bars[10,11] or direct current (dc) superconducting quantum interference devices (SQUIDs)[12−29] offer the possibility of measuring directly magnetization changes in small spin systems by probing changes of the particle's stray magnetic field or magnetic flux coupled to the Hall bars or SQUIDs, respectively. Such devices can be operated continuously as field-to-voltage or flux-to-voltage converters (for dc SQUIDs with nonhysteretic Josephson junctions), allowing one to investigate magnetization dynamics of the sample under investigation. Indeed, apart from pioneering work by Wernsdorfer *et al.* using microSQUIDs for the measurements of the magnetization of nanoparticles,[13] recent publications reported on preliminary measurements of small clusters of nanoparticles by using nanoSQUIDs with a flux capture area below 1 μm^2.[22,26,30]

For SQUIDs, scaling down their size to the submicrometer range offers the possibility to reach extremely low values of the spectral density of flux noise power S_Φ (*via* reduction of the inductance L of the SQUID loop).[31] Furthermore, by placing a magnetic particle on top of a very narrow constriction intersecting the SQUID loop, one can achieve a large coupling factor $\phi_\mu \equiv \Phi/\mu$, that is, the amount of magnetic flux Φ

* Address correspondence to koelle@uni-tuebingen.de.

Received for review November 22, 2012 and accepted December 19, 2012.

Published online December 19, 2012
10.1021/nn305431c

which is coupled by a particle with magnetic moment μ to the SQUID loop. Hence, it has been proposed that nanoSQUIDs may reach spin sensitivities $S_\mu^{1/2} \equiv S_\Phi^{1/2}/\phi_\mu$ of only a few $\mu_B/(\mathrm{Hz})^{1/2}$,[32] where μ_B is the Bohr magneton. Taking $\phi_\mu \approx 20\ n\Phi_0/\mu_B$, for example, which is achievable as we demonstrate below, a spin sensitivity of 1 $\mu_B/(\mathrm{Hz})^{1/2}$ requires an ultralow rms flux noise $S_\Phi^{1/2} = 20\ n\Phi_0/(\mathrm{Hz})^{1/2}$ (Φ_0 is the magnetic flux quantum). We note that state-of-the art, nonminiaturized dc SQUIDs reach values for $S_\Phi^{1/2}$ on the order of 1 $\mu\Phi_0/(\mathrm{Hz})^{1/2}$.[33] However, for very low inductance SQUIDs, values of $S_\Phi^{1/2}$ down to $\sim$20 $n\Phi_0/(\mathrm{Hz})^{1/2}$ have been demonstrated indeed.[31]

So why have we not seen demonstrations of measurements of magnetization reversals of small magnetic particles by using ultrasensitive dc nanoSQUIDs so far? The reason for this is that such measurements typically require the application of very strong magnetic fields in the Tesla range,[13] while very low flux noise in SQUIDs has been demonstrated only for operation of such SQUIDs in the earth's magnetic field ($\sim$60 μT) or, more typically, in a magnetically well-shielded environment in the nT range (*i.e.*, 9 orders of magnitude lower magnetic fields).[33]

Miniaturized nanoSQUIDs based on very thin Nb films with constriction-type Josephson junctions have been operated in impressive background fields in the Tesla range.[34,27] Chen *et al.*[34] achieved operation in fields up to 7 T for SQUIDs made of $d \sim 5.5$ nm thin Nb films. However, there are two drawbacks in this design. First, the very low thickness of the Nb film causes the (kinetic) SQUID inductance L ($\propto 1/d$) and consequently the SQUID flux noise power S_Φ ($\propto L$) to be large,[35] at least 4 orders of magnitude above the values obtained for sensitive state-of-the-art SQUIDs. Second, the constriction junctions have a hysteretic current voltage characteristic (IVC). This prevents continuous measurements and the use of advanced readout schemes,[36] which are required for ultrasensitive dc SQUIDs. Similar values for the flux noise (at $B \sim 0.3$ T) have been reported very recently for boron-doped diamond μ-SQUIDs based on constriction junctions, which operated up to 4 T.[29] For $B > 0.5$ T, the IVCs became nonhysteretic; however, noise data at such high fields have not been reported, and the very low transfer function $V_\Phi \equiv (\partial V/\partial\Phi)_{max} \approx 0.5\ \mu V/\Phi_0$ at $B = 1$ T implies probably similar noise performance as for lower fields (V is the voltage across the SQUID).

We should note here that very sensitive Nb thin film (d = 200 nm) nanoSQUIDs based on nonhysteretic constriction type junctions, resistively shunted with a 150 nm thick W layer, have been realized with $S_\Phi^{1/2} = 0.2\ \mu\Phi_0/(\mathrm{Hz})^{1/2}$.[37] However, these devices are probably only suited for operation in subTesla fields[38] and show optimum performance only in a narrow temperature range not too far below the transition temperature (T_c) of Nb. This makes them less interesting for applications which are most promising for temperatures of a few Kelvin and well below.[13]

In order to fully exploit the potential of SQUIDs, there is thus a clear need to develop sensitive nanoSQUIDs with nonhysteretic IVCs that at the same time can be operated in strong background fields. As for the SQUIDs with constriction junctions, such SQUIDs should incorporate at least one very thin and/or narrow section where the magnetic particle is placed, allowing for a good coupling of the magnetic stray field of the particle to the SQUID. This all calls for a superconductor which has a very high critical field and allows for patterning nanosized structures and not too large Josephson junctions. The cuprate superconductor $YBa_2Cu_3O_7$ (YBCO) fulfills these requirements. Compared to Nb, YBCO is not a mature material and even the most reliable type of YBCO Josephson junctions, such as grain boundary junctions (GBJs), exhibit a large $1/f$ noise as well as an appreciable scatter in their electrical parameters.[39,40] Nonetheless, based on a recently developed process for fabricating high-quality submicrometer YBCO grain boundary junctions,[41] SQUIDs with high spin sensitivity can be fabricated reproducibly. YBCO GBJ SQUIDs have already been demonstrated to operate in $B = 1$ T[4] and were used to measure magnetization curves of microscale magnets in fields up to 0.12 T,[42] however, with poor noise performance. Here, we show that this field scale can be extended to above 1 T, while still maintaining state-of-the art noise performance of the SQUID.

RESULTS AND DISCUSSION

Sample Fabrication and Layout. The YBCO nanoSQUIDs were made in a similar way, as described in Nagel *et al.*[41] Using pulsed laser deposition, epitaxial *c*-axis-oriented YBCO thin films of thickness $d = 50$ nm were grown on $SrTiO_3$ (STO) [001] bicrystal substrates with misorientation angle $\Theta = 24°$. Subsequently, a Au layer of thickness $d_{Au} = 60$ nm was evaporated *in situ*, serving as a shunt resistance for the YBCO GBJs (providing nonhysteretic IVCs at the envisaged operation temperature $T = 4.2$ K and below) and also acting as a protection layer during focused ion beam (FIB) milling. The critical temperature (T_c) of the YBCO film, measured inductively, was $\sim$91 K.

To obtain the nanoSQUID, structures with line widths down to 1 μm (at the region of the grain boundary) were prepatterned by photolithography and Ar ion milling. Subsequently, two nanoscaled Josephson junctions and a constriction next to the SQUID loop, which permits modulation of the SQUID by applying an additional current I_{mod}, were patterned by FIB. Cutting deep into the STO substrate results in sloped junction edges due to redeposition of amorphous YBCO and STO, which should help to prevent oxygen outdiffusion from the YBCO film. With this procedure, we could fabricate high-performance SQUIDs with junction

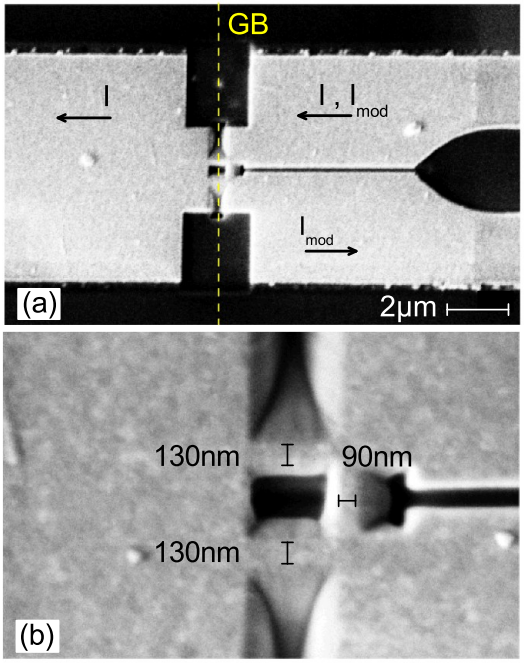

Figure 1. SEM images of the nanoSQUID. In (a), the directions of the modulation and bias currents I_{mod} and I are indicated by arrows, and the grain boundary (GB) is indicated by the vertical dashed line. In (b), the widths of the most narrow sections of the nanoSQUID are indicated.

widths w_J down to ~100 nm. The SQUIDs had almost identical transport and noise characteristics. Below, we discuss data of one device.

Figure 1 shows a scanning electron microscope (SEM) image of the nanoSQUID with a hole size of 300 nm × 400 nm. The junctions have a width $w_J \approx$ 130 nm, and the lengths of the bridges containing the junctions are $l_J \approx 400$ nm. The constriction has a width $w_c \approx 90$ nm and length $l_c = 300$ nm. A bias current I flowing across the junctions, as well as a modulation current I_{mod} flowing across the constriction are applied as indicated by arrows in Figure 1a.

Electric Transport Data. All measurements were performed at $T = 4.2$ K with the magnetic field B carefully aligned in the plane of the SQUID loop. Figure 2a shows the IVC of the nanoSQUID at $B = 0$ and $I_{mod} = 0$. We find a critical current of the SQUID $I_c = 2I_0 = 37\ \mu$A and a resistance $R/2 = 3.5\ \Omega$, which results in $I_0R = 130\ \mu$V (I_0 and R refer to the average junction critical current and resistance, respectively). The corresponding values $j_0 = I_0/(w_J d) = 2.85$ mA/μm^2, $\rho = Rw_J d = 0.046\ \Omega\cdot\mu$m^2, and the value for I_0R are close to the values obtained for earlier devices.[41] Very slightly above I_c, the voltage increases continuously from zero, but then the IVC develops a small hysteresis between 15 and 70 μV. This is presumably caused by some Fiske or LC-type resonance, which prevented accurately fitting the resistive part of this IVC to a resistively and capacitively shunted junction (RCSJ) model.[43,44] Simulations using Langevin equations[45] were still possible for $I_c(I_{mod})$.

Figure 2b shows the measured $I_c(I_{mod})$ at $B = 0$ (solid black line), together with $I_c(I_{mod})$ curves at $B = 1$ and 3 T, which will be discussed below. The data for $B = 0$ are fitted well by the Langevin simulations, which is shown as the dashed cyan line. For the simulations, we have used a noise parameter $\Gamma = 2\pi k_B T/I_0\Phi_0 = 0.01$, corresponding to the measured value of I_0 at $T = 4.2$ K. We further used an inductance asymmetry $\alpha_L = (L_2 - L_1)/(L_1 + L_2) = 0.175$ due to asymmetric biasing of the device; here, L_1 and L_2 are the inductance of the upper and lower arm of the SQUID, respectively (cf. Figure 1). We also used a junction critical current asymmetry $\alpha_i = (I_{02} - I_{01})/(I_{01} + I_{02}) = 0.22$. For the inductance parameter, the simulations yield $\beta_L \equiv 2I_0L/\Phi_0 = 0.65$, which results in $L = 36$ pH. From the $I_c(I_{mod})$ modulation period, we find for the magnetic flux Φ, coupled to the SQUID by I_{mod}, the value $\Phi/I_{mod} = 3.1\ \Phi_0$/mA, which corresponds to a mutual inductance $M_{mod} = 6.4$ pH. We note that the values quoted above for L and M_{mod} are determined experimentally; given the geometry of our device, these values seem to be consistent. However, using standard expressions taking into account the large contribution of the kinetic inductance due to the small YBCO film thickness $d \ll \lambda_L$ (λ_L is the London penetration depth), one expects much smaller values for L and M_{mod}. The reason for this is still unclear. The final parameter to be determined is the Stewart–McCumber parameter $\beta_C \equiv 2\pi I_0R^2C/\Phi_0$, where C is the junction capacitance. Since we cannot fit the experimental IVC accurately, we cannot infer a precise number here. However, due to the fact that a small hysteresis shows up in limited ranges of bias current and applied flux, we assume that β_C is on the order of 1, yielding $C \approx 0.36$ pF. Figure 2c shows the $V(\Phi)$ characteristics of the device for bias currents I ranging from −49.5 to 49.5 μA at $B = 0$. Near $I = I_c$, the curves are hysteretic. The transfer function, that is, the maximum slope of the $V(\Phi)$ curves at optimum I (determined for the nonhysteretic curves), is $V_\Phi = 500\ \mu V/\Phi_0$.

For further measurements, the nanoSQUID was shunted by the input circuit of the SQUID amplifier with an input resistance $R_{inp} = 10\ \Omega$. The additional shunt resistance reduces β_C, yielding nonhysteretic IVCs and $V(I_{mod})$ characteristics; in this case, $V_\Phi \approx 450\ \mu V/\Phi_0$ (at $B = 0$).

At $B = 1$ T (cf. dashed red line in Figure 2b), the $I_c(I_{mod})$ characteristics show a slightly suppressed maximum critical current $I_c(1\ T) = 30\ \mu$A. This pattern is shifted in comparison to the $B = 0$ data, as the SQUID is not perfectly aligned to the magnetic field and flux couples into the Josephson junctions and the SQUID loop. In addition, when sweeping I_{mod} back and forth, a hysteresis becomes visible in a small interval of I_{mod}, presumably caused by Abrikosov vortices trapped in the bias leads. Flux jumps caused by Abrikosov vortices also affect the modulation period, reducing it by about 5% in the interval plotted in Figure 2b. Figure 2d shows

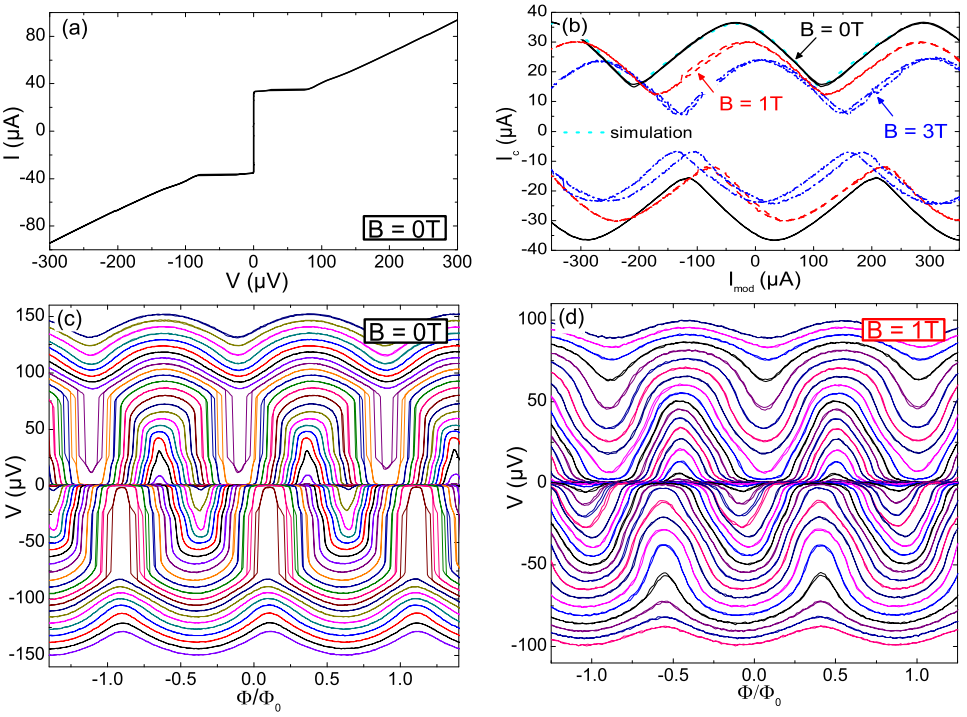

Figure 2. Transport characteristics of the nanoSQUID: (a) IVC at $I_{mod} = 0$ and $B = 0$. (b) Critical current $I_c(I_{mod})$ for $B = 0$, 1, and 3 T; for comparison, the numerically calculated curve for $B = 0$ is also shown. (c) $V(\Phi)$ at $B = 0$ for $I = -49.5 \ldots 49.5$ μA (in 1.5 μA steps.) (d) $V(\Phi)$ at $B = 1$ T for currents fed to the SQUID which is shunted by the input resistance $R_{inp} = 10\ \Omega$ of the SQUID amplifier $I_b = -40.5 \ldots 40.5$ μA (in 1.5 μA steps.) All curves in (a–d) were traced out in both sweep directions.

$V(\Phi)$ characteristics at $B = 1$ T for currents I_b (fed to the SQUID which is shunted by R_{inp}) ranging from -40.5 to 40.5 μA. The IVCs are nonhysteretic and hence the $V(\Phi)$ characteristics are smooth, exhibiting no jumps as in Figure 2c. The lack of hysteresis is either due to the additional shunt resistance R_{inp} or due to the strong magnetic field suppressing the critical current. The transfer function is $V_\Phi = 350\ \mu V/\Phi_0$. Interestingly, the hysteresis in $V(\Phi)$ at $B = 1$ T upon sweeping the applied flux in both directions almost disappeared, which is helpful for reading out the SQUID when operated in strong magnetic fields.

Upon increasing B up to 3 T, still periodic $I_c(I_{mod})$ characteristics with only a slightly suppressed maximum critical current $I_c = 24$ μA could be measured, as shown in Figure 2b as blue dashed-dotted lines. The shift in comparison to the $B = 0$ data did increase further, and also the hysteresis did increase, as mentioned above presumably due to vortices in the bias leads. These data clearly show that the SQUID is operating also in $B = 3$ T. As mentioned above, noise measurements could not be performed for fields much higher than 1 T since the SQUID amplifier trapped magnetic flux. However, this is just a technical problem which can be solved in future measurements by implementing field compensation *via* a coil mounted around the Nb shield.

Flux Noise Measurements. Figure 3 summarizes the flux noise spectra $S_\Phi^{1/2}(f)$ of the nanoSQUID at $B = 0$ and $B = 1$ T at the optimum working point.

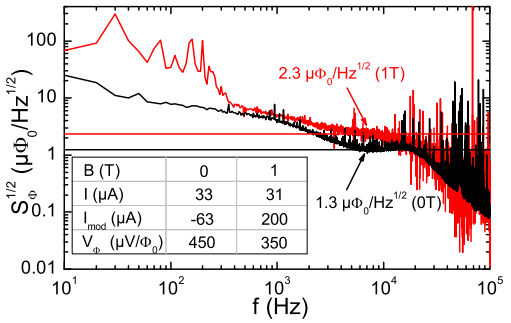

Figure 3. Flux noise spectra of the nanoSQUID at optimum working points at $B = 0$ and 1 T. The horizontal lines indicate the white noise levels.

As measurements were performed without magnetic shielding, noise spikes occur on both spectra. The noise data were corrected for the noise contribution of the amplifier. In both cases, $S_\Phi^{1/2}$ increases for frequencies f below ~3 kHz, a behavior which at least for $B = 0$ is known to arise from critical current fluctuations of the junctions. This contribution can, in principle, be eliminated by proper modulation techniques (bias reversal).[46] At $B = 1$ T, there are presumably additional contributions due to fluctuating Abrikosov vortices. Note, however, that between ~300 Hz and 3 kHz the noise level is less than a factor of 2 higher at $B = 1$ T as compared to $B = 0$. The decrease in $S_\Phi^{1/2}$ above 10 kHz is caused by the limited bandwidth of our measurement setup. At $B = 0$, the white noise level averaged between 6 and 7 kHz is 1.3 $\mu\Phi_0/(\text{Hz})^{1/2}$. For $B = 1$ T, we determine

a rms flux noise of 2.3 $\mu\Phi_0/(\mathrm{Hz})^{1/2}$ averaged between 6 and 7 kHz.

These numbers may be compared to the theoretical expression obtained from Langevin simulations, $S_\Phi = f(\beta_L)\Phi_0 k_B TL/I_0 R$, which is valid for $\beta_C \lesssim 1$.[47] For $\beta_L > 0.4$, $f(\beta_L) \approx 4(1 + \beta_L)$. For lower values of β_L, S_Φ increases. For the parameters of our device, we calculate $S_\Phi^{1/2} = 0.23\ \mu\Phi_0/(\mathrm{Hz})^{1/2}$, that is, a factor of almost 6 less than the experimental value at $B = 0$. Such an excess noise is not unusual for YBCO SQUIDs.[46]

Finally, we note that the observed increase by a factor of ~1.8 in $S_\Phi^{1/2}$ at 6−7 kHz upon increasing B from 0 to 1 T cannot be explained by the reduction of I_0 and V_Φ. From the above-mentioned expression for S_Φ, one would only expect an increase in the white rms flux noise by ~10%. However, we note that in the flux noise data for B = 1 T (cf. Figure 3) no clear white noise is observable. Hence, the quoted value for $S_\Phi^{1/2}(B = 1\ \mathrm{T})$ should be seen as an upper limit for the white noise level.

Spin Sensitivity. In order to estimate the spin sensitivity $S_\mu^{1/2} = S_\Phi^{1/2}/\phi_\mu$ of the nanoSQUID, we numerically calculated the coupling factor $\phi_\mu = \Phi/\mu$, that is, the flux Φ coupled into the SQUID loop by a point-like particle with magnetic moment μ, using the software package 3D-MLSI.[48] Details on the calculation procedure can be found in Nagel *et al.*[41] In brief, one calculates the magnetic field distribution $\vec{B}(\vec{r})$ generated by a current J circulating around the SQUID hole. The coupling factor is obtained from $\phi_\mu = -\hat{e}_\mu \vec{B}(\vec{r})/J$. Here, $\hat{e}_\mu$ is the direction of the magnetic moment $\vec{\mu}$ at position $\vec{r}$. The results of these calculations are summarized in Figure 4 for a point-like particle with magnetic moment pointing in the x-direction. The particle is located in the (x,z) plane (perpendicular to the plane of the SQUID loop in the (x,y) plane) at position $y = 0$ and $x = 0$ to 1000 nm, as indicated by the dashed line in the SEM image shown in Figure 4a. The contour plot in Figure 4b shows $\phi_\mu(x,z)$ for values of $z = 0$ (substrate surface) up to z = 1000 nm. Figure 4c shows a linescan $\phi_\mu(x)$ through this plane, as indicated by the horizontal dashed line in Figure 4b. The linescan is taken at a distance of 10 nm above the Au layer. The coupling factor ϕ_μ has a maximum of 9.2 $n\Phi_0/\mu_B$ at the position of the constriction at $x \approx 0.64\ \mu$m. The minimum in $\phi_\mu(x)$ is slightly left from the center of the SQUID loop; this is because the constriction breaks symmetry. Figure 4d shows a linescan taken along the vertical dashed line in graph (b). The coupling factor ϕ_μ decreases strongly with increasing z. Calculating the spin sensitivity with ϕ_μ = 9.2 $n\Phi_0/\mu_B$, we obtain $S_\mu^{1/2} = 141\ \mu_B/(\mathrm{Hz})^{1/2}$ at $B = 0$ and 250 $\mu_B/(\mathrm{Hz})^{1/2}$ at B = 1 T. In principle, the particle could be brought even closer to the constriction by removing the Au layer right above the constriction, without affecting S_Φ. In this case (for a distance of 10 nm above the YBCO), ϕ_μ = 21 $n\Phi_0/\mu_B$ and $S_\mu^{1/2}$ = 62 $\mu_B/(\mathrm{Hz})^{1/2}$ at $B = 0$ and 110 $\mu_B/(\mathrm{Hz})^{1/2}$ at B = 1 T. The geometrical and electrical parameters for our device are summarized in Table 1.

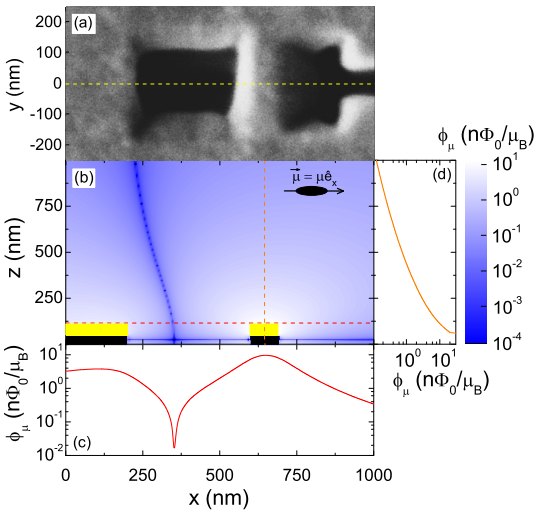

Figure 4. Calculated coupling factor ϕ_μ for the nanoSQUID. (a) SEM image showing SQUID hole and constriction in the (x,y) plane. The dashed line indicates the location of the (x,z) plane for which data are shown in (b); it also indicates the position of the linescan $\phi_\mu(x)$ shown in (c). (b) Contour plot of the coupling factor ϕ_μ *vs* position (x,z) of a magnetic moment pointing in the x-direction. Dashed lines indicate position of the linescans shown in (c) and (d). (c) Horizontal linescan $\phi_\mu(x)$ at a distance of 10 nm above the Au layer. (d) Vertical linescan $\phi_\mu(z)$ at the center of the constriction.

TABLE 1. Summary of Geometric and Electric NanoSQUID Parameters (As Defined in the Text)

d (nm)	l_c (nm)	l_j (nm)	w_c (nm)	w_j (nm)	β_L	L (pH)
50	300	400	90	130	0.65	36

I_0 (μA)	R (Ω)	I_0R (mV)	j_0 (mA/μm^2)	$S_\Phi^{1/2}$ ($n\Phi_0/(\mathrm{Hz})^{1/2}$)	ϕ_μ ($n\Phi_0/\mu_B$)	$S_\mu^{1/2}$ ($\mu_B/(\mathrm{Hz})^{1/2}$)
18.5	7.0	0.13	2.85	1300	21	62

CONCLUSIONS

In summary, we have demonstrated low-noise performance of a YBCO nanoSQUID in magnetic fields up to 1 T. At zero applied field, the white flux noise of the device at 7 kHz was 1.3 $\mu\Phi_0/(\mathrm{Hz})^{1/2}$, increasing only slightly to 2.3 $\mu\Phi_0/(\mathrm{Hz})^{1/2}$ at 1 T. For the spin sensitivity, assuming that a small particle is placed onto a constriction in the SQUID loop, directly on top of the YBCO film, we calculated values of 62 $\mu_B/(\mathrm{Hz})^{1/2}$ at $B = 0$ and 110 $\mu_B/(\mathrm{Hz})^{1/2}$ at B = 1 T.

The device investigated experimentally was not optimized yet in terms of its geometrical and electrical parameters. In particular, the thickness of the epitaxially grown YBCO films can be increased (to ~300 nm). This, in turn, would decrease the SQUID inductance by approximately a factor of 10, which will significantly reduce the flux noise. However, such an increase in thin film thickness will also reduce the coupling factor.

Hence, one has to carefully optimize all SQUID parameters by also taking into account technological constraints. Very recently, we performed such an optimization study, for YBCO nanoSQUIDs operated at 4.2 K and below, which predicts an optimum spin sensitivity of a few $\mu_B/(\mathrm{Hz})^{1/2}$. It remains to be shown whether or not such values can be achieved in high fields.

Furthermore, we note that miniaturized YBCO dc SQUIDs have been already used to investigate the magnetic properties of magnetic microcrystals at 0.12 T between 30 and 70 K.[42] Hence, due to their high T_c, YBCO nanoSQUIDs might also be useful for applications over a wide temperature range up to 70−80 K, such as for the investigation of the transition between the superparamagnetic and ferromagnetic state of magnetic nanoparticles. Optimization of the SQUID parameters for such a large temperature range—and according variation in the critical current of the grain boundary junctions and hence in the noise parameter Γ, the inductance parameter β_L and the Stewart−McCumber parameter β_C—will be more challenging than for operation at a few Kelvin and below. Still, such an approach may be rewarding because highly sensitive YBCO SQUIDs operating at 77 K have been demonstrated in the past.[46]

METHODS

Film Deposition. The films were deposited on 10 mm × 10 mm (1 mm thick) $SrTiO_3$ [001] bicrystal substrates. The substrates contain a single symmetric [001] tilt grain boundary with misorientation angle $\Theta = 24°$. After mounting the substrates by sliver paste on the sample holder, they were transferred to the ultrahigh vacuum (UHV) thin film deposition cluster tool (base pressure 10^{-9} mbar), equipped with a pulsed laser deposition (PLD) chamber and an electron beam evaporation (EBE) chamber. In the PLD chamber, 60 nm thick YBCO films were grown epitaxially by using a pulsed KrF excimer laser (wavelength 248 nm, pulse frequency 2 Hz), which is ablating material from a stochiometric YBCO target (purity 99.995%) with an energy density of ∼2 J/cm^2 of the laser spot on the target. During deposition at an oxygen pressure $p_{O_2} = 0.2$ mbar, the substrate was heated to a temperature T_s = 780 °C by a laser heating system. For the used 60 mm substrate-to-target distance, the PLD parameters yield a deposition rate of 9.8 nm/s. After deposition, the pressure was increased to p_{O_2} = 450 mbar; subsequently, T_s was reduced to 450 °C and kept there for 30 min before cooling the sample to room temperature. For the next deposition step, the sample was transferred in UHV to the EBE chamber, where a 60 nm thick Au film was deposited by electron beam evaporation (deposition rate ∼0.2 nm/s).

FIB Patterning. FIB patterning was performed in a FEI Dualbeam Strata 235, equipped with a Ga ion source. Parameters for FIB milling needed to be chosen carefully, as this patterning step can suppress superconductivity of YBCO. In the cutting scheme, which finally permitted the fabrication of nanoscaled Josephson junctions with no significant reduction of the critical current density j_c, Ga ion currents where adjusted to 30 pA at an acceleration voltage of 30 kV. Four rectangular patterns cut line-by-line (cleaning cross section cut), with cutting directions pointing away from the Josephson junctions, were placed at the grain boundary to form the final SQUID layout.

Measurements of Electric Transport Properties and Noise. The transport and noise measurements were performed at $T = 4.2$ K in an electrically shielded environment. We used a four-terminal configuration with filtered lines to measure IVCs, critical current $I_c(I_{mod})$, and $V(I_{mod})$. For transport measurements, the voltage V across the SQUID was amplified using a room temperature amplifier. All currents were applied by battery-powered current sources. In-plane magnetic fields up to $B = 7$ T could be applied by a split coil superconducting magnet. As magnetic fields that couple into the Josephson junctions suppress their critical current and hence the modulation amplitude of the SQUID, the SQUID loop needed to be aligned with high accuracy parallel to the magnetic field, and the in-plane field was aligned perpendicular to the grain boundary. To do so, the sample was mounted on two goniometers with perpendicular tilt axes (minimum step size 0.02 m°) and a rotator (minimum step size 0.5 m°). Alignment was done by monitoring and maximizing I_c at $B \sim 1$ T.

For noise measurements, the voltage drop across the nanoSQUID was preamplified by a dc SQUID amplifier[49] with 0.l nV/(Hz)$^{1/2}$ resolution and ∼30 kHz bandwidth. In this case, the SQUID was shunted by the input resistance $R_{inp} = 10\ \Omega$ of the SQUID amplifier. The thermal noise of the input resistance (at $T = 4.2$ K) limits the voltage resolution of the SQUID amplifier. To minimize stray fields, the SQUID amplifier was placed inside a Nb shield mounted inside the cryostat at a position of minimum magnetic field. Still, for $B \sim 1.5$ T (at the sample position), the SQUID amplifier trapped magnetic flux, preventing noise measurements at higher fields.

Conflict of Interest: The authors declare no competing financial interest.

Acknowledgment. We gratefully acknowledge S. Menzel for helping us with his expertise and with FIB facilities at IFW Dresden in the early stage of this project. J.N. and T.S acknowledge support by the Carl-Zeiss-Stiftung. This work was funded by the Nachwuchswissenschaftlerprogramm of the Universität Tübingen, by the Deutsche Forschungsgemeinschaft (DFG) *via* the SFB/TRR 21 and by the European Research Council *via* SOCATHES.

REFERENCES AND NOTES

1. Gatteschi, D.; Sessoli, R. Quantum Tunneling of Magnetization and Related Phenomena in Molecular Materials. *Angew. Chem., Int. Ed.* **2003**, *42*, 268–297.
2. Bogani, L.; Vindigni, A.; Sessoli, R.; Gatteschi, D. Single Chain Magnets: Where to from Here? *J. Mater. Chem.* **2008**, *18*, 4750–4758.
3. Fortágh, J.; Zimmermann, C. Toward Atom Chips. *Science* **2005**, *307*, 860–861.
4. Bushev, P.; Bothner, D.; Nagel, J.; Kemmler, M.; Konovalenko, K. B.; Loerincz, A.; Ilin, K.; Siegel, M.; Koelle, D.; Kleiner, R.; *et al.* Trapped Electron Coupled to Superconducting Devices. *Eur. Phys. J. D* **2011**, *63*, 9–16.
5. Rugar, D.; Budakian, R.; Mamin, H. J.; Chui, B. W. Single Spin Detection by Magnetic Resonance Force Microscopy. *Nature* **2004**, *430*, 329–332.
6. Maze, J. R.; Stanwix, P. L.; Hodges, J. S.; Hong, S.; Taylor, J. M.; Cappellaro, P.; Jiang, L.; Gurudev Dutt, M. V.; Togan, E.; Zibrov, A. S.; *et al.* Nanoscale Magnetic Sensing with an Individual Electronic Spin in Diamond. *Nature* **2008**, *455*, 644–647.
7. Balasubramanian, G.; Chan, I. Y.; Kolesov, R.; Al-Hmoud, M.; Tisler, J.; Shin, C.; Kim, C.; Wojcik, A.; Hemmer, P. R.; Krueger, A.; *et al.* Nanoscale Imaging Magnetometry with Diamond Spins under Ambient Conditions. *Nature* **2008**, *455*, 648–651.
8. Manassen, Y.; Hamers, R. J.; Demuth, J. E.; Castellano, A. J., Jr. Direct Observation of the Precession of Individual Paramagnetic Spins on Oxidized Silicon Surfaces. *Phys. Rev. Lett.* **1989**, *62*, 2531–2534.

9. Durkan, C.; Welland, M. E. Electronic Spin Detection in Molecules Using Scanning-Tunneling-Microscopy-Assisted Electron-Spin Resonance. *Appl. Phys. Lett.* **2002**, *80*, 458–460.
10. Theil Kuhn, L.; Geim, A. K.; Lok, J. G. S.; Hedegård, P.; Ylänen, K.; Jensen, J. B.; Johnson, E.; Lindelof, P. E. Magnetisation of Isolated Single Crystalline Fe-Nanoparticles Measured by a Ballistic Hall Micro-Magnetometer. *Eur. Phys. J. D* **2000**, *10*, 259–263.
11. Kazakova, O.; Panchal, V.; Gallop, J.; See, P.; Cox, D. C.; Spasova, M.; Cohen, L. F. Ultrasmall Particle Detection Using a Submircon Hall Sensor. *J. Appl. Phys.* **2010**, *107*, 09E708.
12. Voss, R. F.; Laibowitz, R. B.; Broers, A. N. Niobium Nanobridge dc SQUID. *Appl. Phys. Lett.* **1980**, *37*, 656–658.
13. Wernsdorfer, W. Classical and Quantum Magnetization Reversal Studied in Nanometersized Particles and Clusters. *Adv. Chem. Phys.* **2001**, *118*, 99–190.
14. Lam, S. K. H.; Tilbrook, D. L. Development of a Niobium Nanosuperconducting Quantum Interference Device for the Detection of Small Spin Populations. *Appl. Phys. Lett.* **2003**, *82*, 1078–1080.
15. Cleuziou, J.-P.; Wernsdorfer, W.; Bouchiat, V.; Ondarçuhu, T.; Monthioux, M. Carbon Nanotube Superconducting Quantum Interference Device. *Nat. Nanotechnol.* **2006**, *1*, 53–59.
16. Troeman, A. G. P.; Derking, H.; Borger, B.; Pleikies, J.; Veldhuis, D.; Hilgenkamp, H. NanoSQUIDs Based on Niobium Constrictions. *Nano Lett.* **2007**, *7*, 2152–2156.
17. Huber, M. E.; Koshnick, N. C.; Bluhm, H.; Archuleta, L. J.; Azua, T.; Björnsson, P. G.; Gardner, B. W.; Halloran, S. T.; Lucero, E. A.; Moler, K. A. Gradiometric Micro-SQUID Susceptometer for Scanning Measurements of Mesoscopic Samples. *Rev. Sci. Instrum.* **2008**, *79*, 053704.
18. Granata, C.; Esposito, E.; Vettoliere, A.; Petti, L.; Russo, M. An Integrated Superconductive Magnetic Nanosensor for High-Sensitivity Nanoscale Applications. *Nanotechnology* **2008**, *19*, 275501.
19. Wu, C. H.; Chou, Y. T.; Kuo, W. C.; Chen, J. H.; Wang, L. M.; Chen, J. C.; Chen, K. L.; Sou, U. C.; Yang, H. C.; Jeng, J. T. Fabrication and Characterization of High-T_c $YBa_2Cu_3O_{7-x}$ NanoSQUIDs Made by Focused Ion Beam Milling. *Nanotechnology* **2008**, *19*, 315304.
20. Koshnick, N. C.; Huber, M. E.; Bert, J. A.; Hicks, C. W.; Large, J.; Edwards, H.; Moler, K. A. A Terraced Scanning Superconducting Quantum Interference Device Susceptometer with Submicron Pickup Loops. *Appl. Phys. Lett.* **2008**, *93*, 243101.
21. Foley, C. P.; Hilgenkamp, H. Why NanoSQUIDs Are Important: An Introduction to the Focus Issue. *Supercond. Sci. Technol.* **2009**, *22*, 064001.
22. Vohralik, P. F.; Lam, S. K. H. NanoSQUID Detection of Magnetization from Ferritin Nanoparticles. *Supercond. Sci. Technol.* **2009**, *22*, 064007.
23. Bouchiat, V. Detection of Magnetic Moments Using a Nano-SQUID: Limits of Resolution and Sensitivity in Near-Field SQUID Magnetometry. *Supercond. Sci. Technol.* **2009**, *22*, 064002.
24. Faucher, M.; Jubert, P.-O.; Fruchart, O.; Wernsdorfer, W.; Bouchiat, V. Optimizing the Flux Coupling between a NanoSQUID and a Magnetic Particle Using Atomic Force Microscope Nanolithography. *Supercond. Sci. Technol.* **2009**, *22*, 064010.
25. Finkler, A.; Segev, Y.; Myasoedov, Y.; Rappaport, M. L.; Ne'eman, L.; Vasyukov, D.; Zeldov, E.; Huber, M. E.; Martin, J.; Yacoby, A. Self-Aligned Nanoscale SQUID on a Tip. *Nano Lett.* **2010**, *10*, 1046–1049.
26. Hao, L.; Aßmann, C.; Gallop, J. C.; Cox, D.; Ruede, F.; Kazakova, O.; Josephs-Franks, P.; Drung, D.; Schurig, T. Detection of Single Magnetic Nanobead with a Nano-Superconducting Quantum Interference Device. *Appl. Phys. Lett.* **2011**, *98*, 092504.
27. Lam, S. K. H.; Clem, J. R.; Yang, W. A Nanoscale SQUID Operating at High Magnetic Fields. *Nanotechnology* **2011**, *22*, 455501.
28. Nagel, J.; Kieler, O. F.; Weimann, T.; Wölbing, R.; Kohlmann, J.; Zorin, A. B.; Kleiner, R.; Koelle, D.; Kemmler, M. Superconducting Quantum Interference Devices with Submicron Nb/HfTi/Nb Junctions for Investigation of Small Magnetic Particles. *Appl. Phys. Lett.* **2011**, *99*, 032506.
29. Mandal, S.; Bautze, T.; Williams, O. A.; Naud, C.; Étienne Bustarret,; Omnès, F.; Rodière, P.; Meunier, T.; Bäuerle, C.; Saminadayar, L. The Diamond Superconducting Quantum Interference Device. *ACS Nano* **2011**, *5*, 7144–7148.
30. Russo, R.; Granata, C.; Esposito, E.; Peddis, D.; Cannas, C.; Vettoliere, A. Nanoparticle Magnetization Measurements by a High Sensitive Nano-Superconducting Quantum Interference Device. *Appl. Phys. Lett.* **2012**, *101*, 122601.
31. Van Harlingen, D. J.; Koch, R. H.; Clarke, J. Superconducting Quantum Interference Device with Very Low Magnetic Flux Noise Energy. *Appl. Phys. Lett.* **1982**, *41*, 197–199.
32. Gallop, J. SQUIDs: Some Limits to Measurement. *Supercond. Sci. Technol.* **2003**, *16*, 1575–1582.
33. Kleiner, R.; Koelle, D.; Ludwig, F.; Clarke, J. Superconducting Quantum Interference Devices: State-of-the-Art and Applications. *Proc. IEEE* **2004**, *92*, 1534–1548.
34. Chen, L.; Wernsdorfer, W.; Lampropoulos, C.; Christou, G.; Chiorescu, I. On-Chip SQUID Measurements in the Presence of High Magnetic Fields. *Nanotechnology* **2010**, *21*, 405504.
35. Wernsdorfer, W. From Micro- to Nano-SQUIDs: Applications to Nanomagnetism. *Supercond. Sci. Technol.* **2009**, *22*, 064013.
36. Drung, D.; Mück, M. In *The SQUD Handbook*; Clarke, J., Braginski, A. I., Eds.; Wiley-VCH: Weinheim, Germany, 2004; Vol. 1: Fundamentals and Technology of SQUIDs and SQUID Systems, Chapter 4, pp 127–170.
37. Hao, L.; Macfarlane, J. C.; Gallop, J. C.; Cox, D.; Beyer, J.; Drung, D.; Schurig, T. Measurement and Noise Performance of Nano-Superconducting-Quantum-Interference Devices Fabricated by Focused Ion Beam. *Appl. Phys. Lett.* **2008**, *92*, 192507.
38. Romans, E. J.; Rozhko, S.; Young, L.; Blois, A.; Hao, L.; Cox, D.; Gallop, J. C. Noise Performance of Niobium Nano-SQUIDs in Applied Magnetic Fields. *IEEE Trans. Appl. Supercond.* **2011**, *21*, 404–407.
39. Gross, R.; Alff, L.; Beck, A.; Froehlich, O.; Koelle, D.; Marx, A. Physics and Technology of High Temperature Superconducting Josephson Junctions. *IEEE Trans. Appl. Supercond.* **1997**, *7*, 2929–2935.
40. Hilgenkamp, H.; Mannhart, J. Grain Boundaries in High-T_c Superconductors. *Rev. Mod. Phys.* **2002**, *74*, 485.
41. Nagel, J.; Konovalenko, K. B.; Kemmler, M.; Turad, M.; Werner, R.; Kleisz, E.; Menzel, S.; Klingeler, R.; Büchner, B.; Kleiner, R.; *et al.* Resistively Shunted $YBa_2Cu_3O_7$ Grain Boundary Junctions and Low-Noise SQUIDs Patterned by a Focused Ion Beam down to 80 nm Linewidth. *Supercond. Sci. Technol.* **2011**, *24*, 015015.
42. Takeda, K.; Mori, H.; Yamaguchi, A.; Ishimoto, H.; Nakamura, T.; Kuriki, S.; Hozumi, T.; Ohkoshi, S. High Temperature Superconductor Micro-Superconducting-Quantum-Interference-Device Magnetometer for Magnetization Measurement of a Microscale Magnet. *Rev. Sci. Instrum.* **2008**, *79*, 033909.
43. Stewart, W. C. Current-Voltage Characteristics of Josephson Junctions. *Appl. Phys. Lett.* **1968**, *12*, 277.
44. McCumber, D. Effect of ac Impedance of dc Voltage-Current Characteristics of Josephson Junctions. *J. Appl. Phys.* **1968**, *39*, 3113.
45. Tesche, C. D.; Clarke, J. DC SQUID: Noise and Optimization. *J. Low Temp. Phys.* **1977**, *29*, 301–331.
46. Koelle, D.; Kleiner, R.; Ludwig, F.; Dantsker, E.; Clarke, J. High-Transition-Temperature Superconducting Quantum Interference Devices. *Rev. Mod. Phys.* **1999**, *71*, 631–686.
47. Chesca, B.; Kleiner, R.; Koelle, D. In *The SQUD Handbook*; Clarke, J., Braginski, A. I., Eds.; Wiley-VCH: Weinheim, Germany, 2004; Vol. 1: Fundamentals and Technology of SQUIDs and SQUID Systems, Chapter 2, pp 29–92.
48. Khapaev, M.; Kupriyanov, M.; Goldobin, E.; Siegel, M. Current Distribution Simulation for Superconducting Multi-Layered Structures. *Supercond. Sci. Technol.* **2003**, *16*, 24–27.
49. SQ100 LTS dc SQUID, PC-100 Single-Channel dc SQUID Electronics System, STAR Cryoelectronics, USA.

Publication 2

IOP Publishing Superconductor Science and Technology
Supercond. Sci. Technol. **27** (2014) 125007 (12pp) doi:10.1088/0953-2048/27/12/125007

Optimizing the spin sensitivity of grain boundary junction nanoSQUIDs—towards detection of small spin systems with single-spin resolution

R Wölbing, T Schwarz, B Müller, J Nagel, M Kemmler, R Kleiner and D Koelle

Physikalisches Institut-Experimentalphysik II and Center for Collective Quantum Phenomena in LISA$^+$, Universität Tübingen, Auf der Morgenstelle 14, D-72076 Tübingen, Germany

Received 3 June 2014, revised 22 September 2014
Accepted for publication 24 September 2014
Published 7 November 2014

Abstract

We present an optimization study of the spin sensitivity of nano superconducting quantum interference devices (SQUIDs) based on resistively shunted grain boundary Josephson junctions. In addition the direct current SQUIDs contain a narrow constriction onto which a small magnetic particle can be placed (with its magnetic moment in the plane of the SQUID loop and perpendicular to the grain boundary) for efficient coupling of its stray magnetic field to the SQUID loop. The separation of the location of optimum coupling from the junctions allows for an independent optimization of the coupling factor ϕ_μ and junction properties. We present different methods for calculating ϕ_μ (for a magnetic nanoparticle placed 10 nm above the constriction) as a function of device geometry and show that those yield consistent results. Furthermore, by numerical simulations we obtain a general expression for the dependence of the SQUID inductance on geometrical parameters of our devices, which allows to estimate their impact on the spectral density of flux noise S_Φ of the SQUIDs in the thermal white noise regime. Our analysis of the dependence of S_Φ and ϕ_μ on the geometric parameters of the SQUID layout yields a spin sensitivity $S_\mu^{1/2} = S_\Phi^{1/2}/\phi_\mu$ of a few μ_B Hz$^{-1/2}$ (μ_B is the Bohr magneton) for optimized parameters, respecting technological constraints. However, by comparison with experimentally realized devices we find significantly larger values for the measured white flux noise, as compared to our theoretical predictions. Still, a spin sensitivity on the order of $10\,\mu_B$ Hz$^{-1/2}$ for optimized devices seems to be realistic.

Keywords: Josephson junctions, nanoSQUIDs, spin sensitivity

(Some figures may appear in colour only in the online journal)

1. Introduction

Miniaturized direct current (dc) superconducting quantum interference devices (SQUIDs) with dimensions in the sub-micrometer range (nanoSQUIDs) are promising devices for the sensitive detection and investigation of small spin systems [1]. The basic idea behind this is to attach a small (nanometer-sized) magnetic particle directly to the SQUID and trace out magnetic hysteresis loops of the particle. This shall be done by detecting the change of the stray magnetic field of the particle with magnetic moment $\boldsymbol{\mu}$ via the change of the magnetic flux Φ coupled to the SQUID loop [2–4]. To meet the ultimate goal of detecting the flipping of only a few electron spins [5], the spin sensitivity $S_\mu^{1/2} = S_\Phi^{1/2}/\phi_\mu$ has to be optimized carefully via reducing the spectral density of flux noise S_Φ of the SQUID and increasing the coupling factor $\phi_\mu \equiv \Phi/\mu$ (with $\mu \equiv |\boldsymbol{\mu}|$). S_Φ can be reduced by shrinking the size of the SQUID loop, and hence its inductance L, and ϕ_μ

can be increased by placing the particle on a narrow constriction inserted in the SQUID loop, which motivates the need to implement sub-micron SQUID structures [2, 4, 6–26].

Until now, the most common approach for the realization of nanoSQUIDs is to use constriction type Josephson junctions (cJJs) intersecting small SQUID loops (see e.g. [13] published in a special issue on nanoSQUIDs and related articles therein and [7, 8, 10, 12, 15, 20, 23, 25]). Although impressive results have been achieved very recently for ultra-small SQUIDs based on Pb constrictions [24], the cJJ approach comes with several drawbacks: cJJs often show hysteretic current–voltage characteristics (IVCs). This hampers continuous operation of cJJ-based nanoSQUIDs, which however is required for the investigation of the magnetization dynamics of the sample under investigation. Hence, more advanced readout-schemes are required for operating such devices. Here, a promising approach is the dispersive nanoSQUID magnetometer with ultra-low flux noise down to $\sim 30\ \mathrm{n}\Phi_0\ \mathrm{Hz}^{-1/2}$ achieved with Al variable thickness nanobridges at 30 mK [23]. We should also note here, that very sensitive Nb thin film nanoSQUIDs based on cJJs, resistively shunted with a thin W layer and operated in the voltage state, have been realized [12]. However, in this case, the devices show optimum performance only in a narrow range of temperature T not too far below the transition temperature T_c of Nb, which makes them less interesting for applications. Also, the noise properties of cJJs are not well understood and hence hard to optimize. And, finally, the magnetic particles have to be placed close to the cJJs to achieve optimum coupling. However, this means that the junction properties and the coupling factor ϕ_μ cannot be optimized independently, which hampers a careful optimization of the spin sensitivity.

With respect to the application of nanoSQUIDs for the detection of the magnetization reversal of nanomagnets, the most interesting regime of operation is at $T \approx 1$ K and below and at very high magnetic fields in the tesla range [1]. It has been demonstrated that Nb thin film nanoSQUIDs based on constriction type junctions can be operated in impressive background fields up to 7 T [27]. However, the upper critical field B_{c2} of typical Nb thin films ($\sim$1 T) requires to use very thin Nb films with thicknesses of only a few nm, i.e. well below the London penetration depth λ_L of the Nb films, if such SQUIDs shall be operated in tesla fields. This leads to a large kinetic inductance contribution to the SQUID inductance, and hence a large flux noise of such SQUIDs, which does not allow to use the huge potential for the realization of ultralow-noise nanoSQUIDs. We note that ultralow noise values have been achieved for ultra-small SQUIDs based on Pb cJJs up to $\sim$1 T, where the high-field operation was presumably also limited by B_{c2} [24].

To circumvent the above mentioned drawbacks, we recently started to develop dc nanoSQUIDs based on c-axis oriented $YBa_2Cu_3O_7$ (YBCO) thin films with submicron wide bicrystal grain boundary Josephson junctions (GBJs) [28]. Due to the huge upper critical field of YBCO, such SQUIDs can be realized with film thicknesses on the order of λ_L and above and operated in tesla fields. Furthermore, due to the large critical current densities of the YBCO GBJs (several $\mathrm{mA}\,\mu\mathrm{m}^{-2}$ at $T = 4.2$ K and below for a grain boundary misorientation angle of 24°) submicron junctions still yield reasonably large values of the critical current I_0. To achieve non-hysteretic IVCs, the GBJs are shunted by a thin Au film. Due to the fact that the barrier of the GBJs is oriented perpendicular to the YBCO thin film plane, it is possible to apply tesla magnetic fields in the plane of the film, without a significant reduction of I_0 [29]. And finally, by implementing an additional narrow constriction (which can be much narrower than the GBJs) in the SQUID loop, the optimization of the coupling factor for a nanoparticle placed on top of the constriction is possible without affecting the junction properties.

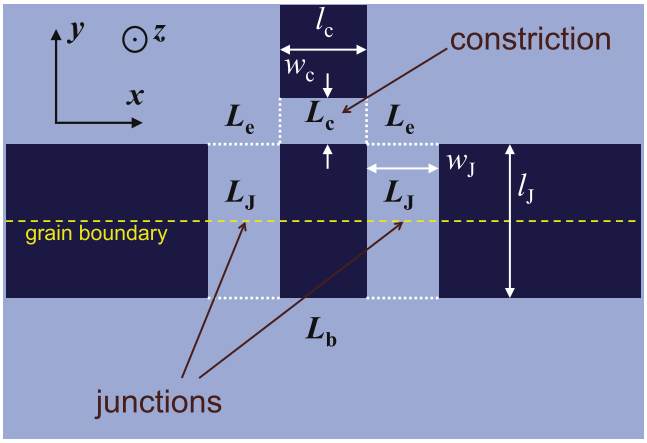

Figure 1. Schematic view of the nanoSQUID layout, divided (by white dotted lines) into the constriction (inductance L_c, length l_c, width w_c), two corners (each with inductance L_e), the two junctions (each with inductance L_J, length l_J, width w_J) and the bottom part (inductance L_b).

Here, we present a detailed optimization study of the spin sensitivity of such grain boundary junction nanoSQUIDs by analyzing the dependence of the flux noise S_Φ and the coupling factor ϕ_μ on the geometry of our devices. We find that for an optimized SQUID geometry a continuous detection of magnetic moments down to a spin sensitivity $S_\mu^{1/2}$ of a few $\mu_B\ \mathrm{Hz}^{-1/2}$ (μ_B is the Bohr magneton) is feasible if a magnetic particle is placed 10 nm above the center of the constriction, with its magnetic moment oriented in the plane of the SQUID loop and perpendicular to the grain boundary.

2. nanoSQUID design

The layout of the nanoSQUID (top view) is shown in figure 1. The SQUID structure is patterned in a YBCO thin film of thickness d, covered by a thin Au film with thickness d_{Au}. The two bridges straddling the grain boundary have a width w_J and length l_J. The upper part of the SQUID loop contains a constriction of width w_c and length l_c. An applied bias current I_b is flowing from top to bottom across the two GBJs. A small magnetic particle can be placed on top of the constriction, and an in-plane magnetic field (perpendicular to the grain

boundary, i.e. along the y-direction) can be applied without significant suppression of the critical current I_0 of the two GBJs.

Optimizing the SQUID for spin sensitivity means to minimize the ratio S_Φ/ϕ_μ^2. The coupling factor ϕ_μ is essentially determined by the geometry of the constriction, i.e., its width w_c and thickness d. S_Φ depends on the SQUID inductance L and on the junction parameters I_0, resistance R and capacitance C. If the constriction could be made not only arbitrarily thin and narrow, but also arbitrarily short, one could envision a scenario, where ϕ_μ reaches a value around $0.5\ \Phi_0/\mu_B$ [4], while, at the same time, the inductance of the constriction remains small (Φ_0 is the magnetic flux quantum). Then, S_Φ could be optimized independently by proper choice of the SQUID size and the junction properties. For the type of device we discuss here, this is certainly not the case and we thus look for an optimization, which is compatible with technological limitations. A large coupling ϕ_μ demands an as narrow and thin as possible constriction. On the other hand, for a too narrow constriction, given a fixed value of d, its inductance L_c and thus also the total inductance L of the SQUID may become too large, possibly degrading the flux noise. This may be counterbalanced by choosing a different film thickness and changing, e.g., the junction width w_J.

In the following sections, we derive explicit expressions for the dependence of ϕ_μ (section 3) and S_Φ (section 4) on various geometric and electric SQUID parameters, which then allows us to optimize S_μ (section 5).

3. Coupling factor

We numerically calculate the coupling factor $\phi_\mu = \Phi/\mu$, i.e. the flux Φ coupled into the SQUID loop by a point-like particle with magnetic moment μ, using the software package 3D-MLSI. This routine takes explicitly into account the geometry in the plane of the SQUID loop (see figure 1), and is based on the numerical simulation of the two-dimensional (2D) sheet current density distribution $j_{2D}(x, y)$ in the SQUID loop, using London theory with λ_L and d (and hence the effective penetration depth in the thin film limit) as adjustable parameters [30].

3.1. Methods

Three different methods, which are briefly described in the following, have been developed to calculate ϕ_μ.

Method 1. With 3D-MLSI we choose an arbitrary value for the total current J circulating around the SQUID hole and calculate the corresponding sheet current density distribution $j_{2D}(x, y)$ in the SQUID loop. The resulting $j_{2D}(x, y)$ is then used to calculate the three-dimensional (3D) magnetic field distribution $\boldsymbol{B}(\boldsymbol{r})$ generated by J. The coupling factor is then obtained from the relation

$$\phi_\mu(\boldsymbol{r}, \hat{\boldsymbol{e}}_\mu) = -\hat{\boldsymbol{e}}_\mu \cdot \boldsymbol{B}(\boldsymbol{r})/J \qquad (1)$$

which was derived in [28]. Here, $\hat{\boldsymbol{e}}_\mu$ is the unit vector along the direction of the magnetic moment $\boldsymbol{\mu} = \mu\,\hat{\boldsymbol{e}}_\mu$ at position $\boldsymbol{r}$. This means that equation (1) provides ϕ_μ for any given position $\boldsymbol{r}$ and orientation $\hat{\boldsymbol{e}}_\mu$ of a point-like magnetic particle.

To capture variations of $\boldsymbol{B}$ with film thickness d, we simply assume that the circulating current J flows within a number n of 2D sheets in the x–y-plane, stacked equidistantly along the z-axis from the upper surface (at $z = 0$) to the lower surface (at $z = -d$) of the SQUID loop. The resulting field $\boldsymbol{B}(\boldsymbol{r})$ is obtained by averaging the individual fields generated by the sheets.

In our earlier work (see [31] and references therein) we used $n = 2$, which corresponds to a circulating current flow only in the upper and lower surface sheet of the SQUID loop. This approach works well if d is small enough. However, if one is interested in the scaling of ϕ_μ with d one should use a larger value for n, which provides a better approximation of a homogeneous current density distribution within the entire film thickness in z-direction, in particular for relatively large d. Since for YBCO $\lambda_L \approx 0.7\ \mu$m along the c-axis (here, the z-direction), we expect such a homogenous current distribution along $\hat{\boldsymbol{e}}_z$ for a technologically reasonable thickness ($d \lesssim 0.5\ \mu$m).

Method 2. The expression for the coupling factor ϕ_μ from equation (1), as used for method 1 does not take into account modifications of $j_{2D}(x, y)$ due to the strongly inhomogeneous dipole field in close vicinity to the magnetic particle. Such a modification, however, may become important when the distance between the point-like dipole and the SQUID surface is smaller than the film thickness d. Within method 2, we achieve a better description of the near-field regime by calculating (with 3D-MLSI) the fluxoid $\Phi_{\text{fluxoid}}(\boldsymbol{r})$ in the SQUID loop, which is induced by a 'quasi-dipole' (mimicking a small magnetic particle at position $\boldsymbol{r}$) with a magnetic moment of $1\ \mu_B$. With this we obtain $\phi_\mu(\boldsymbol{r}) = \Phi_{\text{fluxoid}}(\boldsymbol{r})/\mu_B$. Such a quasi-dipole can be constructed by a properly adjusted circulating current in a tiny loop placed at position $\boldsymbol{r}$. However, in this case, the orientation $\hat{\boldsymbol{e}}_\mu$ of the magnetic moment of the quasi-dipole is now fixed by the design of this tiny loop, implemented in 3D-MLSI, which allows only to construct 2D structures in the x–y-plane.

For instance a quasi-dipole with its magnetic moment oriented along the z-axis (i.e. $\hat{\boldsymbol{e}}_\mu = \hat{\boldsymbol{e}}_z$) can be realized by a current circulating in a tiny ring in the x–y-plane. Due to the layout of the nanoSQUID considered in this work, it is however more favorable to construct a dipole with magnetic moment pointing in y-direction. Unfortunately, it is not possible to build a corresponding ring within 3D-MLSI. Instead, we consider two strips (2D current sheets) lying on top of each other with separation $\Delta z = 3$ nm along the z-axis. Both strips expand 4 nm and 2 nm in x- and y-direction, respectively. Currents flowing along $\hat{\boldsymbol{e}}_x$ ($-\hat{\boldsymbol{e}}_x$) in the upper (lower) strip create a quasi-dipole field with a magnetic moment oriented along $\hat{\boldsymbol{e}}_y$. The currents were adjusted to generate the magnetic field distribution of a single μ_B. Furthermore the two strips are regarded as normal conductors by setting $\lambda_L \to \infty$. The quasi-dipole does not provide the field distribution of an ideal dipole (from a point-like particle) since

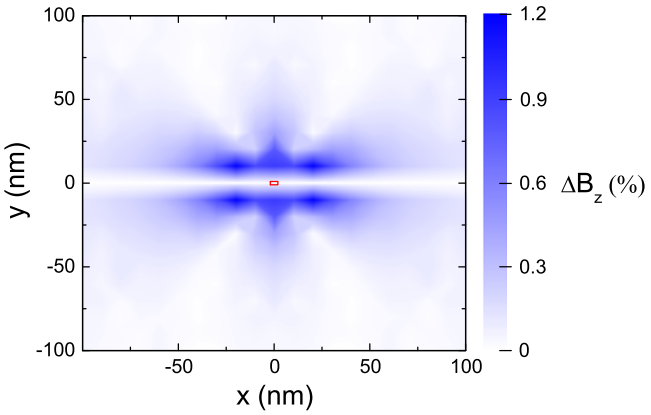

Figure 2. Distribution of normalized difference $\Delta B_z(x, y)$ in the z-components of the quasi-dipole vs ideal dipole fields at $z = 0$, with both dipoles centered at $(0, 0, z_0 = 10\,\text{nm})$. The small rectangle in the center indicates size and position of the two strips (stacked on top of each other) forming the quasi-dipole.

the two strips are not connected. However, the field generated by the missing links should be of minor relevance since it neither interacts with the superconducting structure nor with the SQUID hole. In figure 2 we plot the relative deviation ΔB_z between the z-component of the magnetic field $B_{z,\text{qd}}$ created by the quasi-dipole and $B_{z,\text{d}}$ of an ideal dipole

$$\Delta B_z = \left| \frac{B_{z,\text{qd}} - B_{z,\text{d}}}{B_{z,\text{d}}} \right| \tag{2}$$

in the x–y-plane at $z = 0$, with both dipoles centered at $\boldsymbol{r}_0 = (0, 0, z_0 = 10\,\text{nm})$ and with an orientation of their magnetic moment along the y-axis. As expected, the quasi-dipole is a very good approximation to an ideal magnetic dipole in the far field regime. In the near field regime one finds minor deviations of $\Delta B_{z,\text{max}} \approx 1.2\%$, which presumably arise from the finite volume of the quasi-dipole.

For the nanoSQUID structure, the effect of (ideal) flux focussing is taken into consideration by setting the net current J circulating around the hole to zero. The calculation is deployed for $n = 11$ current sheets and the resulting fluxoids are averaged in a similar way as for method 1.

Method 3. For this method we again examine the interaction of the quasi-dipole with the SQUID loop. In contrast to method 2, (ideal) screening is taken into consideration by setting the fluxoid in the loop to zero. In other words, a circulating current J is induced in the loop, which counterbalances the coupled flux of the quasi-dipole, due to the diamagnetic response of the SQUID. The coupling factor is obtained by computing L of the bare SQUID within 3D-MLSI and calculating $\phi_\mu(\boldsymbol{r}) = \Phi_{\text{fluxoid}}(\boldsymbol{r})/\mu_\text{B} = LJ/\mu_\text{B}$. As before, the calculation is performed for $n = 11$ current sheets. We note that method 3 is very similar to the method used by Koch *et al* [32] for the calculation of the coupling between an electron magnetic moment and a SQUID.

3.2. Comparison of methods

To compare the three methods, we calculate ϕ_μ for a particle with its magnetic moment oriented along $\hat{e}_y$, which corresponds to the optimum direction of the applied external magnetic field for our SQUID design. In all cases, we find a maximum in $\phi_\mu(\boldsymbol{r})$ if the dipole is placed as close as possible on top of the constriction at its center in the x–y-plane. For the following considerations, we set the origin of our coordinate system at the center of the constriction in the x–y-plane at the upper surface of the superconducting film.

Assuming that the particle is placed at the position $\boldsymbol{r}_0 = (0, 0, z_0)$ with $z_0 = 10\,\text{nm}$ above the constriction (without an Au layer, which can be removed without affecting the junction properties), we calculate $\phi_\mu(d)$ in the range $10\,\text{nm} \leqslant d \leqslant 500\,\text{nm}$ for the three presented methods (see figure 3(a)).

For method 1, with $n = 2$ current sheets, $\phi_\mu(d)$ saturates for $d \gtrsim 200\,\text{nm}$ to $\phi_{\mu,\text{s}} \approx \frac{1}{2}\phi_\mu(d = 10\,\text{nm})$. Since the current J is circulating in sheets at the lower $(z = -d)$ and upper $(z = 0)$ surface of the superconductor, the field $B_y(z_0 = 10\,\text{nm})$ induced by the lower sheet decays as d increases. However, the field induced by the upper sheet remains constant and thus the mean value of B_y as well, as soon as the contribution from the lower sheet becomes negligible for large enough d. Obviously, the saturation in $\phi_\mu(d)$ is an artefact stemming from the simple approximation of the current distribution along $\hat{\boldsymbol{e}}_z$ by the currents in only two surface sheets.

Turning to method 1 with $n = 11$ current sheets, the unphysical saturation of $\phi_\mu(d)$ is eliminated. Similar calculations with $n = 101$ and $n = 1001$ reveal the same behavior of $\phi_\mu(d)$ for the range of thickness shown. As expected, method 1 with $n = 2$ and $n = 11$ yields the same $\phi_\mu(d)$ for very small d.

Albeit method 1 provides a sensible approximation of ϕ_μ for currents flowing across the entire film thickness if n is large enough, it does not incorporate the effect of local screening currents induced by a magnetic particle in close proximity to the SQUID. This becomes obvious by comparison of the current distributions in the region of the constriction, as shown for method 1 in figure 3(b) and for methods 2 and 3 in figures 3(c) and 3(d), respectively. The latter two feature a more complex current distribution, arising from local screening currents. The corresponding dependence $\phi_\mu(d)$ for method 2 and 3 (see figure 3(a)), however, show qualitatively and quantitatively the same behavior as for method 1 (with $n = 11$). Accordingly, the local screening currents taken into account in method 2 and 3 do not alter ϕ_μ in the near field regime as compared to method 1.

Concluding this section, we have shown that all three methods constitute a valid approach for calculating the coupling factor, since each technique gives the same dependence $\phi_\mu(d, w_\text{c})$ for large enough values of n. Furthermore, we note that these methods can also be applied to calculations of ϕ_μ for other nanoSQUID designs, including constriction-type or planar sandwich-type junctions, which would facilitate optimization of their spin sensitivity and comparison of different designs.

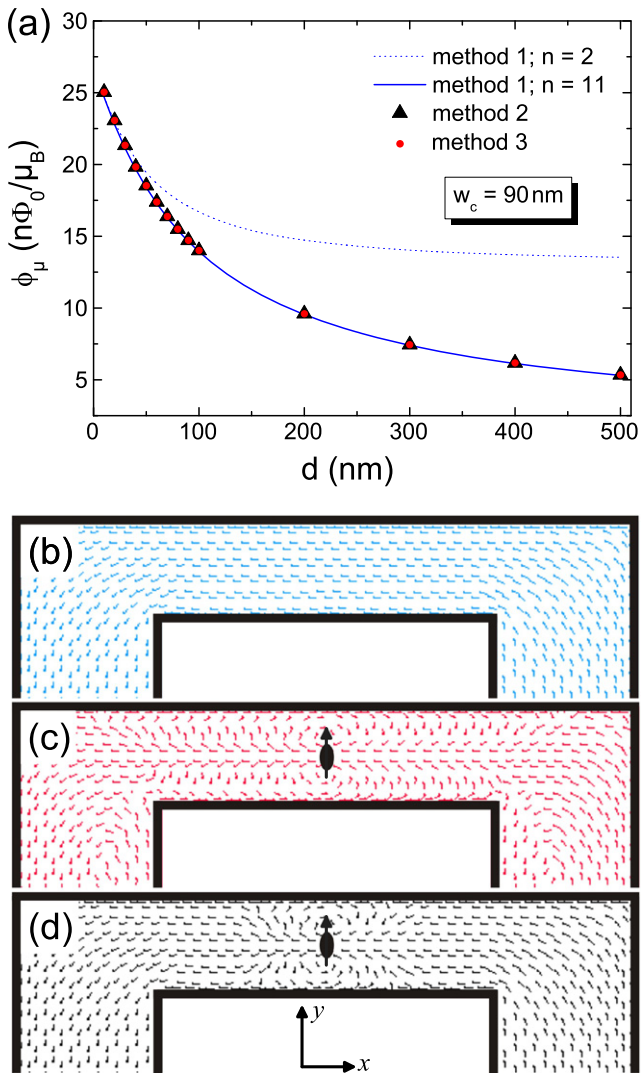

Figure 3. Comparison of methods used for calculating the coupling factor and current distribution in a $w_c = 90$ nm wide constriction (for $\lambda_L = 250$ nm). (a) $\phi_\mu(d)$ for a particle at $z_0 = 10$ nm; position and direction of magnetic moment is indicated in (c) and (d). (b)–(d) 3D-MLSI output of the current distribution in the x–y-plane calculated with (b) method 1 (identical distribution for all n sheets), (c) method 2 and (d) method 3 (for uppermost sheet at $z = 0$). Arrows indicate the local direction of currents.

3.3. Results

As already mentioned in section 2, the coupling factor should also depend on the width of the constriction. Hence, we computed ϕ_μ in the range 10 nm $\leqslant w_c \leqslant$ 500 nm and 10 nm $\leqslant d \leqslant$ 500 nm, assuming that the quasi-dipole is placed 10 nm above the center of the constriction, as in the previous section. The numerical results can be approximated by

$$\phi_\mu(d, w_c) \approx \frac{\phi_{\mu,0}}{\left(1 + \frac{d}{d_0}\right)\left(1 + \frac{w_c}{w_0}\right)}, \tag{3}$$

with the values for the fitting parameters $\phi_{\mu,0}$, d_0 and w_0 given in table 1 for two different values of λ_L. As expected, ϕ_μ decreases with increasing width w_c and thickness d. Within the simulation range, we find a monotonic decrease of $\phi_\mu(d, w_c)$, with a slightly weaker decay in $\phi_\mu(d)$ as for $\phi_\mu(w_c)$.

By modifying the distance z_0 between the magnetic particle and the upper surface of the superconductor, we find qualitatively the same dependence as in equation (3) within 10 nm $\leqslant z_0 \leqslant$ 1000 nm with absolute values scaling like $\phi_\mu(z_0) \propto z_0^{-3/2}$. Since the optimization of ϕ_μ does only trivially depend on the distance between particle and SQUID, we can absorb $\phi_\mu(z_0)$ into $\phi_{\mu,0}$.

4. Flux noise

To determine the flux noise of the SQUID in the thermal white noise regime, we use the theoretical expression obtained from Langevin simulations

$$S_\Phi = f(\beta_L)\Phi_0 k_B T L / I_0 R, \tag{4}$$

which is valid for a Stewart–McCumber parameter $\beta_C \equiv 2\pi I_0 R^2 C/\Phi_0 \lesssim 1$ and $\Gamma\beta_L < 0.1$ [33]. Here, $\Gamma \equiv 2\pi k_B T/I_0\Phi_0$ is the noise parameter, and $\beta_L \equiv 2LI_0/\Phi_0$ is the screening parameter. For $\beta_L > 0.4$, $f(\beta_L) \approx 4(1 + \beta_L)$. For lower values of β_L, S_Φ increases.

The first factor to be discussed is I_0R. The junction resistance R can be varied to some extent by varying the thickness d_{Au} of the Au layer covering the YBCO film; the maximum achievable value is the unshunted junction normal state resistance R_N (for $d_{Au} = 0$). For 24° YBCO grain boundary junctions, I_0R_N values ~2 − 3 mV are achievable at 4.2 K [34]. However, such junctions typically have hysteretic IVCs. We thus demand $\beta_C \lesssim 1$ to avoid hysteresis. Ideally, one would like to derive an expression for I_0R as a function of w_J, d and d_{Au} using the constraint $\beta_C \lesssim 1$ and assuming certain values for the critical current density j_0, unshunted normal junction resistance times area $\rho \equiv R_N w_J d$ and capacitance per junction area C'. However, the scaling of R with w_J, d and d_{Au} is currently not known. Furthermore, an estimate of C' as a function of w_J and d, based on various scaling laws available in literature [35–37] is quite difficult, in particular since it is difficult to determine C for underdamped YBCO GBJs and since the stray capacitance due to the commonly used $SrTiO_3$ substrates may play an important role [38]. On the other hand, we have fabricated nanoSQUIDs from 24° YBCO GBJs with different junction widths 85 $\leqslant w_J \leqslant$ 440 nm and film thicknesses 50, 100, 120 and 300 nm, using the focused ion beam (FIB) milling technique as described in [29]. Parameters of some of those devices are listed in table 2. Except for the devices with both, small film thickness ($d = 50$ nm) and narrow junctions ($w_J \approx 100$ nm), which tend to have slightly lower I_0R and j_0, typical values for our devices are $I_0R \approx 0.5$ mV and $j_0 = 3 - 5$ mA μm^{-2} at $T = 4.2$ K. Below we will find an optimum junction width well above 100 nm and a very weak dependence of the optimum spin sensitivity on film thickness for

Table 1. Summary of fit parameters from numerical simulations on nanoSQUIDs for two different values of λ_L. The values for $S_{\Phi,0}^{1/2}$ and $S_{\mu,0}^{1/2}$ are given for $T = 4.2$ K and $I_0R = 0.5$ mV.

λ_L (nm)	$\phi_{\mu,0}$ ($n\Phi_0/\mu_B$)	d_0 (nm)	w_0 (nm)	w_c' (nm)	L' (pH·nm)	L_e' (pH·nm)	L_b' (pH·nm)	L_b'' (pH·nm)	b	r	L'/d_0 (pH)	$S_{\Phi,0}^{1/2}$ ($n\Phi_0$ $Hz^{-1/2}$)	$S_{\mu,0}^{1/2}$ (μ_B $Hz^{-1/2}$)
250	49	120	102	7	85	56	25	120	0.29	2.73	0.71	12.6	0.26
335	78	83	53	4.8	143	100	45	150	0.31	2.45	1.72	19.7	0.25

100 nm $\lesssim d \lesssim$ 500 nm. Thus, rather than introducing an ill-defined scaling of I_0R with w_J and d, below we fix $I_0R = 0.5$ mV and $j_0 = 3$ mAμm^{-2} as realistic values.

We next determine the dependence of the SQUID inductance L on the various geometrical parameters. We separate the SQUID into the constriction (inductance L_c, length l_c, width w_c), the two (symmetric) bridges containing the junctions (inductance L_J, length l_J, width w_J), the two corners connecting the constriction and the junction arms (inductance L_e), and the bottom part of the SQUID (inductance L_b), as indicated in figure 1. Then, L is given by

$$L = L_c + 2L_J + 2L_e + L_b. \tag{5}$$

We should find $L_c(w_c, l_c, d)$, $L_J(w_J, l_J, d)$, $L_e(w_c, w_J, d)$ and $L_b(l_c, w_J, d)$. From 3D-MLSI simulations we find the parametrization $L_c(w_c, l_c, d) \approx L' \cdot l_c/w_c d$. This expression fits the computed L_c well, within the parameter range 10 nm $\leqslant l_c, w_c, d \leqslant$ 500 nm, covered by the simulations. We use the same parametrization for $L_J(w_J, l_J, d)$. For the corners we find, within a 15% variation with respect to w_J and w_c, the expression $L_e \approx L_e'/d$. Finally, we find $L_b \approx L_b' l_c/w_J d + L_b''/d$. The fitting parameters L', L_e', L_b' and L_b'' are summarized in table 1 for two different values of λ_L. Inserting these expressions into equation (5) yields

$$L \approx \frac{L'}{d}\left\{\frac{l_c}{w_c} + \frac{2l_J + bl_c}{w_J} + r\right\}, \tag{6}$$

with $b \equiv L_b'/L'$ and $r \equiv (2L_e' + L_b'')/L'$ (see table 1). We note that in our simulations we have adjusted $\lambda_L = 250$ nm to be consistent with most of the experimentally determined values of L for our nanoSQUIDs. This value is consistent with the literature on λ_L in the a–b-plane of epitaxially grown c-axis oriented YBCO thin films [25, 39]. However, for some devices we find good agreement between measured and simulated values of L only if we assume larger values for λ_L, e.g. $\lambda_L = 335$ nm for 'exp. device 1a'[1] listed in table 2.

For the minimization of S_μ, we will use β_L as a variable parameter. Since both, L and w_J are not independent of each other and are related to β_L, we express both as functions of β_L. This will allow us to eliminate L and w_J in the final expression for S_μ which has to be optimized. With $\beta_L = 2I_0L/\Phi_0$ and $I_0 = j_0 w_J d$, we obtain

$$w_J(\beta_L, L) = \frac{\Phi_0\beta_L}{2j_0 dL}. \tag{7}$$

[1] 'Exp. device 1a' corresponds to the YBCO nanoSQUID which has been described in [29]. Due to our refined calculation of the coupling factor ϕ_μ (i.e. using $n = 11$ instead of $n = 2$ current sheets), we find a ~14 % reduction of the calculated value for ϕ_μ, and correspondingly a slightly larger value for $S_\mu^{1/2}$, as compared to the values quoted in [29]. Our choice of $\lambda_L = 250$ nm for the calculation of ϕ_μ (instead of 335 nm in [29]) has a negligible effect on the calculated value of ϕ_μ for this device.

Inserting this into equation (6) yields

$$L(\beta_L) \approx \frac{L'}{d}\left(\frac{l_c}{w_c} + r\right)\left\{1 - \frac{\kappa}{\beta_L}\right\}^{-1}, \tag{8}$$

with

$$\kappa(l_J, l_c, j_0) \equiv 2(2l_J + bl_c)j_0 L'/\Phi_0. \tag{9}$$

Inserting equation (8) into equation (4) and using $f(\beta_L) = 4(1 + \beta_L)$ finally yields

$$S_\Phi(d, w_c, \beta_L) \approx S_{\Phi,0}\frac{d_0}{d}\left(\frac{l_c}{w_c} + r\right)\frac{1 + \beta_L}{1 - \frac{\kappa}{\beta_L}}, \tag{10}$$

with $S_{\Phi,0}^{1/2} \equiv 2\sqrt{\frac{\Phi_0 k_B T L'}{I_0 R d_0}}$ (see table 1). The most important result here is the scaling $S_\Phi \propto 1/d$. This is due to the fact that the SQUID inductance $L \propto 1/d$ within the simulation range for d, because of the increase of the kinetic inductance contribution with decreasing d below λ_L. For $d \gtrsim 2\lambda_L$ we expect a saturation of $L(d)$ and hence of $S_\Phi(d)$. However, we will neglect this for the optimization of S_μ, since values for $d \gtrsim$ 500 nm are outside the simulation range and since we cannot expect to produce high-quality GBJs for such large values of d.

5. Optimization of spin sensitivity via improved SQUID geometry

With equation (3) and (10) we find the spin sensitivity $S_\mu^{1/2} = S_\Phi^{1/2}/\phi_\mu$. The individual dependencies on d, β_L and constriction parameters w_c and l_c can be separated. Hence, we can express the spin sensitivity as

$$S_\mu^{1/2}(d, w_c, \beta_L) = S_{\mu,0}^{1/2} \cdot s_d(d) \cdot s_{\beta_L}(\beta_L) \cdot s_c(w_c, l_c), \tag{11}$$

with $S_{\mu,0}^{1/2} \equiv S_{\Phi,0}^{1/2}/\phi_{\mu,0}$ (see table 1) and with

$$s_d(d) \equiv \sqrt{\frac{d_0}{d}} + \sqrt{\frac{d}{d_0}}, \tag{12}$$

$$s_{\beta_L}(\beta_L) \equiv \sqrt{\frac{1 + \beta_L}{1 - \frac{\kappa}{\beta_L}}}, \tag{13}$$

$$s_c(w_c, l_c) \equiv \left(1 + \frac{w_c}{w_0}\right)\sqrt{\frac{l_c}{w_c} + r}. \tag{14}$$

Figure 4 shows $s_d(d)$, $s_{\beta_L}(\beta_L)$ for fixed κ, and $s_c(w_c)$ and $s_c(l_c)$ for fixed l_c and w_c, respectively, for $\lambda_L = 250$ nm. In the following we discuss the optimum choice of the various parameters.

For $s_d(d)$ from equation (12) we obtain a shallow minimum at $d_{min} = d_0$, and a rather weak dependence for $d \gtrsim$ 100 nm. This indicates that with increasing d above ~100 nm the decrease in kinetic inductance (and hence in flux noise) and coupling factor almost compensate each other within the simulation range. Hence, the optimization of the spin sensitivity with respect to film thickness is

Table 2. Summary of geometric and electric nanoSQUID parameters (as defined in the text). The values for 'opt. device 1' are calculated for optimized parameters obtained for a given constriction length l_c, with $\lambda_L = 250$ nm. For 'opt. device 2' we used more relaxed values for w_c, l_c and l_J and otherwise identical input parameters for d, j_0, I_0R, λ_L with correspondingly optimized β_L and adjusted w_J. For the experimental devices we quote experimentally determined values for L and $S_\Phi^{1/2}$ (in the thermal white noise limit) [40] together with values (in brackets) which are calculated with equation (6) and (4), respectively, with $\lambda_L = 250$ nm. Here, the flux noise was calculated based on the measured SQUID inductance L. Accordingly, the values in brackets for the spin sensitivity $S_\mu^{1/2}$ are based on the calculated values for the flux noise $S_\Phi^{1/2}$.

	d	l_c	l_J	w_c	w_J	β_L	L	I_0	R	I_0R	j_0	L_c	L_J	L_e	L_b	$S_\Phi^{1/2}$	ϕ_μ	$S_\mu^{1/2}$
Units	nm	nm	nm	nm	nm		pH	μA	Ω	mV	mA μm^{-2}	pH	pH	pH	pH	nΦ_0 Hz$^{-1/2}$	nΦ_0/μ_B	μ_B Hz$^{-1/2}$
opt. device1	120	44	174	25	280	0.40	4.1	101	5.0	0.5	3	1.3	0.44	0.47	1.0	36	20	1.8
opt. device2	120	100	200	60	316	0.45	4.1	114	4.4	0.5	3	1.2	0.45	0.47	1.1	36	15	2.4
exp. device1a	50	300	400	90	130	0.65	36 (22)	18.5	7.0	0.13	2.85	5.7	5.2	1.1	3.6	1300 (228)	18	71 (12)
exp. device1b	50	535	435	50	85	1.29	42 (43)	31.4	10.2	0.32	7.39	18	8.7	1.1	5.6	600 (185)	23	26 (8.0)
exp. device2a	100	500	500	420	190	0.78	8.9 (8.5)	91	5.4	0.49	4.79	1.0	2.2	0.56	1.9	450 (60)	5.2	86 (11)
exp. device2b	100	475	455	410	140	1.37	9.1 (9.7)	155	3.1	0.47	11.0	0.98	2.8	0.56	2.0	400 (72)	5.3	75 (13)
exp. device3	120	230	370	100	205	0.94	5.8 (6.4)	168	5.0	0.84	6.81	1.6	1.3	0.47	1.2	<83 (39)	12	<6.7 (3.1)
exp. device4a	300	300	450	120	280	0.87	2.9 (2.5)	315	1.4	0.44	3.75	0.71	0.46	0.19	0.49	240 (37)	6.4	37 (5.7)
exp. device4b	300	485	480	195	285	1.01	2.2 (2.6)	471	1.7	0.78	5.51	0.70	0.48	0.19	0.54	<240 (25)	4.8	<50 (5.3)

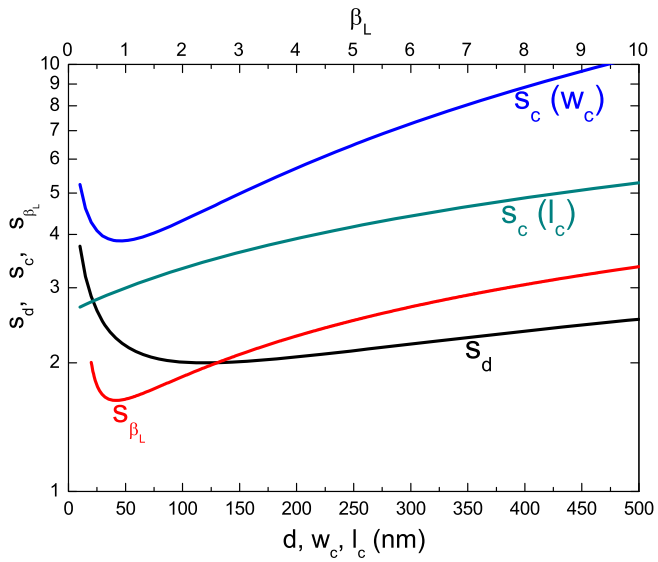

Figure 4. Scaling of the terms $s_d(d)$, $s_{\beta_L}(\beta_L)$ for $\kappa = 0.26$, $s_c(w_c)$ for $l_c = 200$ nm and $s_c(l_c)$ for $w_c = 60$ nm, which enter the spin sensitivity in equation (11) as calculated from equation (12)–(14) with $\lambda_L = 250$ nm.

straightforward, although, the proper choice of d is not very crucial as long as $d \gtrsim 100$ nm. However, in order to avoid too large aspect ratios d/w_c and d/w_J, it is advisable to fix the optimum film thickness to $d_{opt} = d_{min}$. This in turn fixes the optimum value for s_d according to equation (12) to

$$s_{d,opt} = s_d(d_{min}) = 2. \tag{15}$$

The evaluation of equation (13) shows a much more pronounced dependence for $s_{\beta_L}(\beta_L)$ with a clear minimum at $\beta_{L,min} = \kappa(1 + \sqrt{1 + \kappa^{-1}})$, and $s_{\beta_L}(\beta_{L,min}) = \sqrt{\kappa} + \sqrt{\kappa + 1}$. For $\kappa = 0.26$ used in figure 4, we obtain $\beta_{L,min} \approx 0.83$ and $s_{\beta_L}(\beta_{L,min}) \approx 1.6$. Both, $\beta_{L,min}(\kappa)$ and $s_{\beta_L}(\beta_{L,min})$ decrease monotonically with decreasing κ, which implies that κ should be as small as possible. However, as mentioned above, for $\beta_L < 0.4$ the flux noise increases again with further decreasing β_L, and equation (13) is not applicable. Hence, the optimum value for β_L is $\beta_{L,opt} = 0.4$, which then fixes the optimum value for κ via the relation $\beta_{L,min}(\kappa)$ to

$$\kappa_{opt} = \frac{\beta_{L,\,opt}^2}{1 + 2\beta_{L,opt}} = \frac{4}{45} \approx 0.09. \tag{16}$$

Accordingly, the optimum value for s_{β_L} in equation (13) yields

$$s_{\beta_L,opt} = s_{\beta_L}(\beta_{L,opt}, \kappa_{opt}) = \frac{3}{\sqrt{5}} \approx 1.3. \tag{17}$$

We note that according to equation (9), the choice of $\kappa = \kappa_{opt}$ relates the optimum length $l_{J,opt}$ of the bridges containing the GBJs and l_c via

$$l_{J,opt} = \frac{\kappa_{opt}\Phi_0}{4j_0L'} - \frac{b}{2}l_c. \tag{18}$$

Since $b/2 \approx 0.15 \ll 1$, the dependence $l_{J,opt}(l_c)$ is quite weak. For our choice of $j_0 = 3$ mA μm^{-2} and with $\lambda_L = 250$ nm, equation (18) yields $l_{J,opt} \approx 180$ nm $- 0.15 l_c$, i.e. $l_{J,opt}$ decreases only slightly from ~180 nm to ~150 nm for $l_c = 0$ to 200 nm. Hence, the choice of l_c (together with j_0 and λ_L) fixes $l_{J,opt}$.

By inserting $d = d_{opt} = d_0$, $\beta_L = \beta_{L,opt}$ and $\kappa = \kappa_{opt}$ into equation (8), we find for the optimized SQUID inductance

$$L_{opt} \approx 1.3\,\frac{L'}{d_0}\left(r + \frac{l_c}{w_c}\right), \tag{19}$$

i.e. $L_{opt} \approx 2.5$ pH $+ 0.91$ pH $\cdot \frac{l_c}{w_c}$ for $\lambda_L = 250$ nm and roughly a factor of two larger values for $\lambda_L = 335$ nm. Inserting this into equation (7), we find for the optimum junction width

$$w_{J,opt} = \frac{7\Phi_0}{45L'j_0}\,\frac{1}{r + \frac{l_c}{w_c}}. \tag{20}$$

For our choice of $j_0 = 3$ mA μm^{-2}, the prefactor in equation (20) is ≈1.26 μm (750 nm) for $\lambda_L = 250$ (335) nm; i.e. the optimum junction width decreases monotonically with increasing ratio l_c/w_c from ~340 (270) nm for $l_c/w_c = 1$ to ~100 (60)nm for $l_c/w_c = 10$, with $\lambda_L = 250$ (335)nm. For our choice of $j_0 = 3$ mA$/\mu$m^2, the prefactor in equation (20) is ≈1.26 μm (750 nm) for $\lambda_L = 250$ (335) nm; i.e. the optimum junction width decreases monotonically with increasing ratio l_c/w_c from ~340 (270) nm for $l_c/w_c = 1$ to ~100 (60)nm for $l_c/w_c = 10$, with $\lambda_L = 250$ (335)nm.

Finally, as shown in figure 4, the relation $s_c(w_c, l_c)$, given by equation (14) yields a monotonic decrease of s_c with decreasing l_c and a clear minimum in $s_c(w_c)$ at

$$w_{c,min} = \frac{l_c}{4r}\left(\sqrt{1 + \frac{8rw_0}{l_c}} - 1\right), \tag{21}$$

which can be approximated by a power law dependence $w_{c,min} \approx w_c' \cdot (l_c/\text{nm})^{0.35}$ (see dashed and dotted lines in figure 5) with $w_c' = 7$ (4.8) nm for $\lambda_L = 250$ (335) nm. Accordingly, s_c can be minimized by choosing $w_c = w_{c,min}(l_c)$. This yields

$$s_{c,opt}(l_c) = \left\{1 + \frac{w_c'}{w_0}\left(\frac{l_c}{\text{nm}}\right)^{0.35}\right\}\sqrt{r + \frac{\text{nm}}{w_c'}\left(\frac{l_c}{\text{nm}}\right)^{0.65}}. \tag{22}$$

Both, $w_{c,min}(l_c)$ and $s_{c,opt}(l_c)$ decrease monotonically with decreasing l_c. This implies that l_c should be made as small as possible.

All numbers in the following paragraph are quoted for $\lambda_L = 250$ nm. For $l_c = 500$ nm we find $w_{c,min} \approx 60$, which is feasible to realize with our FIB technology; however upon shrinking l_c it becomes increasingly hard to realize devices with optimum constriction width $w_{c,min}(l_c)$. Fortunately, it

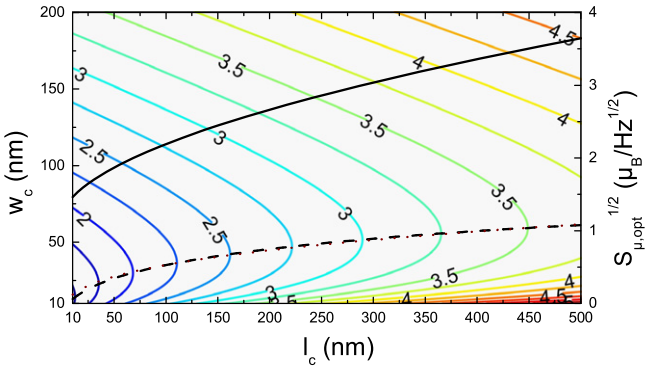

Figure 5. Contour plot of optimized spin sensitivity $S^{1/2}_{\mu,\,\mathrm{opt}}(l_\mathrm{c},\, w_\mathrm{c})$ (for $T = 4.2$ K, $I_0R = 0.5$ mV, $d = 120$ nm and $\beta_L = 0.4$). Numbers at contour lines are in units of $\mu_\mathrm{B}\mathrm{Hz}^{-1/2}$. Dashed and dotted lines show $w_{\mathrm{c,min}}\,(l_\mathrm{c})$ from equation (21) and approximation by power law dependence, respectively. The solid black line shows $S^{1/2}_{\mu,\,\mathrm{opt}}(l_\mathrm{c})$ for $w_\mathrm{c} = w_{\mathrm{c,min}}$. All quantities were calculated for $\lambda_\mathrm{L} = 250$ nm.

turns out that the degradation in spin sensitivity is not very severe if w_c deviates from $w_{\mathrm{c,min}}$, as long as one can keep w_c below, say, 100 nm. This is illustrated in the contour plot in figure 5, which shows the spin sensitivity for optimized d and β_L, i.e. $S^{1/2}_{\mu,\,\mathrm{opt}}(l_\mathrm{c},\, w_\mathrm{c}) = S^{1/2}_{\mu,\,0} \cdot s_{d,\mathrm{opt}} \cdot s_{\beta_L,\mathrm{opt}} \cdot s_\mathrm{c}(l_\mathrm{c},\, w_\mathrm{c}) \approx 0.69\,\mu_\mathrm{B}\,\mathrm{Hz}^{-1/2} \cdot s_\mathrm{c}(l_\mathrm{c},\, w_\mathrm{c})$ for $T = 4.2$ K and $I_0R = 0.5$ mV. Within the plotted range, the spin sensitivity lies in most cases between 2 and 4 $\mu_\mathrm{B}\,\mathrm{Hz}^{-1/2}$, and practically for an optimized device the spin sensitivity is limited by both, the smallest length and linewidth which can be realized for the constriction. The solid line in figure 5 shows $s_{\mathrm{c,opt}}(l_\mathrm{c})$ according to equation (22), i.e. with the additional condition $w_\mathrm{c} = w_{\mathrm{c,min}}\,(l_\mathrm{c})$. If we take $l_\mathrm{c} = 44$ nm, corresponding to $w_{\mathrm{c,min}} = 25$ nm as the current limitation for our FIB patterning technology, we calculate $S^{1/2}_{\Phi,\,\mathrm{opt}} \approx 36\,\mathrm{n}\Phi_0\,\mathrm{Hz}^{-1/2}$ and $\phi_{\mu,\mathrm{opt}} \approx 20\,\mathrm{n}\Phi_0/\mu_\mathrm{B}$, giving an optimized spin sensitivity $S^{1/2}_{\mu,\,\mathrm{opt}} \approx 1.8\,\mu_\mathrm{B}\,\mathrm{Hz}^{-1/2}$. Corresponding SQUID parameters are listed in table 2 ('opt. device 1'). If we take more easily achievable values $w_\mathrm{c} = 60$ nm, $l_\mathrm{c} = 100$ nm and $l_\mathrm{J} = 200$ nm (other input parameters are the same as for the initial optimization), we still get $S^{1/2}_{\mu} = 2.4\,\mu_\mathrm{B}\,\mathrm{Hz}^{-1/2}$ (see table 2 for parameters of 'opt. device 2').

6. Discussion

In the following, we discuss some practical issues regarding the realization of optimized YBCO GBJ nanoSQUIDs. The optimization of the spin sensitivity given by equation (11) certainly depends on the control over the various input parameters, which are not always known precisely. For example, I_0R and j_0 of YBCO GBJs can vary significantly, even on the same chip [34], and sometimes we find values for λ_L significantly above 250 nm.

Starting with the prefactor $S^{1/2}_{\mu,\,0}$, this depends on T and I_0R. Regarding operation temperature T, this will certainly depend on the different applications the nanoSQUIDs will be used for. Hence, this is not a parameter which should be used for optimization. Still, the use of YBCO SQUIDs based on GBJs offers operation from close to their transition temperature T_c (say, 77 K) down to the mK regime. The very large range of operation temperatures is certainly a significant advantage over nanoSQUIDs based on other materials or other junction types such as constriction junctions, which often can only be operated in a very limited temperature interval. The I_0R product does only enter into the expression for the spin sensitivity via $S_{\mu,0} \propto 1/I_0R$. Hence, any variation in I_0R does not affect the optimization of the device geometry. Obviously, as large as possible values for I_0R are helpful for improving the spin sensitivity.

The term for s_d depends on the film thickness d only, and due to the shallow minimum in $s_d(d)$, slight deviations from $d = d_\mathrm{opt} = 120$ nm (for $\lambda_\mathrm{L} = 250$ nm) or larger values for λ_L will have an almost negligible effect on $S^{1/2}_{\mu}$.

The term for s_c depends only on the geometry of the constriction and on λ_L. Here, technological limitations imposed by the patterning technique and possible edge damage effects are crucial, since the smallest achievable s_c will depend on the smallest achievable length l_c and width w_c of the constriction. For our FIB patterning technique, we currently do not know what the final limits for the minimum achievable values for l_c and w_c are, and how strong edge damage effects are. Further investigations are required to determine (and reduce) edge damage effects, which will finally limit the minimum achievable constriction size.

The term s_{β_L} depends on β_L and κ. Here, j_0 enters into the optimization only via $\kappa \propto j_0$. A variation in j_0 will modify the optimum length $l_{\mathrm{J,opt}}(j_0,\, l_\mathrm{c})$ (see equation (18)) and width $w_{\mathrm{J,opt}} \propto 1/j_0$ (see equation (20)), which are required for maintaining $\beta_L \approx 0.4$ (and hence $s_{\beta_L} = s_{\beta_L,\mathrm{opt}}$). Fortunately, j_0 can be measured prior to FIB patterning, which allows to adjust the geometry of the bridges straddling the GBJs. Hence, as long as j_0 does not change significantly after FIB milling [28], and as long as the conditions for $l_{\mathrm{J,opt}}$ and $w_{\mathrm{J,opt}}$ can be fulfilled, the optimized spin sensitivity is not affected by variations in j_0.

A variation in λ_L has a similar effect as a variation in j_0, since $\kappa \propto L'$ and L' increases with λ_L (see table 1). However, it is difficult to determine λ_L prior to FIB patterning in order to adjust w_J and l_J properly. For fixed geometrical parameters, we find that an increase in λ_L from 250 to 335 nm decreases the coupling factor only very slightly, as long as $w_\mathrm{c} \lesssim 100$ nm. The strongest effect comes from the increase in L' by a factor of ~1.7, which increases L and β_L, which both enter into the flux noise. Depending on the value of β_L, this induces an increase in $S^{1/2}_{\Phi}$ (and in $S^{1/2}_{\mu}$) by a factor of approximately 1.4–1.7.

Finally, we would like to comment on two additional practical issues. First, the predicted optimized spin sensitivity around a few $\mu_\mathrm{B}\mathrm{Hz}^{-1/2}$ is in particular due to the reduction in SQUID inductance for an optimized geometry, yielding improved flux noise. However, we should mention that for YBCO SQUIDs the measured flux noise is often significantly

higher than the theoretically predicted one [41]. For the experimental devices listed in table 2 the measured $S_\Phi^{1/2}$ was a factor 3.2–7.5 higher than predicted by equation (4). Hence, we expect the predicted spin sensitivities to be too low by a similar factor if compared with experimental results.

Second, the optimization procedure as described in this work is based on calculating the white thermal noise of the SQUIDs. However, it is well known that I_0 fluctuations can lead to a flux noise S_Φ which scales with the measurement frequency f as $1/f^\alpha$ with α typically close to 1, and it is also known that for YBCO GBJs such a $1/f$ noise contribution can be quite large [41]. For YBCO nanoSQUIDs with improved white thermal noise around 100 $n\Phi_0$ $Hz^{-1/2}$ and below, this implies that the $1/f$ noise may dominate at frequencies up to the MHz range. Hence, in order to utilize the full potential of such SQUIDs, the implementation of bias reversal schemes for suppression of $1/f$ noise from I_0 fluctuations will be very important. Furthermore, for dc SQUIDs based on metallic superconductors such as Nb, it has been shown that below $T \approx 1$ K additional sources of low-frequency excess flux noise may become important, which cannot be eliminated by bias reversal [42] (for more recent work see e.g. [43, 44] and references therein). In YBCO nanoSQUIDs also similar effects may be present and deserve further studies.

7. Conclusions

In summary, we have performed a detailed analysis of the coupling factor ϕ_μ and the spectral density of flux noise S_Φ, and hence of the spin sensitivity $S_\mu^{1/2} = S_\Phi^{1/2}/\phi_\mu$ for grain boundary junction dc nanoSQUIDs. Based on the calculation of ϕ_μ and S_Φ, we derived an explicit expression for the spin sensitivity $S_\mu^{1/2}$ as a function of the geometric and electrical parameters of our devices. This allows for an optimization of $S_\mu^{1/2}$, which predicts a spin sensitivity of a few $\mu_B Hz^{-1/2}$. Such a low value for $S_\mu^{1/2}$ can be achieved by realization of very low inductance nanoSQUIDs with ultra-low flux noise on the order of 100 $n\Phi_0$ $Hz^{-1/2}$ or even below, in the thermal white noise regime. This poses severe challenges on proper readout electronics for such SQUIDs. It remains to be shown whether or not the readout of such ultralow-noise SQUIDs is feasible and whether or not the envisaged values for the spin sensitivity can also be achieved in high fields, which is a major driving force for using these grain boundary junction nanoSQUIDs.

Acknowledgments

J Nagel and T Schwarz acknowledge support by the Carl-Zeiss-Stiftung. We gratefully acknowledge fruitful discussions with D Drung. This work was funded by the Nachwuchswissenschaftlerprogramm of the Universität Tübingen, and by the Deutsche Forschungsgemeinschaft (DFG) via projects KO 1303/13-1 and SFB/TRR 21 C2.

References

[1] Wernsdorfer W 2001 *Adv. Chem. Phys.* **118** 99
[2] Ketchen M, Awschalom D, Gallagher W, Kleinsasser A, Sandstrom R, Rozen J and Bumble B 1989 *IEEE Trans. Magn.* **25** 1212
[3] Wernsdorfer W, Mailly D and Benoit A 2000 *J. Appl. Phys.* **87** 5094
[4] Bouchiat V 2009 *Supercond. Sci. Technol.* **22** 064002
[5] Gallop J 2003 *Supercond. Sci. Technol.* **16** 1575
[6] Awschalom D D, Rozen J R, Ketchen M B, Gallagher W J, Kleinsasser A W, Sandstrom R L and Bumble B 1988 *Appl. Phys. Lett.* **53** 2108
[7] Hasselbach K, Mailly D and Kirtley J R 2002 *J. Appl. Phys.* **91** 4432
[8] Lam S K H and Tilbrook D L 2003 *Appl. Phys. Lett.* **82** 1078
[9] Cleuziou J-P, Wernsdorfer W, Bouchiat V, Ondarçuhu T and Monthioux M 2006 *Nat. Nanotechnology* **1** 53
[10] Troeman A G P, Derking H, Borger B, Pleikies J, Veldhuis D and Hilgenkamp H 2007 *Nano Lett.* **7** 2152
[11] Koshnick N C, Huber M E, Bert J A, Hicks C W, Large J, Edwards H and Moler K A 2008 *Appl. Phys. Lett.* **93** 243101
[12] Hao L, Macfarlane J C, Gallop J C, Cox D, Beyer J, Drung D and Schurig T 2008 *Appl. Phys. Lett.* **92** 192507
[13] Foley C P and Hilgenkamp H 2009 *Supercond. Sci. Technol.* **22** 064001
[14] Wernsdorfer W 2009 *Supercond. Sci. Technol.* **22** 064013
[15] Finkler A, Segev Y, Myasoedov Y, Rappaport M L, Ne'eman L, Vasyukov D, Zeldov E, Huber M E, Martin J and Yacoby A 2010 *Nano Lett.* **10** 1046
[16] Giazotto F, Peltonen J T, Meschke M and Pekola J P 2010 *Nat. Phys.* **6** 254
[17] Nagel J, Kieler O F, Weimann T, Wölbing R, Kohlmann J, Zorin A B, Kleiner R, Koelle D and Kemmler M 2011 *Appl. Phys. Lett.* **99** 032506
[18] Martínez-Pérez M J, Bellido E, de Miguel R, Sesé J, Lostao A, Gómez-Moreno C, Drung D, Schurig T, Ruiz-Molina D and Luis F 2011 *Appl. Phys. Lett.* **99** 032504
[19] Romans E J, Rozhko S, Young L, Blois A, Hao L, Cox D and Gallop J C 2011 *IEEE Trans. Appl. Supercond.* **21** 404
[20] Russo R, Granata C, Esposito E, Peddis D, Cannas C and Vettoliere A 2012 *Appl. Phys. Lett.* **101** 122601
[21] Wölbing R, Nagel J, Schwarz T, Kieler O, Weimann T, Kohlmann J, Zorin A B, Kemmler M, Kleiner R and Koelle D 2013 *Appl. Phys. Lett.* **102** 192601
[22] Granata C, Vettoliere A, Russo R, Fretto M, Leo N D and Lacquaniti V 2013 *Appl. Phys. Lett.* **103** 102602
[23] Levenson-Falk E M, Vijay R, Antler N and Siddiqi I 2013 *Supercond. Sci. Technol.* **26** 005015
[24] Vasyukov Denis *et al* 2013 *Nat. Nanotechnology* **8** 639
[25] Arpaia R, Arzeo M, Nawaz S, Charpentier S, Lombardi F and Bauch T 2014 *Appl. Phys. Lett.* **104** 072603
[26] Drung D, Storm J-H, Ruede F, Kirste A, Regin M, Schurig T, Repollés A M, Sesé J and Luis F 2014 *IEEE Trans Appl. Supercond.* **24** 1600206
[27] Chen L, Wernsdorfer W, Lampropoulos C, Christou G and Chiorescu I 2010 *Nanotechnology* **21** 405504
[28] Nagel J *et al* 2011 *Supercond. Sci. Technol.* **24** 015015
[29] Schwarz T, Nagel J, Wölbing R, Kemmler M, Kleiner R and Koelle D 2013 *ACS Nano* **7** 844
[30] Khapaev M, Kupriyanov M, Goldobin E and Siegel M 2003 *Supercond. Sci. Technol.* **16** 24
[31] Nagel J *et al* 2013 *Phys. Rev.* B **88** 064425
[32] Koch R H, DiVincenzo D P and Clarke J 2007 *Phys. Rev. Lett.* **98** 267003

[33] Chesca B, Kleiner R and Koelle D 2004 Fundamentals and Technology of SQUIDs and SQUID systems *The SQUD Handbook* ed J Clarke and A I Braginski vol 1 (Weinheim: Wiley) pp 29–92 chapter 2
[34] H Hilgenkamp and J Mannhart 2002 *Rev. Mod. Phys.* **74** 485
[35] Moeckly B H and Buhrman R A 1995 *IEEE Trans. Appl. Supecond.* **5** 3414–7
[36] McBrien P F, Hadfield R H, Booij W E, Moya A, Kahlmann F, Blamire M G, Pegrum C M and Tarte E J 2000 *Physica* C **339** 88
[37] Navacerrada M A, Lucía M L, Sánchez-Soto L L, Sánchez Quesada F, Sarnelli E and Testa G 2005 *Phys. Rev.* B **71** 014501
[38] Beck A, Froehlich O M, Koelle D, Gross R, Sato H and Naito M 1996 *Appl. Phys. Lett.* **68** 3341
[39] Zaitsev A G, Schneider R, Linker G, Ratzel F, Smithey R, Schweiss P, Geerk J, Schwab R and Heidinger R 2002 *Rev. Sci. Instrum.* **73** 335
[40] For exp. device3 and 4b, we find low-frequency excess noise up to the bandwidth of our readout electronics. Hence, we can only give an upper limit for the white thermal noise (flux noise and spin sensitivity) for these devices.
[41] Koelle D, Kleiner R, Ludwig F, Dantsker E and Clarke J 1999 *Rev. Mod. Phys.* **71** 631
[42] Wellstood F C, Urbina C and Clarke J 1987 *Appl. Phys. Lett.* **50** 772
[43] Choi S, Lee D-H, Louie S G and Clarke J 2009 *Phys. Rev. Lett.* **103** 197001
[44] Drung D, Beyer J, Storm J-H, Peters M and Schurig T 2011 *IEEE Trans. Appl. Supercond.* **21** 340

Publication 3

Low-Noise $YBa_2Cu_3O_7$ Nano Superconducting Quantum Interference Devices for Magnetization Reversal Measurements on Magnetic Nanoparticles

T. Schwarz,[1] R. Wölbing,[1] C. F. Reiche,[2] B. Müller,[1]
M. J. Martínez-Pérez,[1] T. Mühl,[2] B. Büchner,[2] R. Kleiner,[1] and D. Koelle[1]

[1] *Physikalisches Institut – Experimentalphysik II and Center for Collective Quantum Phenomena in LISA$^+$, Universität Tübingen, Auf der Morgenstelle 14, D-72076 Tübingen, Germany*

[2] *Leibniz Institute for Solid State and Materials Research IFW Dresden, Helmholtzstr. 20, 01069 Dresden, Germany*

(Dated: September 30, 2014)

We fabricated $YBa_2Cu_3O_7$ (YBCO) direct current (dc) nano superconducting quantum interference devices (nanoSQUIDs) based on grain boundary Josephson junctions by focused ion beam patterning. Characterization of electric transport and noise properties at 4.2 K in magnetically shielded environment yields a very small inductance L of a few pH for an optimized device geometry. This in turn results in very low values of flux noise $< 50\,\mathrm{n}\Phi_0/\mathrm{Hz}^{1/2}$ in the thermal white noise limit, which yields spin sensitivities of a few $\mu_B/\mathrm{Hz}^{1/2}$ (Φ_0 is the magnetic flux quantum and μ_B is the Bohr magneton). We observe frequency-dependent excess noise up to 7 MHz, which can only partially be eliminated by bias reversal readout. This indicates the presence of fluctuators of unknown origin, possibly related to defect-induced spins in the $SrTiO_3$ substrate. We demonstrate the potential of using such YBCO nanoSQUIDs for the investigation of small spin systems, by placing a 39 nm diameter Fe nanowire, encapsulated in a carbon nanotube, on top of a non-optimized YBCO nanoSQUID and by measuring the magnetization reversal of the Fe nanowire via the change of magnetic flux coupled to the nanoSQUID. The measured flux signals upon magnetization reversal of the Fe nanowire are in very good agreement with estimated values, and the determined switching fields indicate magnetization reversal of the nanowire via curling mode.

PACS numbers: 85.25.Dq, 74.78.Na, 75.75.-c 74.72.-h 74.25.F- 74.40.De 85.25.CP,

I. INTRODUCTION

Small spin systems or magnetic nanoparticles (MNPs), like single molecular magnets, nanowires or nanotubes behave very different from magnetic bulk material, which makes them very interesting, both for basic research and applications, ranging from spintronics and spin-based quantum information processing to industrial use of ferrofluidic devices and biomedical applications[1–7]. Due to their nanoscale size, MNPs have very small magnetic moments, which does not allow to use standard magnetic characterization techniques for the investigation of their properties. In one approach, which has been pioneered by Wernsdorfer *et al.*[8], MNPs are placed very close to miniaturized superconducting quantum interference devices (SQUIDs), often referred to as microSQUIDs or nanoSQUIDs[9–25], and the magnetization reversal of MNPs is measured directly via the change of stray magnetic flux coupled to the microSQUIDs or nanoSQUIDs. Major challenges for this application are the development of SQUIDs (i) with ultra-low flux noise, which can be achieved via the reduction of the inductance L of the SQUID loop and (ii) which can be operated in very large magnetic fields (up to the Tesla range), without significant degradation of their noise performance.

The most common approach for the realization of direct current (dc) nanoSQUIDs uses two constriction-type Josephson junctions (cJJs) intersecting the SQUID loop[11,12,14,16,23,26,27]. In this case, optimum coupling between a MNP and the nanoSQUID is achieved by placing the particle directly on top of one of the cJJs. The use of cJJs offers the possibility to operate the SQUIDs in strong magnetic fields. However, if conventional metallic superconductors such as Pb or Nb are used, high-field operation is limited by the upper critical field of typically one Tesla for thin films[28]. Still, it has been demonstrated that by using ultrathin films, this limitation can be overcome[29]. However, with ultrathin films the SQUID inductance L is dominated by a large kinetic inductance contribution, which yields large flux noise. To date, the most successful approach is the SQUID-on-tip (SOT)[26]. With the so far smallest Pb SOT with 46 nm effective loop diameter and 15 nm film thickness, ultra-low flux noise down to $50\,\mathrm{n}\Phi_0/\mathrm{Hz}^{1/2}$ at 4.2 K has been demonstrated[28] (Φ_0 is the magnetic flux quantum). The inductance for a slightly larger device (56 nm effective diameter) was estimated as $L = 5.8$ pH. The SOT technology is extremely powerful for high-resolution scanning SQUID microscopy, and provided for the first time a spin sensitivity below $1\,\mu_\mathrm{B}/\mathrm{Hz}^{1/2}$ for certain intervals of applied magnetic field up to about 1 Tesla (μ_B is the Bohr magneton), estimated for a point-like MNP with 10 nm distance to the SOT. However, maintaining the optimum flux bias point in variable magnetic field is not possible; i.e. the flux noise and spin sensitivity strongly depend on the applied field, which makes such devices less interesting for the investigation of magnetization reversal of MNPs.

An alternative approach is the use of $YBa_2Cu_3O_7$ (YBCO) dc nanoSQUIDs with grain boundary Josephson junctions (GBJJs) for operation at temperature $T = 4.2$ K and below[30]. Magnetization reversal of a MNP can

be detected by applying an in-plane magnetic field perpendicular to the grain boundary, i.e. without significant suppression of the GBJJ critical currents. The huge upper critical field of YBCO in the range of tens of Tesla offers the possibility for operation in strong fields up to the Tesla range, without using ultrathin films[31]. Hence, very low inductance devices with potentially ultra-low flux noise can be realized.

Very recently, we performed an optimization study for the design of YBCO nanoSQUIDs[32]. This is based on the calculation of the coupling factor ϕ_μ, i.e. the amount of magnetic flux coupled to the SQUID per magnetic moment of a point-like MNP, placed on top of a narrow constriction inserted into the SQUID loop. This additional constriction allows for the optimization of ϕ_μ (via constriction geometry) without affecting the junctions. In addition, we performed numerical simulations to calculate the SQUID inductance and root-mean-square (rms) spectral density of flux noise $S_{\Phi,\mathrm{w}}^{1/2}$ in the thermal white noise limit. This enabled us to predict the spin sensitivity in the thermal white noise limit $S_{\mu,\mathrm{w}}^{1/2} = S_{\Phi,\mathrm{w}}^{1/2}/\phi_\mu$ for our devices as a function of all relevant device parameters. This optimization study predicts optimum performance for a YBCO film thickness $d \approx 120\,\mathrm{nm}$, which allows to realize nanoSQUIDs with very small L of a few pH. For optimized devices, we predict $S_{\Phi,\mathrm{w}}^{1/2}$ of several tens of $\mathrm{n}\Phi_0/\mathrm{Hz}^{1/2}$ and $\phi_\mu \sim 10 - 20\,\mathrm{n}\Phi_0/\mu_\mathrm{B}$ (for a MNP placed 10 nm above the YBCO film on top of the constriction), yielding a spin sensitivity $S_{\mu,\mathrm{w}}^{1/2}$ of a few $\mu_\mathrm{B}/\mathrm{Hz}^{1/2}$.

Here, we report on the realization of optimized YBCO nanoSQUIDs based on GBJJs and on the experimental determination of their electric transport and noise properties in magnetically shielded environment at $T = 4.2\,\mathrm{K}$. To demonstrate the suitability of our YBCO nanoSQUIDs for the detection of small spin systems, we present the measurement of the magnetization reversal (up to $\sim 200\,\mathrm{mT}$ at $T = 4.2\,\mathrm{K}$) of a Fe nanowire with diameter $d_\mathrm{Fe} = 39\,\mathrm{nm}$, which was positioned close the SQUID loop.

II. DEVICE FABRICATION AND EXPERIMENTAL SETUP

The fabrication of the devices was carried out according to Refs. [30,31]. A c-axis oriented YBCO thin film of thickness d was grown epitaxially by pulsed laser deposition on a $SrTiO_3$ (STO) [001] bicrystal substrate with a 24° grain boundary misorientation angle. An in-situ evaporated Au layer of thickness d_Au serves as shunt resistance to provide non-hysteretic current-voltage characteristics (IVCs). SQUIDs with smallest line widths down to 50 nm were patterned by focused ion beam (FIB) milling with 30 keV Ga ions. The Au layer also minimizes Ga implantation into the YBCO film during FIB milling.

For characterization of the device properties, electric transport and noise measurements were performed in an electrically and magnetically shielded environment at $T = 4.2\,\mathrm{K}$, i.e. with the samples immersed into liquid He. By applying a modulation current I_mod across the constriction, the magnetic flux coupled to the SQUID can be modulated. This allows flux biasing at the optimum working point and operation in a flux locked loop (FLL) mode[33]. To determine the spectral density of flux noise S_Φ vs frequency f of the devices we used a Magnicon SEL-1 SQUID electronics[34] in direct readout mode[35], which was either operated in open loop mode (maximum bandwidth ~7 MHz), or in FLL mode (maximum bandwidth ~500-800 kHz). The SEL electronics allows for SQUID operation either with constant bias current (dc bias) or with a bias reversal readout scheme (maximum bias reversal frequency $f_\mathrm{br} = 260\,\mathrm{kHz}$), to reduce $1/f$ noise caused by fluctuations of the critical currents $I_{0,1}$ and $I_{0,2}$ of the Josephson junctions 1 and 2, respectively[33].

Below we present data of our best device, SQUID-1, with a $d = 120\,\mathrm{nm}$ thick YBCO film. Figure 1 shows a scanning electron microscope (SEM) image of SQUID-1. The loop size $350 \times 190\,\mathrm{nm}^2$ is given by the length l_J of the bridges straddling the grain boundary and by the length l_c of the constriction. SQUID-1 has junction widths $w_\mathrm{J1} = 210\,\mathrm{nm}$ and $w_\mathrm{J2} = 160\,\mathrm{nm}$ and a constriction width $w_\mathrm{c} = 85\,\mathrm{nm}$. The parameters for SQUID-1 are summarized in Table I. For comparison, we also include parameters for a similar device, SQUID-2, which has the same YBCO film thickness, however slightly larger inductance $L = 6.3\,\mathrm{pH}$, and about a factor of 2.5 smaller characteristic voltage $V_\mathrm{c} \equiv I_\mathrm{c}R_\mathrm{N}$. I_c is the maximum critical current and R_N is the asymptotic normal state resistance of the SQUID. Details on electric transport and noise characteristics of SQUID-2 are presented in Sec. I of the Supplemental Material[36]. Table I also includes parameters for SQUID-3, which was used for measurements on an Fe nanowire in a high-field setup, as discussed further below.

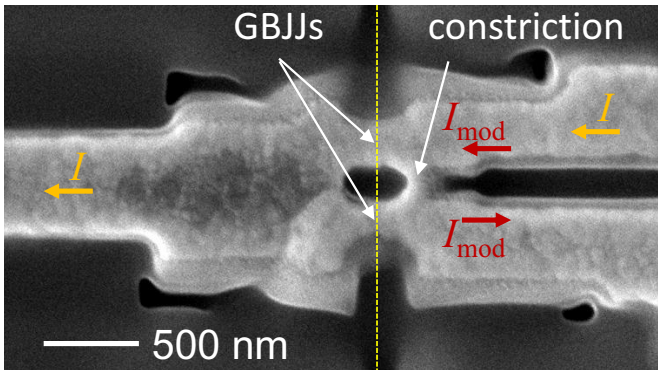

FIG. 1: (Color online) SEM image of YBCO nanoSQUID-1. Vertical dashed line indicates position of the grain boundary intersecting the two SQUID arms. Horizontal arrows indicate paths for modulation current I_mod across the constriction and bias current I across the grain boundary Josephson junctions.

III. SQUID-1: ELECTRIC TRANSPORT AND NOISE

A. SQUID-1: dc characteristics

Figure 2 shows the dc characteristics of SQUID-1. Figure 2(a) shows IVCs for $I_{\rm mod} = 0$ and two values of $I_{\rm mod}$, corresponding to maximum and minimum critical current. The IVCs are slightly hysteretic with maximum critical current $I_{\rm c} = 960\,\mu$A and $R_{\rm N} = 2.0\,\Omega$, which yields $V_{\rm c} = 1.92\,$mV. The inset of Fig. 2(a) shows

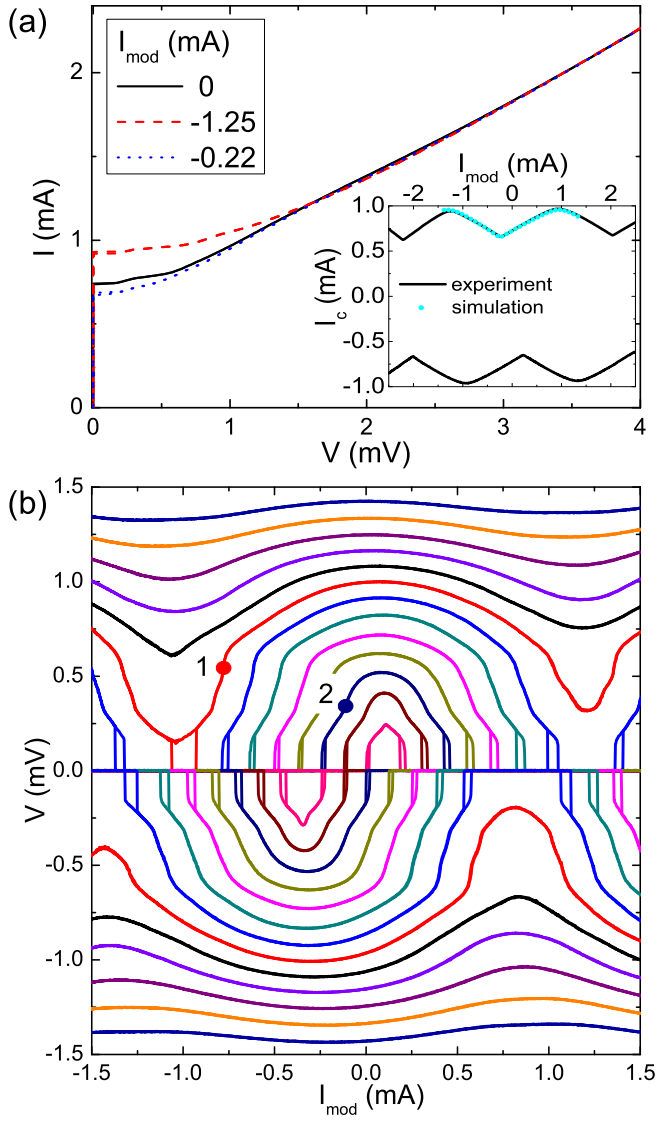

FIG. 2: (Color online) SQUID-1 dc transport characteristics. (a) Measured IVCs for three different values of $I_{\rm mod}$, including flux bias ($I_{\rm mod}$) values which yield maximum and minimum critical current. Inset: measured $I_{\rm c}(I_{\rm mod})$ for positive and negative current bias (solid lines) and numerical simulations (dots). (b) Measured $V(I_{\rm mod})$ for bias currents $|I| = 0.64\ldots1.12\,$mA (in $40\,\mu$A steps). Points 1 and 2 are bias points with V_Φ=12 and 4.5 mV/Φ_0, respectively.

the modulation of the critical current $I_{\rm c}(I_{\rm mod})$. From the modulation period, we find for the magnetic flux Φ coupled to the SQUID by $I_{\rm mod}$ the mutual inductance $M = \Phi/I_{\rm mod} = 0.44\,\Phi_0/$mA $= 0.91\,$pH. We performed numerical simulations, based on the resistively and capacitively shunted junction (RCSJ) model, to solve the coupled Langevin equations which include thermal fluctuations of the junction resistances[37]. From simulations of the $I_{\rm c}(I_{\rm mod})$ characteristics [cf. inset of Fig. 2(a)] we obtain for the screening parameter $\beta_L = 2I_0L/\Phi_0 = 1.8$ (with $I_0 = (I_{0,1} + I_{0,2})/2$), which yields a SQUID inductance $L = 3.9\,$pH. We do find good agreement between the measured and simulated $I_{\rm c}(I_{\rm mod})$ characteristics if we include an inductance asymmetry $\alpha_L \equiv (L_2 - L_1)/(L_2 + L_1) = 0.20$ (L_1 and L_2 are the inductances of the two SQUID arms) and a critical current asymmetry $\alpha_I \equiv (I_{0,2} - I_{0,1})/(I_{0,2} + I_{0,1}) = 0.27$. These asymmetries are caused by asymmetric biasing of the SQUID and by asymmetries of the device itself.

$V(I_{\rm mod})$ is plotted in Fig. 2(b) for different bias currents. The transfer function, i.e. the maximum value of $\partial V/\partial\Phi$, in the non-hysteretic regime is $V_\Phi \approx 12\,$mV/Φ_0 [at $I = 0.92\,$mA; cf. point 1 in Fig. 2(b)].

B. SQUID-1: Noise data

1. *Open loop mode*

Figure 3(a) shows the rms spectral density of flux noise $S_\Phi^{1/2}(f)$ of SQUID-1, measured in open loop mode to reach the highest possible bandwidth of the readout electronics. Due to the limitation in the maximum bias current of the readout electronics, noise spectra were taken at $I = 0.72\,$mA with a transfer function $V_\Phi = 4.5\,$mV/Φ_0 [cf. point 2 in Fig. 2(b)]. Up to the cutoff frequency $f_{\rm 3dB} = 7\,$MHz there is no white flux noise observable. Instead, the flux noise scales roughly as $S_\Phi \propto 1/f$, with $S_\Phi^{1/2} \approx 10\,\mu\Phi_0/{\rm Hz}^{1/2}$ at $f = 100\,$Hz and $1\,\mu\Phi_0/{\rm Hz}^{1/2}$ at 10 kHz. This level of low-frequency excess noise is quite typical for YBCO GBJJ SQUIDs (also at $T = 77\,$K) and has been ascribed to critical current fluctuations in the GBJJs[38]. However, due to the limitation by thermal white noise, typically between 1 and $10\,\mu\Phi_0/{\rm Hz}^{1/2}$ for low-noise YBCO SQUIDs, this f-dependent excess noise has not been observed so far up to the MHz range. We note that for YBCO nanoSQUIDs implementing cJJs[27], a frequency-dependent $1/f$-like excess noise at $T = 8\,$K of almost the same level as for SQUID-1 was reported very recently, and was also attributed to critical current noise. For frequencies above 10 kHz, the flux noise of the YBCO nanoSQUID in Ref. [27] was limited by amplifier background noise.

For a more detailed analysis of the measured flux noise $S_\Phi(f)$, we applied an algorithm[39] to decompose the noise spectra into a sum of Lorentzians $F_i(f) = F_{0,i}/[1 + (f/f_{{\rm c},i})^2]$ plus a white noise contribution $F_{\rm w}$. The noise

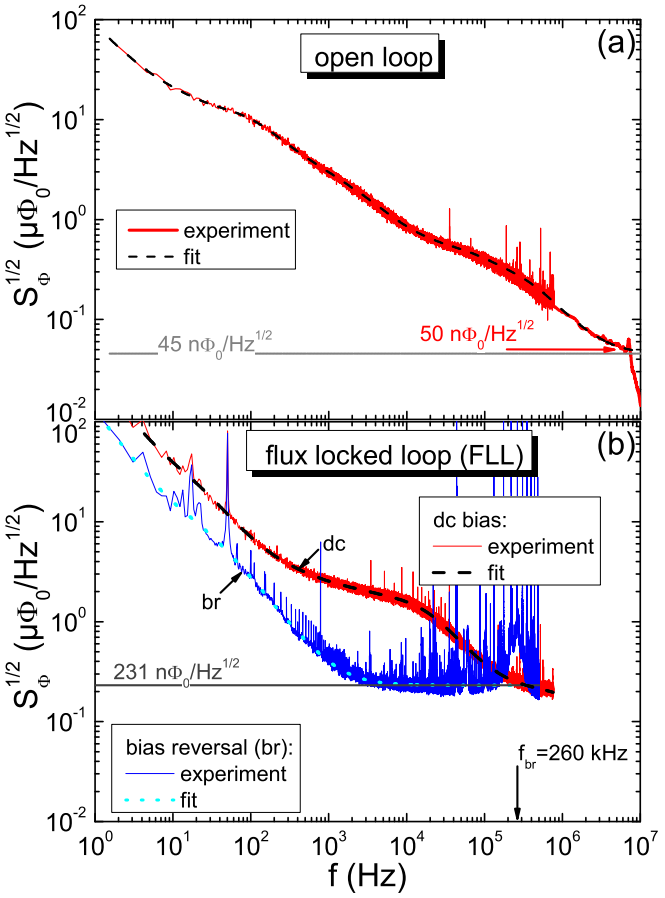

FIG. 3: (Color online) rms flux noise of SQUID-1. (a) Measured in open loop mode at bias point 2 ($I = 0.72\,\mathrm{mA}$) in Fig. 2(b). Dashed line is a fit to the measured spectrum with white noise as indicated by horizontal line. (b) Measured in FLL mode with dc bias and bias reversal ($|I| = 0.43\,\mathrm{mA}$, $V_\Phi = 4.4\,\mathrm{mV}/\Phi_0$). Vertical arrow indicates bias reversal frequency f_{br}. Dashed and dotted lines are fits to the spectra; horizontal lines indicate fitted white noise.

spectrum measured for SQUID-1 in open loop can be very well fitted by $F_{\mathrm{op}}(f) = F_{\mathrm{w,op}} + F_{\mathrm{s,op}} + \sum_{i=1}^{16} F_{\mathrm{op},i}(f)$, i.e., the superposition of a white noise contribution with $F^{1/2}_{\mathrm{w,op}} = 45\,\mathrm{n}\Phi_0/\mathrm{Hz}^{1/2}$ plus a $1/f^2$ spectrum $F_{\mathrm{s,op}}$ (i.e. one or more Lorentzians with characteristic frequencies f_{c} well below 1 Hz) with $F^{1/2}_{\mathrm{s,op}}(1\,\mathrm{Hz}) = 84\,\mu\Phi_0/\mathrm{Hz}^{1/2}$ plus 16 Lorentzians, with $f_{\mathrm{c},i}$ ranging from 2.6 Hz to 2.6 MHz; for more details see Sec. III of the Supplemental Material[36]. Hence, the decomposition of the spectrum into Lorentzians yields an estimate of the white rms flux noise $S^{1/2}_{\Phi,\mathrm{w}} \approx 45\,\mathrm{n}\Phi_0/\mathrm{Hz}^{1/2}$ for SQUID-1. We note that this value for $S^{1/2}_{\Phi,\mathrm{w}}$ is only a factor of 1.8 above the value which we obtain from numerical simulations of the coupled Langevin equations[37] at $T = 4.2\,\mathrm{K}$ for the parameters of SQUID-1.

Taking the measured flux noise at 7 MHz as an upper limit for $S^{1/2}_{\Phi,\mathrm{w}}$, we still obtain a very low white rms flux noise, i.e. $S^{1/2}_{\Phi,\mathrm{w}} < 50\,\mathrm{n}\Phi_0/\mathrm{Hz}^{1/2}$. This more conservative estimate for the white rms flux noise level is an improvement by more than an order of magnitude compared to our non-optimized devices operated at 4.2 K and compared to the lowest value reported so far for a YBCO SQUID (at 8 K) very recently[27]. Furthermore, this value is the same as the lowest value reported for a Pb SOT operated at 4.2 K[28] and among the lowest flux noise levels ever achieved for a SQUID[9,40,41].

For the geometry of SQUID-1, we calculate[32] a coupling factor $\Phi_\mu = 13.4\,\mathrm{n}\Phi_0/\mu_{\mathrm{B}}$ (10 nm above the YBCO film). With $S^{1/2}_{\Phi,\mathrm{w}} < 50\,\mathrm{n}\Phi_0/\mathrm{Hz}^{1/2}$, this yields an upper limit for the spin sensitivity (white noise limit) of $S^{1/2}_{\mu,\mathrm{w}} < 3.7\,\mu_{\mathrm{B}}/\mathrm{Hz}^{1/2}$. If we take the fitted white flux noise of $45\,\mathrm{n}\Phi_0/\mathrm{Hz}^{1/2}$, we obtain $S^{1/2}_{\mu,\mathrm{w}} = 3.4\,\mu_{\mathrm{B}}/\mathrm{Hz}^{1/2}$. Hence, the achieved performance matches very well the predictions of our recent optimization study[32].

2. *FLL mode: dc bias vs bias reversal*

Although the achieved low level of white flux noise for SQUID-1 is encouraging, one certainly would like to extend such a low-noise performance down to much lower frequencies. Therefore, we also performed noise measurements in FLL mode (with $\sim 700\,\mathrm{kHz}$ bandwidth) and compared measurements with dc bias and bias reversal (with $f_{\mathrm{br}} = 260\,\mathrm{kHz}$). We note that the measurements in FLL mode were performed within a different cooling cycle, after SQUID-1 already showed a slight degradation in I_{c}[42]. Still, we were able to find a working point (at $|I| = 0.43\,\mathrm{mA}$) which yielded almost the same transfer function, $4.4\,\mathrm{mV}/\Phi_0$, as for the measurement before degradation in open loop mode.

Figure 3(b) shows rms flux noise spectra taken with dc bias and bias reversal. Comparing first the FLL dc bias measurement with the open loop data, we note that the noise levels at f_{br} coincide. For $f < f_{\mathrm{br}}$ the noise levels of the open loop and FLL dc bias data are similar, however, the shape of the spectra differ, which we attribute to the above mentioned degradation and variations between different cooling cycles. The dashed line in Fig. 3(b) is a fit to the measured spectral density of flux noise by $F_{\mathrm{dc}}(f) = F_{\mathrm{w,dc}} + \sum_{i=1}^{15} F_{\mathrm{dc},i}(f)$, i.e., the superposition of 15 Lorentzians, with $f_{\mathrm{c},i}$ ranging from 0.8 Hz to 6.8 MHz, plus a white noise contribution $F^{1/2}_{\mathrm{w,dc}} = 41\,\mathrm{n}\Phi_0/\mathrm{Hz}^{1/2}$, which we fixed to a value similar to the white noise level determined for the open loop measurement; for more details see Sec. III of the Supplemental Material[36].

Applying bias reversal, one expects a suppression of the contributions due to in-phase and out-of-phase critical current fluctuations of the GBJJs[38]. If the f-dependent excess noise below f_{br} would arise solely from I_0 fluctuations, one would expect in bias reversal mode a frequency-independent noise for frequencies below the peak at f_{br}, at a level which is given by the noise measured at f_{br} in dc bias mode. This is what we observe

TABLE I: Parameters of optimized SQUID-1 and -2 and of SQUID-3 used for measurements on Fe nanowire. Values for V_ϕ correspond to working points of noise measurements. Values in brackets for $S_{\Phi,\mathrm{w}}^{1/2}$ and $S_{\mu,\mathrm{w}}^{1/2}$ of SQUID-1 are based on fitted noise spectrum. All devices have $d_{\mathrm{Au}} = 70\,\mathrm{nm}$. SQUID-1 and -3 were measured at 4.2 K, SQUID-2 was measured at 5.3 K.

	d	l_c	l_J	w_c	$w_{\mathrm{J}1}$	$w_{\mathrm{J}2}$	β_L	L	I_c	R_N	$I_\mathrm{c}R_\mathrm{N}$	V_Φ	$S_{\Phi,\mathrm{w}}^{1/2}$	ϕ_μ	$S_{\mu,\mathrm{w}}^{1/2}$
units	nm	nm	nm	nm	nm	nm		pH	μA	Ω	mV	mV/Φ_0	nΦ_0/Hz$^{1/2}$	nΦ_0/μ_B	μ_B/Hz$^{1/2}$
SQUID-1	120	190	350	85	210	160	1.8	3.9	960	2.0	1.92	4.4	< 50 (45)	13	< 3.7 (3.4)
SQUID-2	120	230	370	100	180	230	0.94	6.3	311	2.5	0.78	1.7	< 83	12	< 6.7
SQUID-3	75	190	340	100	270	340	0.95	28	69	2.3	0.16	0.65	< 1450	15	< 98

for frequencies down to a few kHz, with a f-independent noise $F_{\mathrm{w,br}} = 231\,\mathrm{n}\Phi_0/\mathrm{Hz}$. For lower frequencies, however, we still find a strong f-dependent excess noise in bias reversal mode, which hence cannot be attributed to I_0 fluctuations.

The spectral density of flux noise measured in bias reversal mode can be well approximated [cf. dotted line in Fig. 3(b)] by $F_{\mathrm{br}}(f) = F_{\mathrm{w,br}} + F_{\mathrm{s,br}} + \sum_{i=1}^{6} F_{\mathrm{br},i}(f)$, with $F_{\mathrm{s,br}}^{1/2}(1\,\mathrm{Hz}) = 128\,\mu\Phi_0/\mathrm{Hz}^{1/2}$ and $f_{\mathrm{c},i}$ of the six Lorentzians ranging from 21 Hz to 5 kHz; for more details see Sec. III of the Supplemental Material[36].

Obviously, below a few kHz the low-frequency excess noise is dominated by slow fluctuators, which cannot be attributed to I_0 fluctuations. For different working points (I and I_{mod}) and also for other devices, the observation of low-f excess noise in bias reversal mode was reproducible [cf. flux noise data of SQUID-2 (from $T = 6\,\mathrm{K}$ up to 65 K) and of SQUID-3 (at $T = 4.2\,\mathrm{K}$) in Sec. I and Sec. II, respectively, of the Supplemental Material[36]].

Considering the narrow linewidths of the SQUID structures, we estimate a threshold field for trapping of Abrikosov vortices[43] to be well above 1 mT. Since the measurements were performed in magnetically shielded environment well below 100 nT, the presence of Abrikosov vortices as the source of the observed low-f fluctuators is very unlikely.

Low-frequency excess noise, which does neither arise from I_0 nor from vortex fluctuations, has been reported during the last decades for SQUIDs based on conventional superconductors like Nb, Pb, PbIn and Al, in particular at temperatures well below 1 K[44]. This issue has recently been revived due to the increasing interest in the development of flux qubits and SQUIDs for ultra-low temperature applications[45]. Various models have been suggested to describe the origin of such low-f excess noise, e.g. based on the coupling of magnetic moments associated with trapped electrons[46] or surface states[47,48], although the microscopic nature of defects as sources of excess 'spin noise' still remains unclear.

For YBCO SQUIDs, excess low-f spin noise has not been addressed so far. However, it seems unlikely that defects may not play a role as magnetic fluctuators for SQUIDs based on cuprates or any other oxide superconductors, which are often fabricated on oxide substrates, in particular on STO, which is also used for the nanoSQUIDs discussed here.

The emergence and modification of magnetism at interfaces and surfaces of oxides, which are diamagnetic in the bulk, is currently an intensive field of research[49–51]. For STO, oxygen vacancy-induced magnetism has been predicted[52], and experimental studies suggest ferromagnetic ordering up to room temperature[53], e.g. for defects induced by ion irradiation of single crystalline STO[54]. Furthermore, defect-induced magnetism in oxide grain boundaries and related defects have been suggested to be the intrinsic origin of ferromagnetism in oxides[55].

Although we can only speculate at the current stage of our investigations, it seems possible that the observed low-f excess noise in our nanoSQUIDs (in FLL bias reversal mode) is due to spin noise from defect-induced magnetism in the STO close to the SQUID loop. Possible candidates are defects induced at the STO grain boundary underneath the YBCO GBJJs or FIB milling-induced defects close to the constriction, where the coupling factor is strongest and may exceed the estimate given in Ref. [46] by three orders of magnitude. Obviously, further investigations on the impact and nature of such defects in our devices are needed and will be the subject of further studies. Such studies will include detailed noise measurements (dc vs bias reversal, variable flux bias, temperature and magnetic field) to characterize and understand the f-dependent noise sources and, hopefully, eliminate them. Furthermore, readout with bias reversal at higher frequency up to the MHz range in FLL mode has to be implemented, in order maintain the achieved ultra-low white flux noise level down to lower frequencies. And finally, for applications of our nanoSQUIDs, it will be important do avoid degradation in time. This shall be achieved by adding a suitable passivation layer, however, without introducing f-dependent excess noise.

IV. SQUID-3: MAGNETIZATION REVERSAL OF FE NANOWIRE

As a proof of principle, we demonstrate nanoSQUID measurements on the magnetization reversal of a Fe nanowire which is encapsulated in a carbon nanotube (CNT)[56]. Such iron-filled CNTs (FeCNTs) are of fundamental interest with respect to studies on nanomagnetism. Furthermore, they are attractive for various applications, e.g. as tips in magnetic force microscopy[57,58]. The Fe-nanowire, which contains mainly single crystalline (ferromagnetic) α-Fe, has a diameter $d_{\mathrm{Fe}} = 39\,\mathrm{nm}$ and length $l_{\mathrm{Fe}} = 13.8\,\mu\mathrm{m}$. The CNT has a diameter of $\sim 130\,\mathrm{nm}$.

The FeCNT was positioned by a Kleindiek 3-axis manipulator inside a FIB-SEM combination onto SQUID-3, such that the distance between the left end of the Fe nanowire and the SQUID loop is $\sim 300\,\mathrm{nm}$ (cf. Fig. 4). We note that for optimum coupling of the stray field of the Fe nanowire into the SQUID, it is preferable to place the end of the Fe nanowire close to the edge of the SQUID loop opposite to the constriction. At this location, the coupling factor is slightly smaller than directly on top of the constriction, however, it does not fall off very rapidly upon moving further away from the loop, as it is the case near the constriction[31]. The Fe nanowire axis (its easy axis) was aligned as close as possible with the substrate plane [(x, y) plane], with an inclination angle $\theta \approx 4^\circ$ and perpendicular to the grain boundary, which is oriented along the y-axis. The inclination of the Fe wire axis with respect to the x-axis is $< 1^\circ$. The vertical distance (along the z-axis) between the nanowire axis (at its left end) and the surface of the YBCO film is $\approx 300\,\mathrm{nm}$.

The measurements on the Fe nanowire were performed with the non-optimized SQUID-3. This device has a significantly larger inductance (due to its smaller film thickness) and much smaller characteristic voltage, resulting in a much smaller transfer function $V_\Phi = 0.65\,\mathrm{mV}/\Phi_0$, as compared to SQUID-1 and -2. Magnetization reversal measurements on the FeCNT were performed with

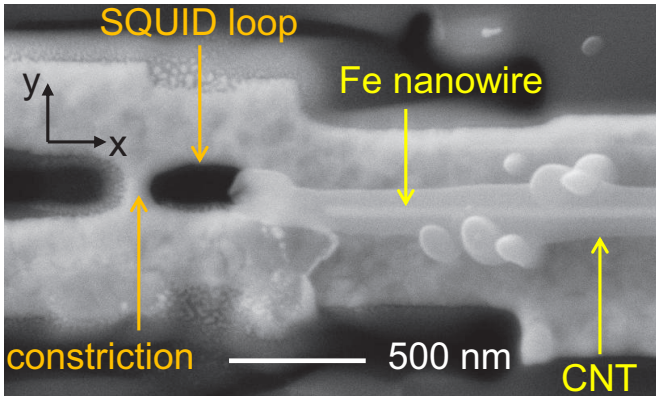

FIG. 4: (Color online) SEM image of SQUID-3 with Fe-wire filled carbon nanotube positioned close to the SQUID loop.

SQUID-3 operated in FLL dc bias mode up to $f = 190\,\mathrm{kHz}$. At this frequency, the noise was limited by the readout electronics, which yields for SQUID-3 an upper limit of the white rms flux noise $S_{\Phi,\mathrm{w}}^{1/2} \leq 1.45\,\mu\Phi_0/\mathrm{Hz}^{1/2}$. Below $\sim 40\,\mathrm{kHz}$, SQUID-3 showed f-dependent excess noise with $S_\Phi^{1/2} \approx 8\,\mu\Phi_0/\mathrm{Hz}^{1/2}$ at $f = 100\,\mathrm{Hz}$ and $S_\Phi^{1/2} \approx 20\,\mu\Phi_0/\mathrm{Hz}^{1/2}$ at $f = 10\,\mathrm{Hz}$, with an approximately $1/f^2$ increase of S_Φ below 10 Hz. Some experimentally determined parameters of SQUID-3 are listed in Tab. I. Details on low-field electric transport and noise characteristics of SQUID-3 are presented in Sec. II of the Supplemental Material[36].

For magnetization reversal measurements of the Fe nanowire on top of SQUID-3, the sample was mounted in a high-field setup, which allows to apply magnetic fields up to $\mu_0 H = 7\,\mathrm{T}$[31]. To minimize coupling of the external magnetic field H into the SQUID, the SQUID loop (in the (x, y) plane) has been aligned parallel to the field. To minimize coupling of the external field into the GB-JJs, the grain boundary (along the y-axis) was aligned perpendicular to the applied field. The alignment of the SQUID with respect to the applied field direction was performed by an Attocube system including two goniometers with perpendicular tilt axes and one rotator. In this configuration, the external field H is applied along the x-axis (cf. Fig. 4), and the angle between H and the Fe nanowire axis is given by θ.

Figure 5 shows the flux signal $\Phi(H)$ detected by SQUID-3, while sweeping H, at a rate $\mu_0 \partial H/\partial t \approx 1\,\mathrm{mT/s}$. At the fields $\pm\mu_0 H_\mathrm{n} = \pm 101\,\mathrm{mT}$, abrupt changes by $\Delta\Phi \approx 150\,\mathrm{m}\Phi_0$ clearly indicate magnetization reversal of the Fe nanowire. The shape of the $\Phi(H)$ curve indicates magnetization reversal of a single

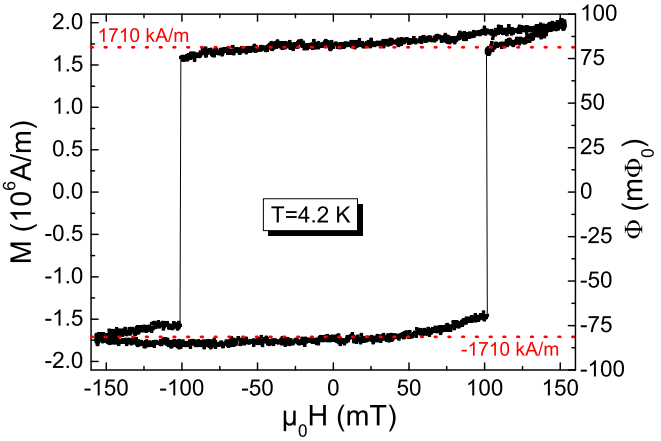

FIG. 5: (Color online) Hysteresis loop $\Phi(H)$ of the Fe-nanowire detected with SQUID-3 (operated in FLL dc bias mode with cutoff frequency $\sim 190\,\mathrm{kHz}$, at optimum working point with $V_\Phi = 0.65\,\mathrm{mV}/\Phi_0$). Switching of the magnetization occurs at $\pm\mu_0 H_\mathrm{n} = \pm 101\,\mathrm{mT}$. The residual field $\mu_0 H_\mathrm{res} = 4.0\,\mathrm{mT}$ was subtracted. Left axis indicates corresponding magnetization $M = \Phi/\phi_M$; the dashed lines indicate the literature value of the saturation magnetization $\pm M_\mathrm{s}$.

domain particle. The slope of the curve in the interval $-H_n \leq H \leq H_n$ depends strongly on the alignment of the SQUID with respect to the applied field. Hence, this slope can be attributed, at least partially, to the coupling of the external field to the SQUID loop. The hysteresis in the signals for $|H| \gtrsim 100\,\mathrm{mT}$ is typically observed also for our SQUIDs measured in the high-field setup without MNPs coupled to them. Hence, this hysteresis is attributed to a spurious magnetization signal from our setup or from the above mentioned magnetic defects close to the nanoSQUID, rather than being generated by the nanowire.

In order to convert from magnetic flux detected by the SQUID to magnetization of the Fe nanowire, we follow the approach described in Ref. [59]. We numerically calculate the coupling factor $\phi_\mu(\hat{e}_\mu, \vec{r}_p)$ for a point-like MNP with orientation $\hat{e}_\mu$ of its magnetic moment at position $\vec{r}_p$ in the 3D space above the SQUID[32]. These simulations take explicitly into account the geometry of SQUID-3 and are based on London theory[60]. We then assume that the Fe nanowire is in its fully saturated state, with saturation magnetization M_s, with all moments oriented along the wire axis. The corresponding saturation flux coupled to the SQUID is denoted as Φ_s. The ratio Φ_s/M_s is obtained by integration of the coupling factor ϕ_μ over the volume V_{Fe} of the Fe wire, at its given position, determined from SEM images. This yields

$$\phi_M \equiv \frac{\Phi_s}{M_s} = \int_{V_{Fe}} \phi_\mu(\vec{r_p})\, dV = 47.6\, \frac{n\Phi_0}{Am^{-1}}\,. \qquad (1)$$

From this we calculate $\Phi_s = M_s\phi_M = 81.4\,m\Phi_0$, with $M_s = 1710\,kA/m$ taken from literature[61]. The comparison with the measured flux signals $\pm 82.5\,m\Phi_0$ at $H = 0$ shows very good agreement. The left axis in Fig. 5 shows the magnetization axis, scaled as $M = \Phi/\phi_M$, with the horizontal dotted lines indicating the literature value $M_s = \pm 1710\,kA/m$. Hence, the measured flux signals are also in quantitative agreement with the assumption that the Fe nanowire switches to a fully saturated single domain state.

In Ref. [57] it was shown for a similar FeCNT that the nucleation field H_n changes with θ in a way which is typical for nucleation of magnetization reversal via the curling mode[62] in ferromagnetic nanowires as opposed to uniform rotation of the magnetic moments in small enough MNPs as described by the Stoner-Wolfarth model[63]. For switching via curling mode one obtains for $\theta = 0$ the simple relation $H_n = M_s a/2$, with a negligible increase well below 1 % with $\theta = 4^\circ$[64]. Here, $a = 1.08\,(2\lambda_{ex}/d_{Fe})^2$, with the exchange length $\lambda_{ex} = \sqrt{4\pi A/(\mu_0 M_s^2)}$ and the exchange constant A[61]. For $d_{Fe} = 39\,nm$ and with $\lambda_{ex} = 5.8\,nm$[61], we obtain $a = 0.0955$, and with $M_s = 1710\,kA/m$ we obtain an estimate of the nucleation field $H_n = 103\,mT$, which is in very good agreement with the experimentally observed value.

Finally, we note that the SQUID measurement yields a noise amplitude of $\sim 1m\Phi_0$, which is two orders of magnitude smaller than the detected signal upon magnetization reversal. For comparison, measurements on a similar Fe nanowire by micro-Hall magnetometry yielded a noise amplitude which was about one order of magnitude below the switching signal[57]. This means that the use of our nanoSQUID improves the signal-to-noise ratio by about one order of magnitude.

V. CONCLUSIONS

In conclusion, we fabricated and investigated optimized YBCO nanoSQUIDs based on grain boundary Josephson junctions. For our best device, an upper limit for the white flux noise level $S_\Phi^{1/2} < 50\,n\Phi_0/Hz^{1/2}$ in magnetically shielded environment could be determined, which corresponds to a spin sensitivity $S_\mu^{1/2} \equiv S_\Phi^{1/2}/\Phi_\mu = 3.7\,\mu_B/Hz^{1/2}$ for a magnetic nanoparticle located 10 nm above the constriction in the SQUID loop. Here, the coupling factor ϕ_μ was determined by numerical simulations based on London theory, which takes the device geometry into account. An obvious drawback of YBCO grain boundary junction nanoSQUIDs is the frequency-dependent excess noise, which extends up to the MHz range for optimized devices with ultra-low flux noise in the white noise limit. To eliminate $1/f$ noise, a bias reversal scheme was applied, which only partially reduced the frequency-dependent excess noise. Hence, in addition to critical current fluctuations, spin noise which is possibly due to fluctuations of defect-induced magnetic moments in the $SrTiO_3$ substrate is a major issue, which has to be studied in more detail for further improvement of the nanoSQUID performance at low frequencies. Nevertheless, we demonstrated the suitability of the YBCO nanoSQUIDs as detectors for magnetic nanoparticles in moderate magnetic fields by measuring the magnetization reversal of an iron nanowire that was placed close to the SQUID loop. Switching of the magnetization was detected at $\mu_0 H \approx \pm 100\,mT$, which is in very good agreement with nucleation of magnetization reversal via curling mode.

Acknowledgments

T. Schwarz acknowledges support by the Carl-Zeiss-Stiftung. M. J. Martínez-Pérez acknowledges support by the Alexander von Humboldt Foundation. We gratefully acknowledge fruitful discussions with D. Drung. This work was supported by the Nachwuchswissenschaftlerprogramm of the Universität Tübingen, by the Deutsche Forschungsgemeinschaft (DFG) via projects KO 1303/13-1, MU 1794/3-2 and SFB/TRR 21 C2 and by the EU-FP6-COST Action MP1201.

[1] J. Bartolomé, F. Luis, and J. F. Fernández, eds., Molecular Magnets: Physics and Applications, NanoScience and Technology (Springer, Heidelberg, 2014).

[2] L. Bogani and W. Wernsdorfer, Nature Materials **7**, 179 (2008).

[3] M. N. Leuenberger and D. Loss, Nature **410**, 789 (2001).

[4] S. Odenbach (ed.), J. Phys: Condens. Matter **18 (38)**, special issue (2006).

[5] A. Jordan, R. Scholz, P. Wust, H. Fähling, and R. Felix, J. Magn. Magn. Mat. **201**, 413 (1999).

[6] R. C. Semelka and T. K. G. Helmberger, Radiology **218**, 27 (2001).

[7] R. Klingeler, S. Hampel, and B. Büchner, Int. J. Hyperthermia **24**, 496 (2008).

[8] W. Wernsdorfer, Adv. Chem. Phys. **118**, 99 (2001).

[9] D. D. Awschalom, J. R. Rozen, M. B. Ketchen, W. J. Gallagher, A. W. Kleinsasser, R. L. Sandstrom, and B. Bumble, Appl. Phys. Lett. **53**, 2108 (1988).

[10] M. Ketchen, D. Awschalom, W. Gallagher, A. Kleinsasser, R. Sandstrom, J. Rozen, and B. Bumble, IEEE Trans. Magn. **25**, 1212 (1989).

[11] K. Hasselbach, D. Mailly, and J. R. Kirtley, J. Appl. Phys. **91**, 4432 (2002).

[12] S. K. H. Lam and D. L. Tilbrook, Appl. Phys. Lett. **82**, 1078 (2003).

[13] J.-P. Cleuziou, W. Wernsdorfer, V. Bouchiat, T. Ondarçuhu, and M. Monthioux, Nature Nanotech. **1**, 53 (2006).

[14] A. G. P. Troeman, H. Derking, B. Borger, J. Pleikies, D. Veldhuis, and H. Hilgenkamp, Nano Lett. **7**, 2152 (2007).

[15] N. C. Koshnick, M. E. Huber, J. A. Bert, C. W. Hicks, J. Large, H. Edwards, and K. A. Moler, Appl. Phys. Lett. **93**, 243101 (2008).

[16] L. Hao, J. C. Macfarlane, J. C. Gallop, D. Cox, J. Beyer, D. Drung, and T. Schurig, Appl. Phys. Lett. **92**, 192507 (2008).

[17] C. P. Foley and H. Hilgenkamp, Supercond. Sci. Technol. **22**, 064001 (2009).

[18] V. Bouchiat, Supercond. Sci. Technol. **22**, 064002 (2009).

[19] W. Wernsdorfer, Supercond. Sci. Technol. **22**, 064013 (2009).

[20] F. Giazotto, J. T. Peltonen, M. Meschke, and J. P. Pekola, Nature Phys. **6**, 254 (2010).

[21] M. J. Martínez-Pérez, E. Bellido, R. de Miguel, J. Sesé, A. Lostao, C. Gómez-Moreno, D. Drung, T. Schurig, D. Ruiz-Molina, and F. Luis, Appl. Phys. Lett. **99**, 032504 (2011).

[22] E. J. Romans, S. Rozhko, L. Young, A. Blois, L. Hao, D. Cox, and J. C. Gallop, IEEE Trans. Appl. Supercond. **21**, 404 (2011).

[23] R. Russo, C. Granata, E. Esposito, D. Peddis, C. Cannas, and A. Vettoliere, Appl. Phys. Lett. **101**, 122601 (2012).

[24] C. Granata, A. Vettoliere, R. Russo, M. Fretto, N. D. Leo, and V. Lacquaniti, Appl. Phys. Lett. **103**, 102602 (2013).

[25] D. Drung, J.-H. Storm, F. Ruede, A. Kirste, M. Regin, T. Schurig, A. M. Repollés, J. Sesé, and F. Luis, IEEE Trans. Appl. Supercond. **24**, 1600206 (2014).

[26] A. Finkler, Y. Segev, Y. Myasoedov, M. L. Rappaport, L. Ne'eman, D. Vasyukov, E. Zeldov, M. E. Huber, J. Martin, and A. Yacoby, Nano Lett. **10**, 1046 (2010).

[27] R. Arpaia, M. Arzeo, S. Nawaz, S. Charpentier, F. Lombardi, and T. Bauch, App. Phys. Lett. **104**, 072603 (2014).

[28] D. Vasyukov, Y. Anahory, L. Embon, D. Halbertal, J. Cuppens, L. Ne'eman, A. Finkler, Y. Segev, Y. Myasoedov, M. L. Rappaport, et al., Nature Nanotechnol. **8**, 639 (2013).

[29] L. Chen, W. Wernsdorfer, C. Lampropoulos, G. Christou, and I. Chiorescu, Nanotechnology **21**, 405504 (2010).

[30] J. Nagel, K. B. Konovalenko, M. Kemmler, M. Turad, R. Werner, E. Kleisz, S. Menzel, R. Klingeler, B. Büchner, R. Kleiner, et al., Supercond. Sci. Technol. **24**, 015015 (2011).

[31] T. Schwarz, J. Nagel, R. Wölbing, M. Kemmler, R. Kleiner, and D. Koelle, ACS Nano **7**, 844 (2013).

[32] R. Wölbing, T. Schwarz, B. Müller, J. Nagel, M. Kemmler, R. Kleiner, and D. Koelle, Supercond. Sci. Technol., in press (2014), arXiv:1301.1189v2 [cond-mat.supr-con].

[33] D. Drung and M. Mück, SQUID Electronics (Wiley-VCH, Weinheim, 2004), vol. 1: Fundamentals and Technology of SQUIDs and SQUID systems, chap. 4, pp. 127–170.

[34] SQUID electronics SEL-1 from Magnicon GmbH, Lemsahler Landstr. 171, D-22397 Hamburg, Germany; http://www.magnicon.com.

[35] D. Drung, Supercond. Sci. Technol. **16**, 1320 (2003).

[36] See Supplemental Material at http://link.aps.org/ supplemental/10.1103/PhysRevApplied.x.yyyyyy for additional data and analysis of SQUID-1, -2 and -3.

[37] B. Chesca, R. Kleiner, and D. Koelle, SQUID Theory (Wiley-VCH, Weinheim, 2004), vol. 1: Fundamentals and Technology of SQUIDs and SQUID systems, chap. 2, pp. 29–92.

[38] D. Koelle, R. Kleiner, F. Ludwig, E. Dantsker, and J. Clarke, Rev. Mod. Phys. **71**, 631 (1999).

[39] E. Sassier, R. Kleiner, and D. Koelle, unpublished.

[40] D. J. Van Harlingen, R. H. Koch, and J. Clarke, Appl. Phys. Lett. **41**, 197 (1982).

[41] E. M. Levenson-Falk, R. Vijay, N. Antler, and I. Siddiqi, Supercond. Sci. Technol. **26**, 005015 (2013).

[42] From measurements on a similar device we found an almost linear decrease in I_c with time, with a $\sim 20\,\%$ reduction in I_c after 40 days. This rate of degradation is typical for most of our devices. A possible explanation of this effect is outdiffusion of oxygen from the submicron GBJJs along the $a-b$ plane of the YBCO thin film.

[43] G. Stan, S. B. Field, and J. M. Martinis, Phys. Rev. Lett. **92**, 097003 (2004).

[44] F. C. Wellstood, C. Urbina, and J. Clarke, App. Phys. Lett. **50**, 772 (1987).

[45] D. Drung, J. Beyer, J.-H. Storm, M. Peters, and T. Schurig, IEEE Trans. Appl. Supercond. **21**, 340 (2011).

[46] R. H. Koch, D. P. DiVincenzo, and J. Clarke, Phys. Rev. Lett. **98**, 267003 (2007).

[47] R. de Sousa, Phys. Rev. B **76**, 245306 (2007).

[48] S. Sendelbach, D. Hover, A. Kittel, M. Mück, J. M. Martinis, and R. McDermott, Phys. Rev. Lett. **100**, 227006 (2008).

[49] M. Venkatesan, C. B. Fitzgerald, and J. M. D. Coey, Nature **430**, 630 (2004).

[50] N. Pavlenko, T. Kopp, E. Y. Tsymbal, J. Mannhart, and G. A. Sawatzky, Phys. Rev. B **86**, 064431 (2012).

[51] J. M. D. Coey, Ariando, and W. E. Pickett, MRS Bulletin **38**, 1040 (2013).
[52] I. R. Shein and A. L. Ivanosvkii, Phys. Lett. A **371**, 155 (2007).
[53] M. Khalid, A. Setzer, M. Ziese, P. Esquinazi, D. Spemann, A. Pöppl, and E. Goering, Phys. Rev. B **81**, 214414 (2010).
[54] K. Potzger, J.Osten, A. A.Levin, A.Shalimov, G.Talut, H.Reuther, S.Arpaci, D. Bürger, H. Schmidt, T.Nestler, et al., J. Magn. Magn. Mater. **323**, 1551 (2011).
[55] B. B. Straumal, A. A. Mazilkin, S. G. Protasova, A. A. Myatiev, P. B. Straumal, G. Schütz, P. A. van Aken, E. Goering, and B. Baretzky, Phys. Rev. B **79**, 205206 (2009).
[56] A. Leonhardt, S. Hampel, C. Müller, I. Mönch, R. Koseva, M. Ritschel, D. Elefant, K. Biedermann, and B. Büchner, Chem. Vap. Deposition **12**, 380 (2006).
[57] K. Lipert, S. Bahr, F. Wolny, P. Atkinson, U. Weißker, T. Mühl, O. G. Schmidt, B. Büchner, and R. Klingeler, App. Phys. Lett. **97**, 212503 (2010).
[58] T. Mühl, J. Körner, S. Philippi, C. F. Reiche, A. Leonhardt, and B. Büchner, App. Phys. Lett. **101**, 112401 (2012).
[59] J. Nagel, A. Buchter, F. Xue, O. F. Kieler, T. Weimann, J. Kohlmann, A. B. Zorin, D. Rüffer, E. Russo-Averchi, R. Huber, et al., Phys. Rev. B **88**, 064425 (2013).
[60] M. Khapaev, M. Kupriyanov, E. Goldobin, and M. Siegel, Supercond. Sci. Technol. **16**, 24 (2003).
[61] M. E. Schabes, J. Magn. Magn. Mater. **95**, 249 (1991).
[62] A. Aharoni, Phys. Stat. Sol. **16**, 3 (1966).
[63] R. Skomski, Simple Models of Magnetism (Oxford University Press, New York, 2008).
[64] A. Aharoni, J. Appl. Phys. **82**, 1281 (1997).

Supplementary Information for Low-Noise $YBa_2Cu_3O_7$ Nano Superconducting Quantum Interference Devices for Magnetization Reversal Measurements on Magnetic Nanoparticles

T. Schwarz,[1] R. Wölbing,[1] C. F. Reiche,[2] B. Müller,[1]
M. J. Martínez-Pérez,[1] T. Mühl,[2] B. Büchner,[2] R. Kleiner,[1] and D. Koelle[1]

[1] *Physikalisches Institut – Experimentalphysik II and Center for Collective Quantum Phenomena in LISA+, Universität Tübingen, Auf der Morgenstelle 14, D-72076 Tübingen, Germany*
[2] *Leibniz Institute for Solid State and Materials Research IFW Dresden, Helmholtzstr. 20, 01069 Dresden, Germany*

(Dated: September 30, 2014)

I. CHARACTERIZATION OF SQUID-2

SQUID-2 was characterized in an electrically and magnetically shielded setup, with the sample mounted in vacuum (or in He gas) on a temperature-controlled cryostage. This enabled us to characterize electric transport and noise properties at variable temperature T, with a T stability of $\sim 1\,\mathrm{mK}$ [1].

Figure 1 shows data of electric transport properties and flux noise of SQUID-2, measured at $T = 5.3\,\mathrm{K}$. Figure 1(a) shows current-voltage-characteristics (IVCs) for modulation current $I_{\mathrm{mod}} = 0$ and two values of I_{mod}, corresponding to maximum and minimum critical current. The IVCs are slightly hysteretic with maximum critical current $I_{\mathrm{c}} = 311\,\mu\mathrm{A}$ and normal state resistance $R_{\mathrm{N}} = 2.5\,\Omega$, which yields a characteristic voltage $V_{\mathrm{c}} \equiv I_{\mathrm{c}}R_{\mathrm{N}} = 0.78\,\mathrm{mV}$. The inset of Fig. 1(a) shows the modulation of the critical current $I_{\mathrm{c}}(I_{\mathrm{mod}})$. From the modulation period, we find for the magnetic flux Φ coupled to the SQUID by I_{mod} the mutual inductance $M = \Phi/I_{\mathrm{mod}} = 0.8\,\Phi_0/\mathrm{mA} = 1.66\,\mathrm{pH}$. From resistively and capacitively shunted junction (RCSJ) simulations [2] of the $I_{\mathrm{c}}(I_{\mathrm{mod}})$ characteristics [cf. inset of Fig. 1(a)] we obtain for the screening parameter $\beta_L = 2I_0L/\Phi_0 = 0.94$ (with $I_0 = I_{\mathrm{c}}/2$), which yields a SQUID inductance $L = 6.3\,\mathrm{pH}$. We do find good agreement between the measured and simulated $I_{\mathrm{c}}(I_{\mathrm{mod}})$ characteristics if we include an inductance asymmetry $\alpha_L \equiv (L_2 - L_1)/(L_2 + L_1) = 0.83$ (L_1 and L_2 are the inductances of the two SQUID arms) and a critical current asymmetry $\alpha_I \equiv (I_{0,2} - I_{0,1})/(I_{0,2} + I_{0,1}) = 0.30$; $I_{0,1}$ and $I_{0,2}$ are the critical currents of the Josephson junctions 1 and 2, respectively, intersecting the SQUID loop. These asymmetries are caused by asymmetric biasing of the SQUID and by asymmetries of the device itself.

$V(I_{\mathrm{mod}})$ is plotted in Fig. 1(b) for different bias currents. The transfer function, i.e. the maximum value of $\partial V/\partial\Phi$, in the non-hysteretic regime is $V_\Phi \approx 1.7\,\mathrm{mV}/\Phi_0$.

Fig. 1(c) shows the rms spectral density of flux noise $S_\Phi^{1/2}(f)$ of SQUID-2. This measurement was performed open loop (in dc bias mode) with a Nb dc SQUID (at $T = 4.2\,K$) as a voltage preamplifier, i.e. in 2-stage configuration, with a $\sim 700\,\mathrm{kHz}$ bandwidth. As for SQUID-1 (see main text), we find dominating f-dependent noise, with a noise power which scales very roughly as $S_\Phi \propto 1/f$.

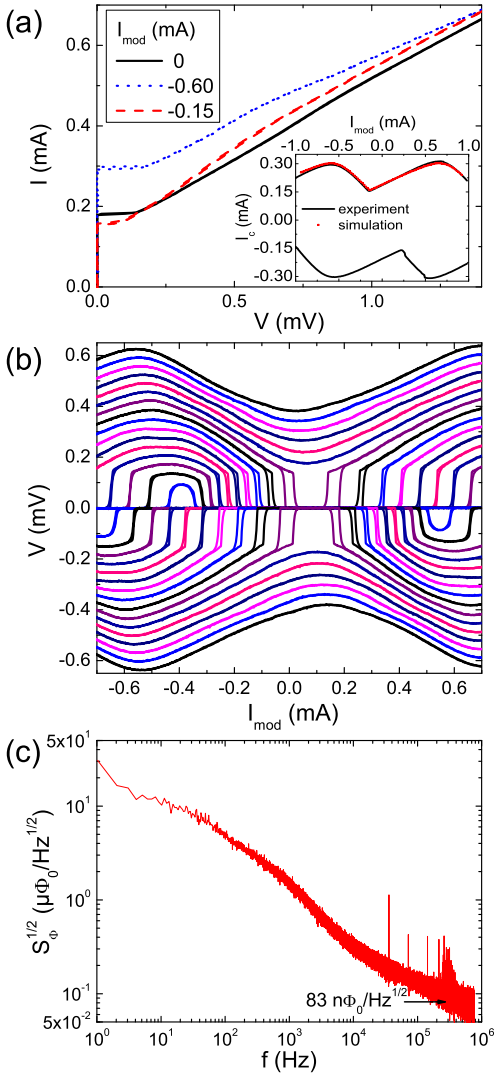

FIG. 1: Characteristics of SQUID-2 at $T = 5.3\,\mathrm{K}$. (a) IVCs for three different values of I_{mod}, including flux bias (I_{mod}) values which yield maximum and minimum critical current. Inset: measured $I_{\mathrm{c}}(I_{\mathrm{mod}})$ together with numerical simulation results. (b) $V(I_{\mathrm{mod}})$ for bias currents $|I| = 175\ldots400\,\mu\mathrm{A}$ (in $15\,\mu\mathrm{A}$ steps). (c) rms spectral density of flux noise, measured open loop (dc bias) in 2-stage configuration. Arrow indicates upper limit for measured white noise at $\sim 700\,\mathrm{kHz}$.

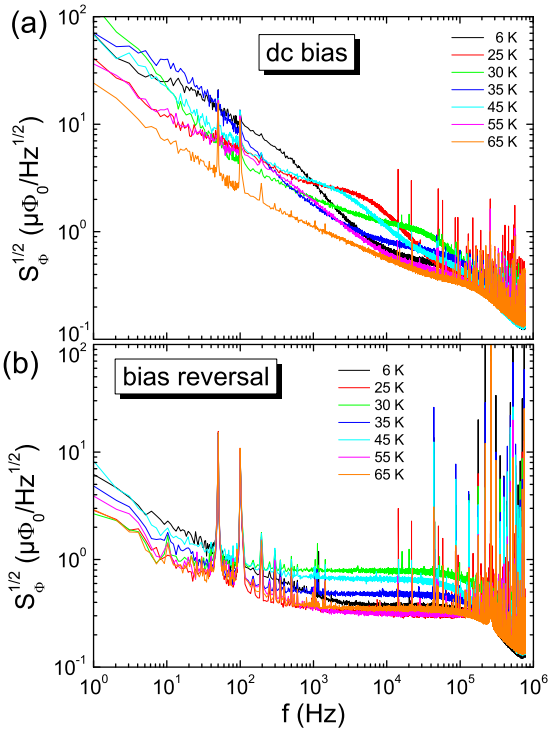

FIG. 2: rms spectral density of flux noise for SQUID-2, measured in FLL mode at different temperatures from 6 K to 65 K. (a) dc bias mode (b) bias reversal mode ($f_{\rm br} = 260\,$kHz).

Figure 2 shows rms flux noise spectra of SQUID-2 measured with direct readout in flux locked loop (FLL), with $\sim 500\,$kHz bandwidth, in dc bias and bias reversal mode [3] for temperatures T ranging from 6 K to 65 K. For all data measured with dc bias [cf. Fig. 2(a)], we find f-dependent excess noise up to the cutoff frequency of the readout electronics. The flux noise S_Φ scales roughly as $1/f$, and for different T, the rms flux noise does not differ by more than about a factor of five, and does not show any systematic T-dependence.

Similar to SQUID-1 (cf. main text), in bias reversal mode [cf. Fig. 2(b)] the f-dependent excess noise above $\sim 1\,$kHz is suppressed. The remaining low-f excess flux noise observed in bias reversal mode roughly scales as $S_\Phi \propto 1/f$ for all values of T, again without any systematic T-dependence.

II. CHARACTERIZATION OF SQUID-3

Figure 3 shows electric transport and flux noise data for SQUID-3, taken in the magnetically and electrically shielded low-field setup at $T = 4.2\,$K, as described in the main text. The IVC shown in Fig. 3(a) is non-hysteretic, with $I_{\rm c} = 69\,\mu$A and $R_{\rm N} = 2.3\,\Omega$, which yields $V_{\rm c} = 0.16\,$mV. The inset shows $I_{\rm c}(I_{\rm mod})$, from which we obtain the mutual inductance $M = \Phi/I_{\rm mod} = 3.3\,\Phi_0/$mA. From the modulation depth of $I_{\rm c}(I_{\rm mod})$ we determine $\beta_L = 0.95$. With the measured $I_{\rm c}$, this yields a SQUID inductance $L = 28\,$pH. The bumps in the IVC at $V_{\rm res} \approx \pm 0.28\,$mV, can be attributed to an LC resonance. From the relation $V_{\rm res}/I_{\rm c}R_{\rm N} = (\frac{\pi}{2}\beta_C\beta_L)^{-1/2}$ [2] we determine the Stewart-McCumber parameter for the GBJJs as $\beta_C \approx 0.22$.

Figure 3(b) shows $V(I_{\rm mod})$ curves for different bias currents, yielding a transfer function $V_\Phi = 0.65\,{\rm mV}/\Phi_0$ at the optimum bias point, at which noise spectra have been taken ($I = 54\,\mu$A). Figure 3(c) shows the rms spectral density of flux noise $S_\Phi^{1/2}(f)$ for SQUID-3, measured in direct readout FLL mode up to $f = 100\,$kHz. For com-

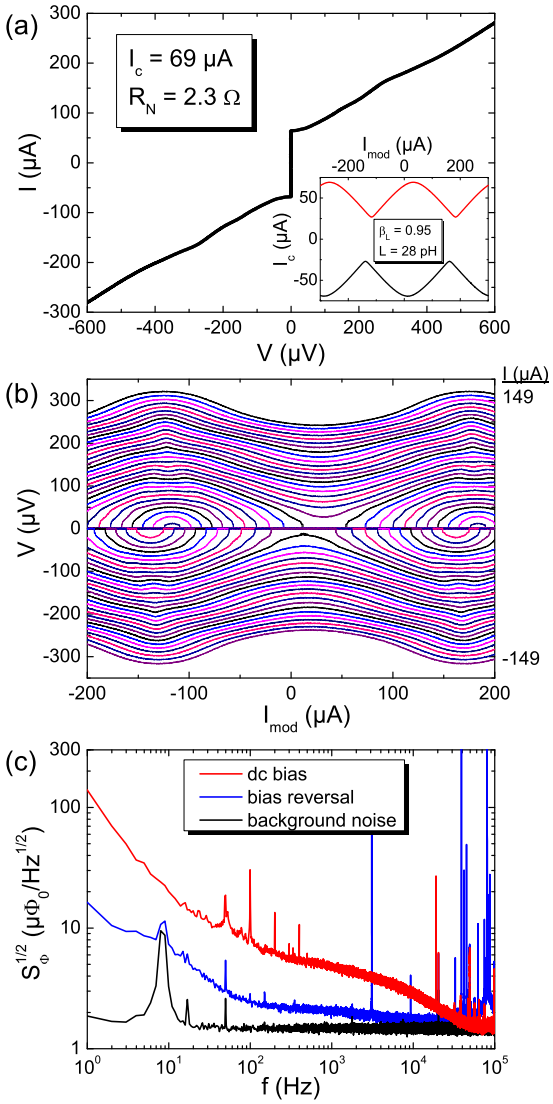

FIG. 3: Electric transport and noise characteristics of SQUID-3. (a) IVC of SQUID-3 for flux bias ($I_{\rm mod}$) which yields maximum critical current. Inset shows $I_{\rm c}(I_{\rm mod})$ curves for positive and negative current bias. (b) Voltage V vs modulation current $I_{\rm mod}$ for bias currents between $I = \pm 149\,\mu$A (step width $\Delta I \approx 4\,\mu$A). (c) Rms spectral density of flux noise measured in FLL with dc bias and bias reversal mode ($f_{\rm br} = 260\,$kHz). The lower trace shows the background noise of the readout electronics.

parison, the bottom trace shows the background noise from the readout electronics $S_\Phi^{1/2} \approx 1.45\,\mu\Phi_0/\mathrm{Hz}^{1/2}$. For $f \lesssim 40\,\mathrm{kHz}$, we find f-dependent flux noise. For larger f, the noise is limited by the electronics background noise. Hence, we can only give an upper limit of the white rms flux noise of SQUID-3 as $S_{\Phi,\mathrm{w}}^{1/2} < 1.45\,\mu\Phi_0/\mathrm{Hz}^{1/2}$. With bias reversal (at $f_\mathrm{br} = 81\,\mathrm{kHz}$), the f-dependent excess noise is clearly reduced. Still, we obtain with decreasing f a slight increase in rms flux noise up to $\sim 2.4\,\mu\Phi_0/\mathrm{Hz}^{1/2}$ at 100 Hz. Below 100 Hz SQUID-3 shows approximately $1/f$ noise, i.e. an increase in $S_\Phi^{1/2}$ to $\sim 16\,\mu\Phi_0/\mathrm{Hz}^{1/2}$ at 1 Hz.

III. ANALYSIS OF NOISE SPECTRA OF SQUID-1

For a more detailed analysis of the measured spectral density of equivalent flux noise power $S_\Phi(f)$ for SQUID-1, we applied an algorithm [4] to decompose the noise spectra into a sum of Lorentzians $F_i(f) = F_{0,i}/[1 + (f/f_{\mathrm{c},i})^2]$ plus a $1/f^2$ spectrum $F_\mathrm{s}(f) = F_\mathrm{s}(1\,\mathrm{Hz})/(f^2/\mathrm{Hz}^2)$ (i.e. one or more Lorentzians with characteristic frequencies f_c well below 1 Hz) plus a white noise contribution F_w. This means, the measured spectra are fitted by $F(f) = F_\mathrm{w} + F_\mathrm{s} + \sum_i F_i$

Figure 4 shows the fit $F_\mathrm{op}^{1/2}(f)$ to the spectrum measured open loop (dc bias) [cf. Fig. 3(a) in the main text.]. This yields an rms white noise level $F_{\mathrm{w,op}}^{1/2} = 45\,\mathrm{n}\Phi_0/\mathrm{Hz}^{1/2}$, a 1 Hz noise $F_{\mathrm{s,op}}^{1/2} = 84\,\mu\Phi_0/\mathrm{Hz}^{1/2}$ from $F_{\mathrm{s,op}}$ plus 16 Lorentzians with characteristic frequencies $f_{\mathrm{c},i}$, ranging from 2.6 Hz to 2.6 MHz, and amplitudes $F_{0,i}^{1/2}$ as listed in Tab. I(a). For comparison of the fluctuation strengths of the different fluctuators with different

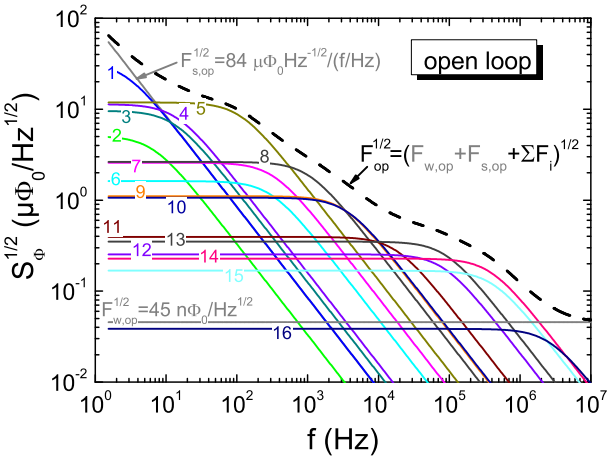

FIG. 4: Analysis of flux noise of SQUID-1: The dashed line is the fit to the noise spectrum, measured open loop (dc bias). This spectrum is the sum of the shown Lorentzians (labeled as $i = 1 \ldots 16$) plus a white noise contribution plus a $F_s \propto 1/f^2$ contribution.

$f_{\mathrm{c},i}$, in Tab. I we also list $\Delta\Phi_i = F_{0,i}^{1/2} \cdot \sqrt{2\pi f_{\mathrm{c},i}}$, which yields values in the range $\sim 30 \ldots 350\,\mu\Phi_0$.

Figure 5(a) and (b) shows the fits $F_\mathrm{dc}^{1/2}(f)$ and $F_\mathrm{br}^{1/2}(f)$ to the spectra measured in FLL with dc bias and bias reversal, respectively [cf. Fig. 3(b) in the main text.]. Here, we fixed the white noise contribution in dc bias mode to $F_{\mathrm{w,dc}}^{1/2} = 41\,\mathrm{n}\Phi_0/\mathrm{Hz}^{1/2}$, i.e. a value close to the one obtained for the measurement in open loop mode. The white noise contribution in bias reversal mode is determined by the noise level achieved in dc bias mode at the bias reversal frequency f_br, which yields $F_{\mathrm{w,br}}^{1/2} = 231\,\mathrm{n}\Phi_0/\mathrm{Hz}^{1/2}$. The spectrum fitted to the dc bias measurement is decomposed into 15 Lorentzians, while for the bias reversal measurement, fitting with 6 Lorentzians is sufficient. The rms noise at 1 Hz for the bias reversal spectrum is by a factor ~ 1.8 lower than the one for the dc bias spectrum. Characteristic frequencies $f_{\mathrm{c},i}$, and amplitudes of the Lorentzians are listed in Tab. I(b) for the dc bias spectrum and in Tab. I(c) for the bias reversal spectrum.

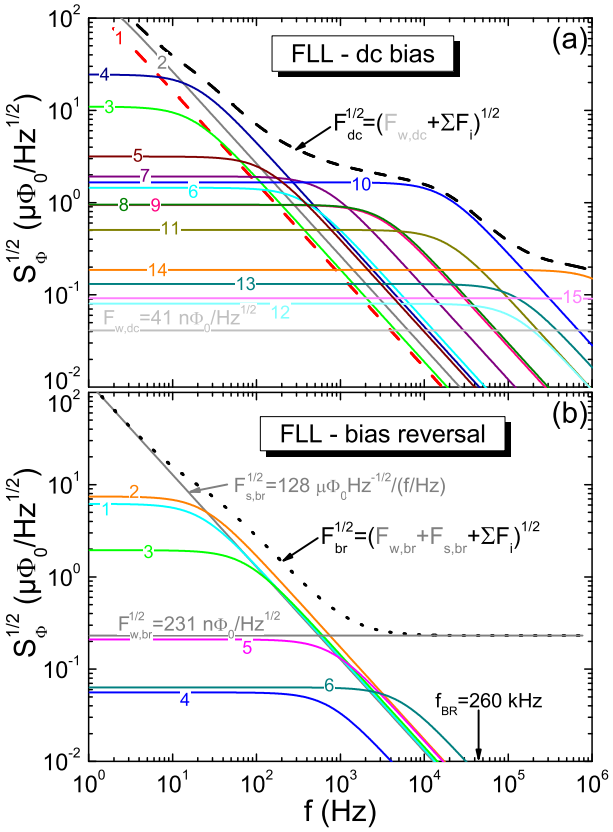

FIG. 5: Analysis of flux noise of SQUID-1: The dashed line in (a) and the dotted line in (b) are fits to the noise spectra, measured in FLL (a) with dc bias and (b) with bias reversal. Those spectra are superpositions of the shown Lorentzians [labeled as $i = 1 \ldots 11$ in (a) and $i = 1 \ldots 6$ in (b)] plus a white noise contribution plus a $F_s \propto 1/f^2$ contribution.

TABLE I: Characteristic frequencies $f_{c,i}$, rms amplitudes $F_{0,i}^{1/2}$ and flux amplitudes $\Delta\Phi_i$ of Lorentzians F_i calculated to approximate the flux noise spectra of SQUID-1, measured (a) in open loop (dc bias) [cf. Fig. 4], (b) in FLL dc bias [cf. Fig. 5(a)], and (c) in FLL bias reversal mode [cf. Fig. 5(b)].

(a) open loop

i	1	2	3	4	5	6	7	8	9	10	11	12	13	14	15	16
$f_{c,i}$ (Hz)	2.6	6.5	13	14	111	301	325	1.0 k	3.3 k	3.5 k	18 k	82 k	88 k	380 k	410 k	2.6 M
$F_{0,i}^{1/2}$ ($\mu\Phi_0$/Hz$^{1/2}$)	33	5.1	9.6	11	12	1.6	2.6	2.6	1.1	1.1	0.40	0.25	0.35	0.23	0.17	0.038
$\Delta\Phi_i$ ($\mu\Phi_0$)	131	32	87	106	314	71	119	211	158	158	131	182	261	352	269	155

(b) FLL – dc bias

i	1	2	3	4	5	6	7	8	9	10	11	12	13	14	15
$f_{c,i}$ (Hz)	0.8	1	17	18	126	369	631	2.9 k	3.2 k	17.1 k	18.5 k	117 k	126 k	1.4 M	6.8 M
$F_{0,i}^{1/2}$ ($\mu\Phi_0$/Hz$^{1/2}$)	206	265	11.0	24.5	3.2	1.4	1.9	0.94	0.95	1.7	0.51	0.08	0.13	0.19	0.09
$\Delta\Phi_i$ ($\mu\Phi_0$)	461	665	114	264	89	70	121	128	134	544	173	69	117	546	600

(c) FLL – bias reversal

i	1	2	3	4	5	6
$f_{c,i}$ (Hz)	21	23	74	736	794	5 k
$F_{0,i}^{1/2}$ ($\mu\Phi_0$/Hz$^{1/2}$)	6.2	7.4	1.9	0.056	0.21	0.063
$\Delta\Phi_i$ ($\mu\Phi_0$)	72	90	42	3.8	15	11

[1] M. Kemmler, D. Bothner, K. Ilin, M. Siegel, R. Kleiner, and D. Koelle, Phys. Rev. B **79**, 184509 (2009).

[2] B. Chesca, R. Kleiner, and D. Koelle, SQUID Theory (Wiley-VCH, Weinheim, 2004), vol. 1: Fundamentals and Technology of SQUIDs and SQUID systems, chap. 2, pp. 29–92.

[3] D. Drung and M. Mück, SQUID Electronics (Wiley-VCH, Weinheim, 2004), vol. 1: Fundamentals and Technology of SQUIDs and SQUID systems, chap. 4, pp. 127–170.

[4] E. Sassier, R. Kleiner, and D. Koelle, unpublished.

Publication 4

Nb nano superconducting quantum interference devices with high spin sensitivity for operation in magnetic fields up to 0.5 T

R. Wölbing,[1] J. Nagel,[1] T. Schwarz,[1] O. Kieler,[2] T. Weimann,[2] J. Kohlmann,[2] A. B. Zorin,[2] M. Kemmler,[1] R. Kleiner,[1] and D. Koelle[1]
[1]*Physikalisches Institut – Experimentalphysik II and Center for Collective Quantum Phenomena in LISA*$^+$, *Universität Tübingen, Auf der Morgenstelle 14, D-72076 Tübingen, Germany*
[2]*Fachbereich 2.4 "Quantenelektronik," Physikalisch-Technische Bundesanstalt, Bundesallee 100, D-38116 Braunschweig, Germany*

(Received 10 April 2013; accepted 27 April 2013; published online 14 May 2013)

We investigate electric transport and noise properties of microstrip-type submicron direct current superconducting quantum interference devices (dc SQUIDs) based on Nb thin films and overdamped Josephson junctions with a HfTi barrier. The SQUIDs were designed for optimal spin sensitivity $S_\mu^{1/2}$ upon operation in intermediate magnetic fields B (tens of mT), applied perpendicular to the substrate plane. Our, so far, best SQUID can be continuously operated in fields up to $B \approx \pm 50\,\mathrm{mT}$ with rms flux noise $S_{\Phi,\mathrm{w}}^{1/2} \leq 250\,\mathrm{n}\Phi_0/\mathrm{Hz}^{1/2}$ in the white noise regime and spin sensitivity $S_\mu^{1/2} \leq 29\,\mu_\mathrm{B}/\mathrm{Hz}^{1/2}$. Furthermore, we demonstrate operation in $B = 0.5\,\mathrm{T}$ with high sensitivity in flux $S_{\Phi,\mathrm{w}}^{1/2} \approx 680\,\mathrm{n}\Phi_0/\mathrm{Hz}^{1/2}$ and in electron spin $S_\mu^{1/2} \approx 79\,\mu_\mathrm{B}/\mathrm{Hz}^{1/2}$. We discuss strategies to further improve the nanoSQUID performance. © *2013 AIP Publishing LLC*. [http://dx.doi.org/10.1063/1.4804673]

Recent developments in miniaturized submicron-sized direct current (dc) superconducting quantum interference devices (SQUIDs) are motivated by the need of sensitive detectors for small spin systems such as molecular magnets[1–3] and magnetic nanoparticles,[4] cold atom clouds,[5] or single electrons and atoms[6] and improved resolution in scanning SQUID microscopy.[7–12] As a common approach, nanoSQUIDs based on constriction Josephson junctions (JJs) have been used,[13–19] achieving root mean square (rms) flux noise power $S_\Phi^{1/2}$ down to a few $100\,\mathrm{n}\Phi_0/\mathrm{Hz}^{1/2}$ (Φ_0 is the magnetic flux quantum) in magnetically shielded environment.[20] However, constriction JJs, even if resistively shunted, often show hysteretic current-voltage-characteristics (IVCs). This hampers continuous SQUID operation as required for the investigation of magnetization dynamics of magnetic particles and the use of common SQUID electronics, developed for readout of very sensitive dc SQUIDs with nonhysteretic JJs. Furthermore, the noise properties of constriction JJs are not well understood, which makes SQUID optimization difficult.

An alternative approach is the use of submicron superconductor-normal conductor-superconductor (SNS) sandwich-type JJs, which offer large critical current densities in the $10^5\,\mathrm{A/cm}^2$ range and which are intrinsically shunted, providing nonhysteretic IVCs without the need of bulky external shunt resistors.[21] In a standard thin film SQUID geometry, the SQUID loop and the JJ barrier are in the plane of the thin films. For detection of magnetization reversal of a small magnetic particle, one applies an external magnetic field in the plane of the SQUID loop and detects the change of the stray field coupled to the SQUID upon magnetization reversal, without coupling the external field to the SQUID. However, in this case, the applied field also couples magnetic flux into the JJ barrier and reduces its critical current, which in turn reduces the SQUID sensitivity. In order to avoid this problem, in this letter we present results on a modified SQUID design, which takes advantage of the multilayer technology used for SNS JJ fabrication. This approach allows for a further reduction of the SQUID inductance and hence improved SQUID sensitivity and at the same time operation in higher magnetic fields.

The Nb thin film dc SQUIDs have a microstrip geometry, i.e., the two 250 nm wide arms of the SQUID loop lie directly on top of each other. The 200 nm thick bottom and 160 nm thick top Nb layers are separated by a 225 nm thick insulating SiO_2 layer and are connected via two JJs with areas $200 \times 200\,\mathrm{nm}^2$ and a nominally 24 nm thick HfTi barrier (see Fig. 1). HfTi was chosen as a barrier material as, among other binary materials, it provides a relatively high resistivity, does not become superconducting at 4.2 K, and is compatible with our fabrication technology. For details on sample fabrication and JJ properties we refer to Refs. 21–23. The size of the SQUID loop is defined by the 1.6 μm spacing between the JJs and by the SiO_2 interlayer thickness. In contrast to earlier work,[21] for this geometry a sufficiently large magnetic field B can be applied perpendicular to the substrate plane without inducing a significant magnetic flux penetrating either the SQUID loop or the junction barrier. Furthermore, this design provides a very small area of the SQUID loop and hence a very small SQUID inductance L of a few pH or even lower. This is essential for reaching ultralow values for the spectral density of flux noise power S_Φ.[24]

For current and flux biasing, additional 250 nm wide Nb lines are connecting the SQUID in a cross-shape geometry, and a bias current I_b, flowing from the top Nb layer through the JJs to the bottom Nb layer, can be applied either in a symmetric or asymmetric configuration (see Fig. 1). For simplified readout we use asymmetric current bias in the following. A magnetic flux Φ can be coupled into the SQUID loop by applying a modulation current I_mod across the bottom Nb layer ("flux bias line"). This enables flux biasing the SQUIDs at the optimum working point without the need of

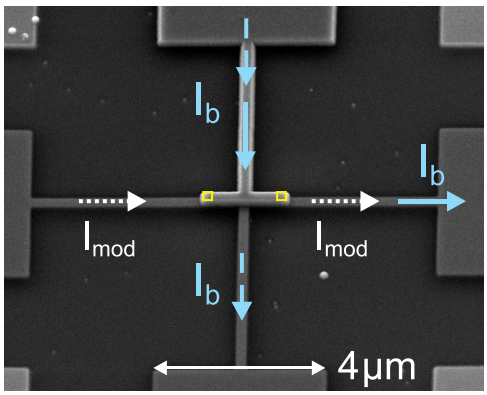

FIG. 1. Scanning electron microscopy (SEM) image of SQUID 2. Open (yellow) squares indicate positions of JJs. Arrows indicate current paths for bias current I_b (dashed: symmetric bias; solid: asymmetric bias) and modulation current I_{mod} (dotted).

an external coil. Furthermore, the flux bias line can also be used to provide a feedback flux for SQUID operation in a flux locked loop. However, in this work, the SQUIDs were always read out open loop.

We investigated various SQUIDs which were fabricated in two different runs on separate wafers. Below we present results for two devices, SQUID 1 from wafer 1 and SQUID 2 from wafer 2. The main difference in the design of these devices is the different lengths $\sim 2.5\,\mu$m (SQUID 1) and $\sim 5\,\mu$m (SQUID 2) of the narrow bias lines, running from the center of the SQUID to the $4\,\mu$m wide connection lines further away from the SQUID (cf., Fig. 1). This variation has a strong impact on the SQUID performance in applied magnetic fields, as will be shown below.

All data were taken at temperature $T = 4.2\,$K. We first present results of transport and noise measurements of the two SQUIDs in an electrically and magnetically shielded environment. Since both devices showed qualitatively the same behavior, we only give a detailed analysis of SQUID 2 and summarize the main parameters extracted for both devices in Table I. Regarding absolute values, a major difference between both devices are the values for maximum critical current I_c and normal resistance R_N, which probably is due to variations in the HfTi barrier thickness for the devices fabricated in different runs. Devices fabricated from the same run showed a spread in I_c and R_N values of $\pm 10\,\%$.

Figure 2(a) shows IVCs of SQUID 2 for $\Phi/\Phi_0 = 0$, 1/4, and 1/2. The IVCs are nonhysteretic with $I_c = 227\,\mu$A and $R_N = 250\,\text{m}\Omega$, yielding a characteristic voltage $V_c \equiv I_c R_N = 57\,\mu$V. The IVC at $\Phi/\Phi_0 = 1/2$ exhibits a small bump for low voltages. This bump appears in all our devices and is presumably a property of the quasiparticle current rather than a *LC* resonance of the SQUID. The inset of Fig. 2(a) shows the modulation $I_c(I_{mod})$ for positive and negative bias current.

TABLE I. Parameters of SQUID 1 and SQUID 2.

	I_c (μA)	R_N (mΩ)	I_cR_N (μV)	β_L	L (pH)	M_i^{-1} $\left(\frac{\text{mA}}{\Phi_0}\right)$	V_Φ $\left(\frac{\mu\text{V}}{\Phi_0}\right)$	$S_{\Phi,w}^{1/2}$ $\left(\frac{\text{n}\Phi_0}{\text{Hz}^{1/2}}\right)$
SQUID 1	129	385	50	0.19	3.0	2.63	154	260
SQUID 2	227	250	57	0.25	2.3	2.73	164	200

From the modulation period we obtain the inverse mutual inductance $M_i^{-1} = 2.73\,\text{mA}/\Phi_0$. From the modulation depth we find a screening parameter $\beta_L \equiv 2I_0L/\Phi_0 = 0.25$. By assuming that both JJs are identical, i.e., $I_c \equiv 2I_0$, we determine the SQUID inductance $L = 2.3\,$pH.

The $V(I_{mod})$ modulation for different bias currents, plotted in the inset of Fig. 2(b), yields a maximum transfer function $V_\Phi \equiv \partial V/\partial\Phi = 164\,\mu\text{V}/\Phi_0$ for $I_b = 230\,\mu$A. The shift in $I_c(I_{mod})$ and $V(I_{mod})$ for positive and negative bias currents can be attributed to the asymmetric current bias, which leads to an inductance asymmetry $\alpha_L \equiv (L_2 - L_1)/(L_1 + L_2)$; here L_1 and L_2 are the inductances of the two SQUID arms. The measured $I_c(I_{mod})$-characteristics are fitted well by numerical simulations based on coupled Langevin equations[25] with a noise parameter $\Gamma \equiv 2\pi k_B T/I_0\Phi_0 = 1.55 \cdot 10^{-3}$ (k_B is the Boltzmann constant) and $\alpha_L = -0.35$ (see inset of Fig. 2(a), dotted lines).

Using a commercial SQUID amplifier with a voltage noise $S_V^{1/2} \approx 40\,\text{pV}/\text{Hz}^{1/2}$ and a $-3\,$dB cutoff frequency $f_c \approx 30\,$kHz, we measured the spectral density of the rms flux noise $S_\Phi^{1/2}(f) \equiv S_V^{1/2}(f)/|V_\Phi|$ at the optimum working point (see solid line in Fig. 2(b)). Here the SQUID amplifier contribution was subtracted. We observe a significant low-frequency excess noise, which we assign to I_0 fluctuations in the JJs. Since the low-frequency excess noise extends to well

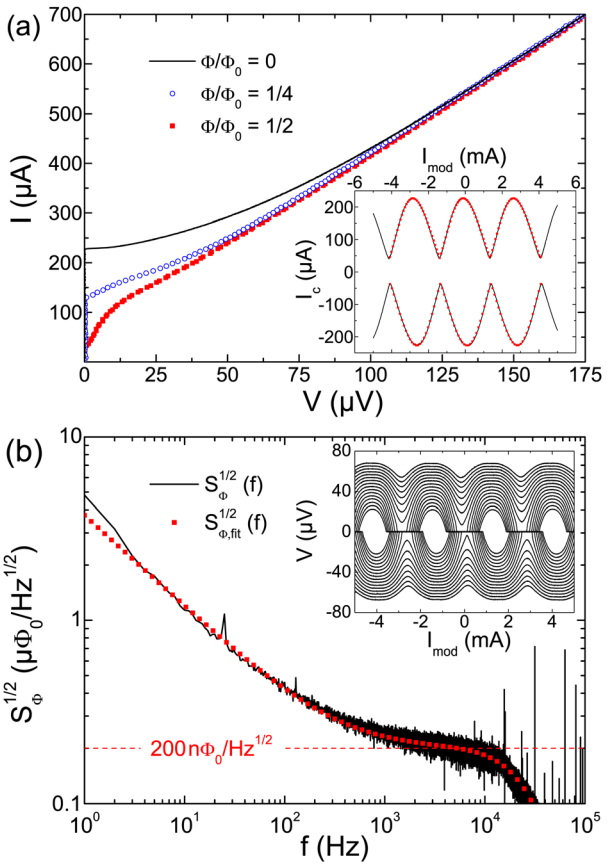

FIG. 2. Transport and noise characteristics of SQUID 2. (a) IVCs for different flux Φ; inset shows measurement (solid black lines) and numerical simulation (dotted red lines) of $I_c(I_{mod})$. (b) Solid black line: Spectral density of rms flux noise $S_\Phi^{1/2}(f)$ at optimum working point ($I_b = 230\,\mu$A, $I_{mod} = 243\,\mu$A). Dotted (red) line: fitted spectrum; dashed (red) line indicates white noise level for fitted curve. Inset shows $V(I_{mod})$ for $I_b = \pm(150\ldots300)\,\mu$A (in $10\,\mu$A steps).

above 1 kHz and due to the limited bandwidth of the SQUID amplifier, we do not see a clear white noise region in the spectrum. By fitting the experimental data (dotted line in Fig. 2(b)), we derive a low-frequency noise contribution $S_{\Phi,f}^{1/2} \propto 1/f^{\alpha}$ with $\alpha = 0.5$ and $S_{\Phi,f}^{1/2}(f = 1\,\mathrm{Hz}) = 3.7\,\mu\Phi_0/\mathrm{Hz}^{1/2}$ and a white noise contribution $S_{\Phi,\mathrm{w}}^{1/2} = 200\,\mathrm{n}\Phi_0/\mathrm{Hz}^{1/2}$ (dashed line in Fig. 2(b)).

In order to determine the spin sensitivity $S_{\mu}^{1/2} \equiv S_{\Phi}^{1/2}/\phi_{\mu}$ of our SQUIDs, we calculated the coupling factor ϕ_{μ}, using a routine based on the numerical solution of the London equations for the given SQUID geometry.[26] Here, $\phi_{\mu} \equiv \Phi/\mu$ is the magnetic flux Φ per magnetic moment $|\vec{\mu}| \equiv \mu$ coupled by a magnetic particle to the SQUID loop. Very recently, the validity of this approach has been verified experimentally by measuring the magnetic coupling of a Ni nanotube to a Nb nanoSQUID which had the same geometry as SQUID 2.[27] For a point-like magnetic particle with $\vec{\mu}$ perpendicular to the substrate plane, placed at a lateral distance of 10 nm from the lower edge of the upper Nb SQUID arm at the center of the loop, we obtain $\phi_{\mu} = 8.6\,\mathrm{n}\Phi_0/\mu_B$ (μ_B is the Bohr magneton). Along with the obtained value of the rms flux noise $S_{\Phi,\mathrm{w}}^{1/2} = 200\,\mathrm{n}\Phi_0/\mathrm{Hz}^{1/2}$ we calculate the spin sensitivity to $S_{\mu}^{1/2} = 23\,\mu_B/\mathrm{Hz}^{1/2}$.

To investigate the SQUID performance in a magnetic field B applied perpendicular to the substrate plane we mounted SQUID 1 on a high-precision alignment system (one rotator, two goniometers). B is generated by a superconducting split coil running in persistent mode to suppress field noise.[28] Figure 3(a) shows $I_c(B)$ for SQUID 1 after the alignment process for a field sweep sequence as indicated by labels 0–6. The observed hysteresis for $|B| < 45\,\mathrm{mT}$ is ascribed to entry and trapping of Abrikosov vortices in the 4 μm wide connection lines, cf., inset of Fig. 3(b). The steep jump in I_c at $B \approx 45\,\mathrm{mT}$ can be assigned to a vortex entering the narrow Nb leads very close to the SQUID loop, as confirmed recently by magnetic force microscopy on a similar Nb nanoSQUID (with layout of SQUID 2).[27] Subsequently, we reduced the linewidth of the connection lines of SQUID 1 from 4 μm to ~500 nm by focused ion beam (FIB) milling[28] (see inset of Fig. 3(b)). For the repatterned device, the maximum I_c was reduced by ~10%, probably due to a slight degradation of the JJs during FIB milling. More importantly, I_c became almost independent of B, and within $B \approx \pm 50\,\mathrm{mT}$ the magnetic hysteresis disappeared, cf., Fig. 3(b). At $B \approx 50\,\mathrm{mT}$ we still observed the jump in I_c due to vortex entry in the narrow Nb line close to the SQUID. This indicates that the linewidth of the Nb wiring close to the SQUID may limit the range of operation to $|B| \leq 50\,\mathrm{mT}$. However, as will be shown below, even after vortex entry, by proper realignment of the applied magnetic field direction, which compensates the stray magnetic flux induced by trapped vortices, I_c can be restored and low flux noise can be retained.

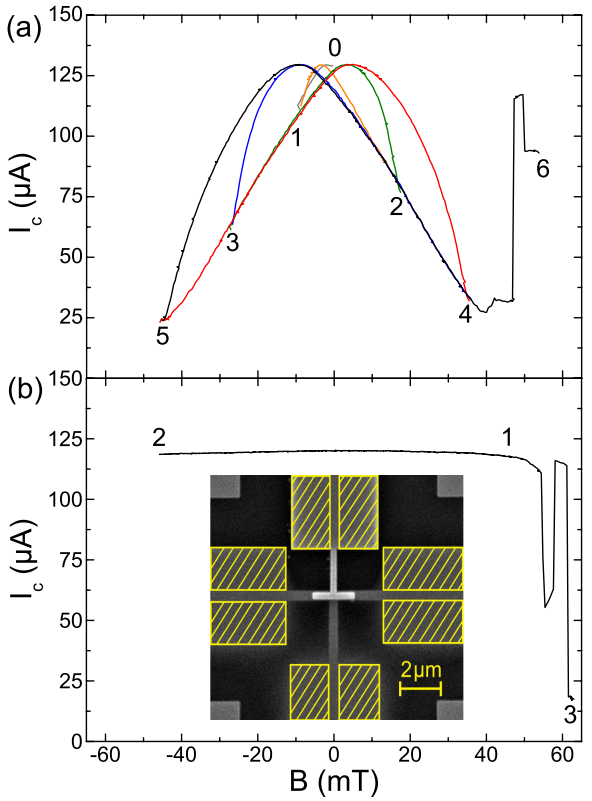

FIG. 3. $I_c(B)$ data of SQUID 1 for field sweep sequence 0–6 (a) and 1–3 (b) after removing Nb areas by FIB milling as indicated by hatched (yellow) rectangles in the inset (SEM image).

We now turn to SQUID 2, which has much longer narrow bias lines. Figure 4(a) shows $I_c(B)$ for a field sweep $46\,\mathrm{mT} \rightarrow -46\,\mathrm{mT} \rightarrow 55\,\mathrm{mT}$ (1–3). Again I_c is almost independent of B for $|B| \leq 50\,\mathrm{mT}$ and, as before, we find a jump in I_c at $B \approx 50\,\mathrm{mT}$ due to a vortex entering the narrow bias lines. The vortex can be removed by sweeping back the field as indicated by the curve (3–4) in Fig. 4(a).

For SQUID 2 we performed noise measurements as described above to determine $S_{\Phi,\mathrm{w}}^{1/2}$ at several values of B from 0 to 50 mT, without any jump in I_c (see inset of Fig. 4(a)). For $B = 0$, $S_{\Phi,\mathrm{w}}^{1/2} \approx 220\,\mathrm{n}\Phi_0/\mathrm{Hz}^{1/2}$, which is slightly higher than the value obtained in the low-field setup. We attribute this to external disturbances from the unshielded environment in the high-field setup (cf., noise spectrum in Fig. 4(b), black line). As indicated in the inset of Fig. 4(a), the white noise level increases only slightly with B to $S_{\Phi,\mathrm{w}}^{1/2} \approx 250\,\mathrm{n}\Phi_0/\mathrm{Hz}^{1/2}$ at $B = 50\,\mathrm{mT}$ (cf., noise spectrum in Fig. 4(b)), still corresponding to a very small spin sensitivity $S_{\mu}^{1/2} \approx 29\,\mu_B/\mathrm{Hz}^{1/2}$ (in the white noise regime). We assign this behavior to a minor decrease of I_c due to an imperfect alignment of the device relative to B. At $B = 55\,\mathrm{mT}$, i.e., after the jump in I_c occurred and after realigning the SQUID by maximizing I_c, we obtain a similar value $S_{\Phi,\mathrm{w}}^{1/2} \approx 240\,\mathrm{n}\Phi_0/\mathrm{Hz}^{1/2}$ as for $B = 50\,\mathrm{mT}$. Following the same procedure of realignment, we were able to operate the SQUID in magnetic fields up to $B = 0.5\,\mathrm{T}$, yielding the noise spectrum as shown in Fig. 4(b), with $S_{\Phi,\mathrm{w}}^{1/2} \approx 680\,\mathrm{n}\Phi_0/\mathrm{Hz}^{1/2}$, corresponding to $S_{\mu}^{1/2} \approx 79\,\mu_B/\mathrm{Hz}^{1/2}$. Note that all spectra feature excess low-frequency noise peaks, which are presumably due to mechanical vibrations of the setup.

In conclusion, we fabricated and investigated Nb nanoSQUIDs based on a trilayer geometry which were optimized for stable operation in comparatively large magnetic fields. Very low white flux noise values down to $S_{\Phi,\mathrm{w}}^{1/2} \approx 200\,\mathrm{n}\Phi_0/\mathrm{Hz}^{1/2}$ have been achieved in a shielded environment yielding a spin sensitivity $S_{\mu}^{1/2} \approx 23\,\mu_B/\mathrm{Hz}^{1/2}$. Concerning the suitability to applied magnetic fields, we

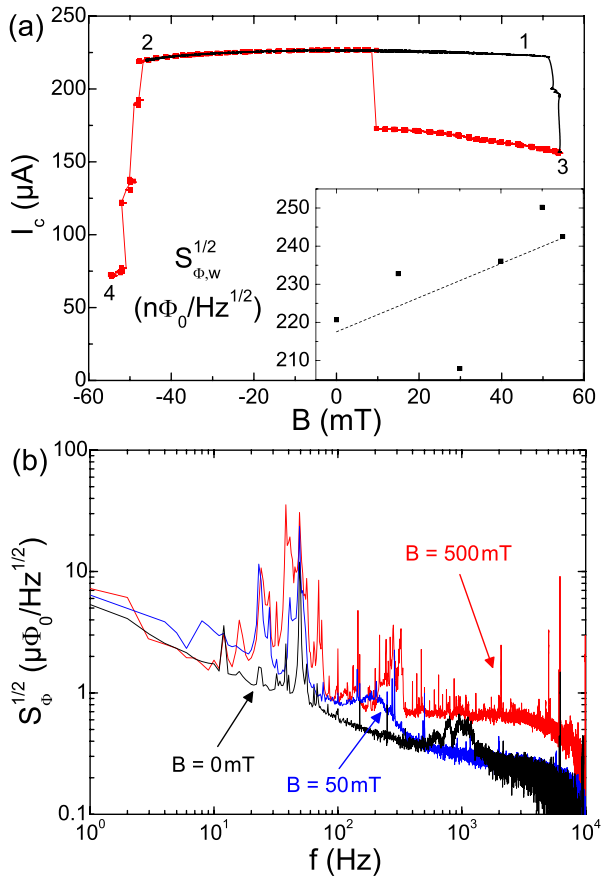

FIG. 4. (a) $I_c(B)$ data of SQUID 2 for field sweep sequence 1–3 (black solid line) and 3–4 (red line plus symbols). Inset: $S^{1/2}_{\Phi,w}(B)$ at optimum working point; dashed line is a linear fit. (b) Spectral density of rms flux noise $S^{1/2}_{\Phi}(f)$ for $B = 0$ mT, 50 mT, and 500 mT.

redesigned the layout of SQUID 1 via FIB milling and implemented these findings into the design of SQUID 2. We demonstrated stable operation in a field range of $B \approx \pm 50$ mT with a marginal increase in white flux noise and spin sensitivity with B ($S^{1/2}_{\Phi,w} \leq 250\,n\Phi_0/Hz^{1/2}$ and $S^{1/2}_{\mu} \leq 29\,\mu_B/Hz^{1/2}$). Moreover it was shown that SQUID 2 can maintain high sensitivity in large fields up to $B = 0.5$ T with $S^{1/2}_{\Phi,w} \approx 680\,n\Phi_0/Hz^{1/2}$ and $S^{1/2}_{\mu} \approx 79\,\mu_B/Hz^{1/2}$. An obvious way to further decrease $S^{1/2}_{\Phi}$ and $S^{1/2}_{\mu}$ is to lower the SQUID inductance L, which can be done easily by decreasing the lateral distance between the JJs and by reducing the thickness of the SiO_2 layer separating the top and bottom Nb layers. In addition, the width of the Nb lines can be reduced further to increase ϕ_μ and to extend the range of magnetic fields where the SQUID can be operated without vortices entering the wiring. All in all, we consider a spin sensitivity down to a few $\mu_B/Hz^{1/2}$, for a field range exceeding 100 mT, to be achievable for this type of device.

J. Nagel and T. Schwarz gratefully acknowledge support by the Carl-Zeiss-Stiftung. We thank K. Störr for assistance in device fabrication. This work was funded by the DFG via the SFB TRR 21 and by the ERC via SOCATHES.

[1]D. Gatteschi and R. Sessoli, Angew. Chem., Int. Ed. **42**, 268 (2003).
[2]W. Wernsdorfer, Nature Mater. **6**, 174 (2007).
[3]L. Bogani, A. Vindigni, R. Sessoli, and D. Gatteschi, J. Mater. Chem. **18**, 4750 (2008).
[4]W. Wernsdorfer, Adv. Chem. Phys. **118**, 99 (2001).
[5]J. Fortágh and C. Zimmermann, Science **307**, 860 (2005).
[6]P. Bushev, D. Bothner, J. Nagel, M. Kemmler, K. B. Konovalenko, A. Loerincz, K. Ilin, M. Siegel, D. Koelle, R. Kleiner, and F. Schmidt-Kaler, Eur. Phys. J. D **63**, 9 (2011).
[7]J. R. Kirtley, M. B. Ketchen, K. G. Staviasz, J. Z. Sun, W. J. Gallagher, S. H. Blanton, and S. J. Wind, Appl. Phys. Lett. **66**, 1138 (1995).
[8]R. Black, F. Wellstood, E. Dantsker, A. Miklich, D. Nemeth, D. Koelle, F. Ludwig, and J. Clarke, Appl. Phys. Lett. **66**, 99 (1995).
[9]C. Veauvy, K. Hasselbach, and D. Mailly, Rev. Sci. Instrum. **73**, 3825 (2002).
[10]J. R. Kirtley, Supercond. Sci. Technol. **22**, 064008 (2009).
[11]A. Finkler, Y. Segev, Y. Myasoedov, M. L. Rappaport, L. Neman, D. Vasyukov, E. Zeldov, M. E. Huber, J. Martin, and A. Yacoby, Nano Lett. **10**, 1046 (2010).
[12]A. Finkler, D. Vasyukov, Y. Segev, L. Néeman, E. O. Lachman, M. L. Rappaport, Y. Myasoedov, E. Zeldov, and M. E. Huber, Rev. Sci. Instrum. **83**, 073702 (2012).
[13]C. P. Foley and H. Hilgenkamp, Supercond. Sci. Technol. **22**, 064001 (2009).
[14]M. Faucher, P.-O. Jubert, O. Fruchart, W. Wernsdorfer, and V. Bouchiat, Supercond. Sci. Technol. **22**, 064010 (2009).
[15]L. Chen, W. Wernsdorfer, C. Lampropoulos, G. Christou, and I. Chiorescu, Nanotechnology **21**, 405504 (2010).
[16]E. J. Romans, S. Rozhko, L. Young, A. Blois, L. Hao, D. Cox, and J. C. Gallop, IEEE Trans. Appl. Supercond. **21**, 404 (2011).
[17]R. Russo, C. Granata, E. Esposito, D. Peddis, C. Cannas, and A. Vettoliere, Appl. Phys. Lett. **101**, 122601 (2012).
[18]N. Antler, E. M. Levenson-Falk, R. Naik, Y.-D. Sun, A. Narla, R. Vijay, and I. Siddiqi, arXiv:1303.2737.
[19]E. M. Levenson-Falk, R. Vijay, N. Antler, and I. Siddiqi, Supercond. Sci. Technol. **26**, 055015 (2013).
[20]L. Hao, J. C. Macfarlane, J. C. Gallop, D. Cox, J. Beyer, D. Drung, and T. Schurig, Appl. Phys. Lett. **92**, 192507 (2008).
[21]J. Nagel, O. F. Kieler, T. Weimann, R. Wölbing, J. Kohlmann, A. B. Zorin, R. Kleiner, D. Koelle, and M. Kemmler, Appl. Phys. Lett. **99**, 032506 (2011).
[22]D. Hagedorn, R. Dolata, F.-I. Buchholz, and J. Niemeyer, Physica C **372–376**, 7 (2002).
[23]D. Hagedorn, O. Kieler, R. Dolata, R. Behr, F. Müller, J. Kohlmann, and J. Niemeyer, Supercond. Sci. Technol. **19**, 294 (2006).
[24]D. J. Van Harlingen, R. H. Koch, and J. Clarke, Appl. Phys. Lett. **41**, 197 (1982).
[25]B. Chesca, R. Kleiner, and D. Koelle, "Fundamentals and technology of SQUIDs and SQUID systems," in *The SQUD Handbook*, edited by J. Clarke and A. I. Braginski (Wiley-VCH, Weinheim, 2004), Vol. 1, Chap. 2, pp. 29–92.
[26]J. Nagel, K. B. Konovalenko, M. Kemmler, M. Turad, R. Werner, E. Kleisz, S. Menzel, R. Klingeler, B. Büchner, R. Kleiner, and D. Koelle, Supercond. Sci. Technol. **24**, 015015 (2011).
[27]J. Nagel, A. Buchter, F. Xue, O. F. Kieler, T. Weimann, J. Kohlmann, A. B. Zorin, D. Rüffer, E. Russo-Averchi, R. Huber, P. Berberich, A. Fontcuberta i Morral, D. Grundler, R. Kleiner, D. Koelle, M. Poggio, and M. Kemmler, arXiv:1305.1195.
[28]T. Schwarz, J. Nagel, R. Wölbing, M. Kemmler, R. Kleiner, and D. Koelle, ACS Nano **7**, 844 (2013).